ATTENUATION IN THE MANTLE, FROM SPECTRAL ANALYSIS OF SHORT-PERIOD SEISMIC WAVES

A thesis submitted for the degree of

DOCTOR OF PHILOSOPHY

in the

Australian National University

by

JOHN ROBERT CLEMENTS

February 1980

STATEMENT

The studies described in this thesis were carried out while I was a full-time research scholar in the Research School of Earth Sciences at the Australian National University during the period September 1975 to February 1980. Except where mentioned in the text or in the acknowledgements, the research described in this thesis is my own. This thesis has never been submitted to another university or similar institution.

John Robert Clements

February, 1980.

ACKNOWLEDGEMENTS

I am indebted to my original supervisor Professor Anton L. Hales (now at the University of Texas at Dallas) who granted me a scholarship at A.N.U. and presented me with this challenging topic. His insight into geophysical problems has never ceased to amaze me.

My appreciation goes to Drs. John Cleary and Ken Muirhead for acting as supervisors after the retirement of Professor Hales. Discussions with John and Ken have lead to many of the final conclusions given in this research. Their critical reading of this manuscript, even though frustrating at times, has lead to many improvements.

Special thanks are owed to Professor Kurt Lambeck for his advice and encouragement. His faith in the ultimate success of the project has been a continual comfort.

For assistance in the spectral analysis aspect of the work, I would like to thank Dr. E.J. Hannan (Research School of Statistical Mathematics, A.N.U.) and Mr Doug Christie. Both have contributed much to the development of my thinking in this field.

Thanks also to the seismological observatory staff, Mrs Jan Weekes, Mrs Willey Penders and Mrs Clementine Krayshek for their continual support in the preparation of this thesis. They not only drafted many of the figures, but also gave me personal encouragement to keep going during my gloomiest moments.

I have been grateful for the continual friendship of Mr Jonathan Ridler, who helped me solve many of the operational computer problems which arose from time to time; to Ms. Jane Prowse, who typed the rough draft; and to Miss Carmel B. Neagle and Mrs Jennifer Barreda for careful typing of the manuscript into its final form.

Others to whom I am indebted are too numerous to mention by name, but include many of the faculty, staff and fellow students whom I consider good friends. Their understanding and concern for me will never be forgotten.

Last but not least, I would like to thank my wife, Beverley, for her good humor and patience which lasted much longer than mine. Without her help this research would not have been possible.

TABLE OF CONTENTS

ABSTRACT

Various techniques for estimating t* (travel time/quality factor Q) from short period array records of body waves have been investigated. Spectral analysis in the frequency domain seems to be more appropriate for this purpose than time domain methods, because of the relative ease in which source and instrument effects can be removed. Of the techniques available, those based on maximum likelihood and homomorphic deconvolution give estimates of relative power versus frequency which best represent the power contained in a time domain wavelet of short duration. The latter technique seemed to have better noise-eliminating properties than the former, without the need to resort to pre-whitening.

Homomorphic deconvolution was therefore used to obtain estimates of t* values from P, PcP, ScP and S phases recorded at the Warramunga array in the Northern Territory of Australia. The source regions for the events studied were the Sunda, Mariana, New Hebrides, Kermadec and Tonga trench zones.

The short-period t* estimates obtained by this means were much smaller than estimates from published Free-oscillation Q models, indicating that the values of Q for compressional and shear waves are frequency dependent. It was found that the short-period and free oscillation data could be satisfied by assuming a linear relationship between Q and frequency, and that this relationship was consistent with other published data. The variation of Q_α/Q_β, Q_K and phase velocity with frequency were also examined. The results of this investigation suggest new directions from which the Q structure of the mantle can be studied.

CHAPTER 1

INTRODUCTION

1.1 Review of Problems Related to Q in the Mantle

If the earth were perfectly elastic, seismic waves, whatever their origin, would continue to vibrate indefinitely. Because the earth is not perfectly elastic, vibrational energy is progressively dissipated. As the material through which the vibrations pass is strained, energy is lost - in the form of heat - through what is often collectively referred to as solid friction. The loss of elastic energy in this manner is generally known as anelasticity. The quality factor Q is a useful measure of anelastic damping. For most purposes, Q may be conveniently defined in terms of the dissipation factor Q^{-1}; that is, $2\pi Q^{-1}$ is equal to the fraction of the total strain energy dissipated per cycle. In general a better understanding of anelasticity in terms of Q mechanisms, i.e. the manner in which vibrational energy is attenuated in the earth, would be of great value to earth scientists.

So far, many researchers interested in how tectonic features occur on the earth have had to rely on creep mechanisms for their explanations. A better understanding of the temperature, pressure, grain structure, etc., in the crust and mantle would enable these workers to put forward more sophisticated explanations. More information about such physical conditions may possibly be deduced from Q mechanisms found by seismological means.

Turning to a more specific problem in seismology, it is not known how anelasticity and phase velocity dispersion are related to frequency for mantle material. It is assumed that parameters such as temperature, pressure, grain structure, chemical composition, and relaxation time, play an important

role in Q mechanisms. Experimental work by Lomnitz (1956, 1957b) and theoretical work by Futterman (1962), Strick (1967), and others indicate that velocity dispersion due to attenuation is a first order effect. Lomnitz's theory is based on an experimentally-obtained logarithmic creep function and on Boltzmann's after-effect equation; this enabled him to specify Q as a function of frequency. The weakness of this theory is that primary creep would continue indefinitely, which is physically impossible. On the other hand, Futterman's theory is based on dispersion relations of the Kramers-Krönig type used in electric circuit theory. Using these relations, Futterman was able to derive equations for velocity dispersion and Q respectively. These results were criticized by Strick (1967) because Futterman's theory is based on a linear frequency dependence for attenuation which extends to infinite frequency. Another criticism of this theory is that it is empirical and not based on any physical mechanisms of attenuation (Liu, Anderson and Kanamori, 1976).

Another approach to the problem of identifying possible causes for anelasticity in the mantle is to examine attenuation mechanisms discovered in various fields of the physical sciences. A complete review of such mechanisms has been given by Gordon and Nelson (1966) and Jackson and Anderson (1970). If a separate attenuation mechanism can be determined for each part of the mantle, then much information may be gained about melt zones, chemical phase transitions which may exist in layers in the earth, lateral inhomogeneities, grain structure, etc.

In the past it has been assumed that phase velocity dispersion was a second order effect of attenuation. Dispersion was ignored despite objections by Jeffreys (1965), and the work of Lomnitz and Futterman. Using this assumption, attempts have been made to construct average velocity models

for the earth by inversion of free-oscillation eigenperiods (Dziewonski and Gilbert, 1972; Jordan and Anderson, 1974; Gilbert and Dziewonski, 1975; Anderson and Hart, 1976). However, it has been found that these models predicted larger travel time shifts than is actually observed in body wave travel times. Jordan (1975) attempted to attribute this observed discrepancy to continental-oceanic mantle differences extending to great depths; however, such an adjustment for mantle differences has been criticized by Hales (1976) who contended that regional differences in the ScS and multiple ScS residuals can be accommodated in the upper 250 km of the mantle.

More recently, it has been considered that phase velocity dispersion may be a first order effect of attenuation, and that the association between dispersion and attenuation may be related to a Q mechanism of some type (Randall, 1976). Liu, Anderson and Kanamori (1976) have demonstrated that if Q is constant over the seismic frequency range then phase velocity dispersion is of the Futterman type. It was found that better velocity models for the earth could be achieved by correcting free oscillation eigenperiods using Futterman's dispersion equation with the Q for the associated modes (Hart, Anderson and Kanamori, 1977). Hence the existence of deep continental-oceanic mantle differences need not be invoked to explain baseline shifts in body wave data.

The above discussion suggests that many areas of the earth sciences would benefit from determining:

(1) a better measurement of Q with increasing depth;

(2) how phase velocity dispersion varies with Q and frequency;

(3) whether Q depends on frequency; and

(4) the relationship between Q and phase transition zones or layering in the mantle.

A knowledge of these parameters, inter alia, would lead to the deduction of more refined Q and velocity models from free oscillation eigenperiods, a better understanding of plate tectonics in relationship to the upper mantle, and a better understanding of physical and chemical properties of the earth.

1.2 Previous Q Estimates from Body Wave Data

Press (1956) undertook pioneering work to determine Q_β, the average quality factor of S waves, in the whole mantle. He estimated its value to be 500 by comparing the amplitude ratios of S waves multiply-reflected between the earth's surface and the outer core. A similar type of analysis was used by Kovach and Anderson (1964) who found Q_β to be approximately 600 for the frequency range 0.015 to 0.07 Hz. By assuming the radiation from the source to be equal to the upward and downward directions, they were able to establish a Q_β of 200 for the upper 600 km of the mantle, and about 2200 for the rest of the mantle; for the base of the mantle Q_β is at least 5000. Satô and Espinosa (1967) obtained Q_β values which decreased with increasing period, from 720 at 34 sec to 232 at 90 sec. Using spectral ratios of ScS, ScP and PcS phases, Kanamori (1967b) found the average Q_β to be 324 for the mantle in the period range 1.5 to 5 sec.; furthermore, he ascertained the average P wave quality factor Q_α to be 435 for the same period range.

It is suspected that the ratio Q_α/Q_β is strongly dependent on physical mechanisms of attenuation; however, there is no widely accepted theory as to what the ratio should be. Even so, it appears most probable that the value of this ratio lies between 1 and 3. So far very few values have been reported. Kanamori (1967a) determined Q_α/Q_β as being approximately equal to

1 for a period of 1 second. Using spectral ratios of ScS, ScP and PcS phases, Kanamori (1967b), on the basis of only three seismic events, also estimated Q_α/Q_β, for the period range 1.5 to 5 sec., as 1.9. More recently, Takano (1971) reported estimates for two different period ranges. For 0.1 to 1 sec. the ratio was 2.5; for 1 to 10 sec. it was 1.7. Takano's results, like those of Satô and Espinosa, indicate that Q decreases with increasing period.

However, layering in the mantle may have a similar effect on the relationship between amplitude ratio and frequency. The shape of the curve which resulted when he plotted P-wave amplitude ratio against epicentral distances led Teng (1967) to suggest that there may be a low-Q zone at the core-mantle boundary. Kanamori (1967a), examining P and PcP phase data for the period range 0.5 to 2 sec., also concluded that there may be a low-Q zone at the core-mantle boundary; furthermore, he estimated that it was a transition zone of thickness less than 1 km. Other researchers lending weight to the low-Q zone hypothesis are Buchbinder and Poupinet (1973) and Ibrahim (1971a,b).

1.3 Research Goals

The previous discussion indicates that more research is needed to obtain values of Q with better precision. Earlier attempts to obtain Q values for short period compressional and shear waves have so far produced limited results. With the advent of computers and the development of appropriate computer techniques, however, many of the data processing problems of the past have been overcome. New high resolution spectral techniques for limited amounts of data have been developed in recent times (Burg, 1967; Lacoss, 1971; Ulrych and Bishop, 1975). To the author's

knowledge these spectral methods have not been applied previously in an attempt to obtain better power estimates for short period seismic time series.

Accordingly the aims of this project are to determine:

(1) if there are better methods than the more conventional Fourier methods of obtaining the earthquake impulse response function;

(2) the Q structure for both shear and compressional waves in the mantle using P, S, ScP and PcP phases;

(3) whether Q is frequency dependent.

1.4 Outline of This Thesis

The acquisition of the data will be discussed in Chapter 2. This discussion will include the equipment limitations and the signal enhancement procedures used to improve the signal-to-noise ratios of the seismic phases. In Chapter 3 the nature of attenuation will be considered. Other factors (source radiation, instrument response, etc.) which modify the characteristics of seismic wavelets will be discussed in Chapter 4, in order to demonstrate how they may be removed from the data. In addition to the specific impulse responses, the data is always contaminated by noise arising from wave scattering (signal generated noise, Key, 1967) and microseisms. These phenomena usually cannot be treated analytically. Accordingly, in Chapters 5 and 6 current techniques of signal enhancement will be investigated to determine the best available method or methods for estimating the attenuating properties of the earth. The results obtained in this manner, including determination of the distribution and frequency dependence of Q in the mantle, will be presented in Chapter 7. In conclusion a summary of the research done in this thesis is presented in Chapter 8, along with a discussion of possible areas for further investigation.

CHAPTER 2

DATA ACQUISITION AND PROCESSING

2.1 Data Acquisition

2.1.1 The Array

Data collected at the Warramunga Seismic Array (WRA), situated near Tennant Creek in the Northern Territory of Australia, has been used in this study. This array is one of the UKAEA arrays (Keen et al., 1965), and is a modified L-shaped configuration with ten seismometers on each leg, as shown in Figure 2.1. The separation between seismometer pits was fixed at 2 to 2.5 km which has proved to be a near optimum separation to ensure that the background noise is not correlated between instruments. These seismometer pit co-ordinates are given in Table 2.1.

The seismometers are short-period vertical component Willmore MkII instruments, with a natural period of one second and a damping factor of 0.64. The signals from the seismometers are telemetered, using a FM carrier, to a receiving station where all twenty are recorded simultaneously on 24 channel magnetic tape. In addition to the 20 seismic channels, two tracks are recorded with a constant frequency for wow and flutter correction and another track is used for a digital time code.

WRA commenced operation in 1965 as part of the United Kingdom Atomic Energy Authority (UKAEA) nuclear surveillance network. The site was chosen because of its remoteness from cultural noise, and the seismometer pits were located on granite to minimise locally-generated noise.

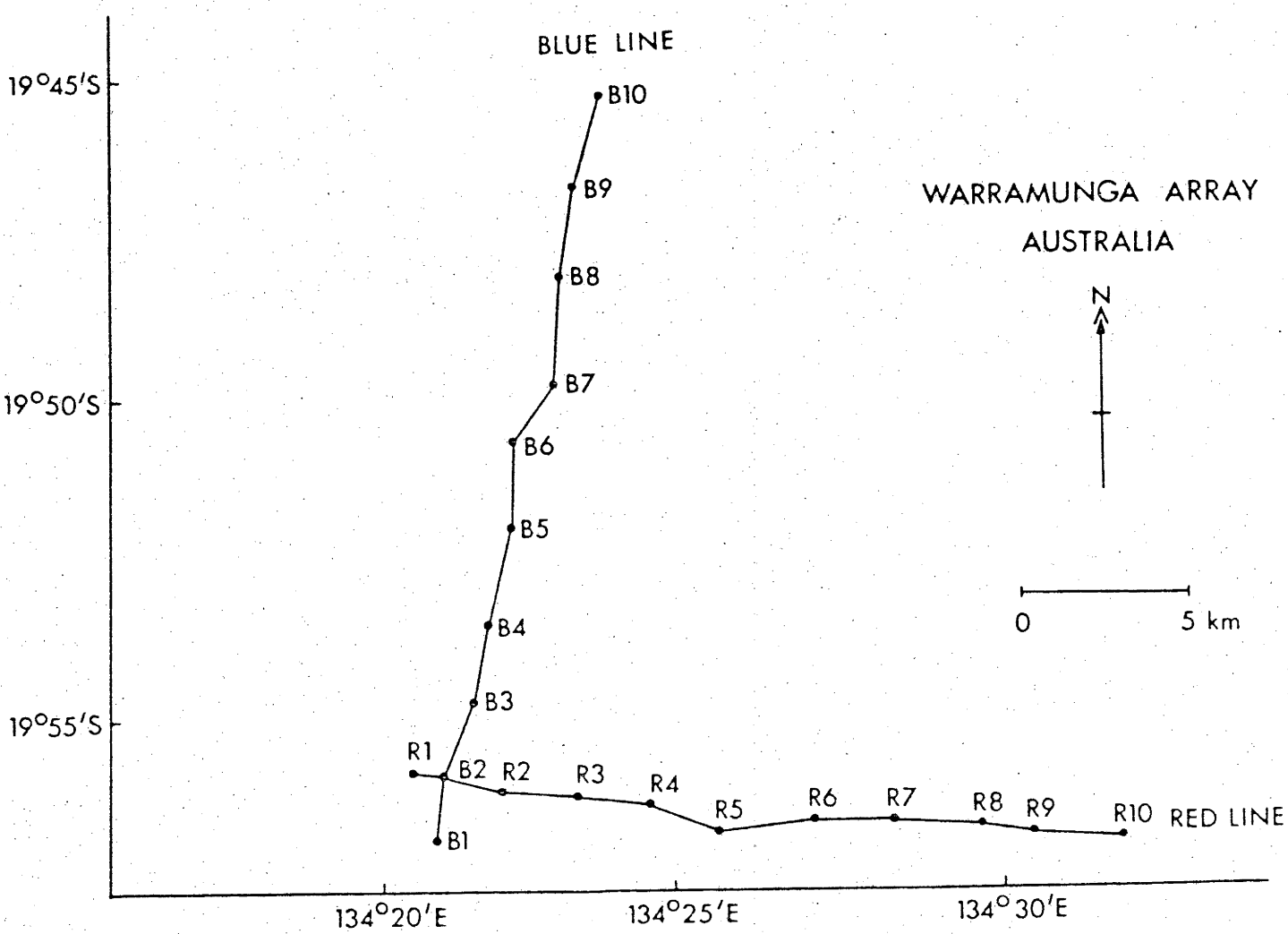

Figure 2.1 Seismometer pit locations for the Warramunga seismic array (WRA).

TABLE 2.1 COORDINATES OF THE INDIVIDUAL SEISMOMETERS OF THE WARRAMUNGA SEISMIC ARRAY

Seismometer	Latitude E	Longitude S	Cartesian Coordinates X, km	Y, km	Elevation feet
B1	134.34776	19.96097	-0.310	-1.476	1294.85
B2	134.35250	19.94417	0.183	0.373	1284.27
B3	134.35681	19.92453	0.638	2.558	1265.89
B4	134.36050	19.90497	1.025	4.724	1252.65
B5	134.36954	19.87971	1.762	7.519	1218.72
B6	134.36852	19.85645	1.863	10.095	1200.07
B7	134.38080	19.84227	3.150	11.662	1268.09
B8	134.38213	19.81541	3.291	14.635	1176.96
B9	134.38530	19.79286	3.623	17.132	1184.94
B10	134.39418	19.76862	4.554	19.816	1188.50
R1	134.34085	19.94411	-1.033	0.391	1281.07
R2	134.36555	19.94890	1.552	-0.140	1265.19
R3	134.38831	19.95000	3.934	-0.264	1236.49
R4	134.40802	19.95181	5.998	-0.465	1228.55
R5	134.42764	19.95949	8.052	-1.314	1217.83
R6	134.45578	19.95525	10.998	-0.846	1155.42
R7	134.47742	19.95667	13.263	-1.004	1167.15
R8	134.50191	19.95726	15.826	-1.074	1212.53
R9	134.51631	19.95912	17.334	-1.281	1190.68
R10	134.54195	19.96109	20.016	-1.502	1161.54

The geographic coordinates of the origin of the cartesian coordinate system are 19.94777°S, 134.35081°E.

Since the commencement of operations at WRA a large data set has been collected on magnetic tape. Previous studies carried out at the Australian National University (ANU) using these data have included the development of array processing techniques (Muirhead, 1968; King, 1974) and velocity modelling of P phases in the mantle (Wright, 1970; Simpson, 1973; and Ram Datt, 1977). The determination of an associated Q model provides a natural complement to these studies.

2.1.2 Playback System

The analog magnetic tapes received from the array are played back using equipment installed at the Australian National University (A.N.U.). A complete description of this playback equipment is contained in the thesis by Muirhead (1968).

The analog signals are first amplified and then demodulated to remove the 270 Hz FM carrier. The resulting amplitude signals are then re-amplified and passed through a bank of high and low pass analog filters to remove background noise associated with the recording station and the playback system. These filters were set for a frequency band range of 0.1 through 3.5 Hz for this study.

The transfer of a specific event from analog tapes to digital form is accomplished in the following manner. First, the magnetic tape is replayed and reviewed on a 16-channel Oscillomink chart recorder. When the required event is detected the tape is backed up and the event digitized using a 12-bit analog-to-digital converter (ADC). The resulting digital information is temporarily stored on computer disc in a multiplexed form, and then transferred from disc to digital magnetic tape. A block diagram of the above equipment arrangements and its interaction with the Datacraft 6024/4

computer is shown in Figure 2.2.

A theoretical dynamic range of 72 dB could be achieved if the playback and recording systems were set up for maximum efficiency. Because of the dynamic range of analog magnetic tapes and microseismic and systems noise, however, the usable dynamic range is reduced to between 40 and 60 dBs. This dynamic range reduction will become more apparent when spectral observations are considered in Chapters 5 and 6.

2.1.3 The Data Set

Using the playback system just described, thirty-two seismic events were digitized from the analog magnetic tapes prepared at WRA. Each phase (P, PcP, ScP, S) was digitized in 200 second segments at a rate of approximately 27 samples per second. Most of these events have a large-amplitude ScP phase associated with them, because it was originally intended that this would be the main phase to be studied. Event location, source depths, earthquake magnitudes and origin times were taken from the U.S.G.S., Norsar, and B.I.S.C. bulletins; this information is tabulated in Table 2.2.

In Figure 2.3 a portion of an equal distance map projection of the earth's surface with WRA co-ordinates at the centre demonstrate pictorially the distribution of the earthquake epicenters along with their vertically projected raypaths. The arrows in this figure indicate the directions in which the down-going slabs are being subducted. In the Pacific, the Tonga-Kermadec and Mariana subducted slabs dip towards WRA, whereas the New Hebrides slab is also being subducted away from WRA. All these down-going slabs, with the notable exception of the New Hebrides slab, are dipping with an approximate angle of 45 degrees. The New Hebrides slab dips at an angle of approximately 75 degrees in the south and 80 degrees in the north. There appears to be a

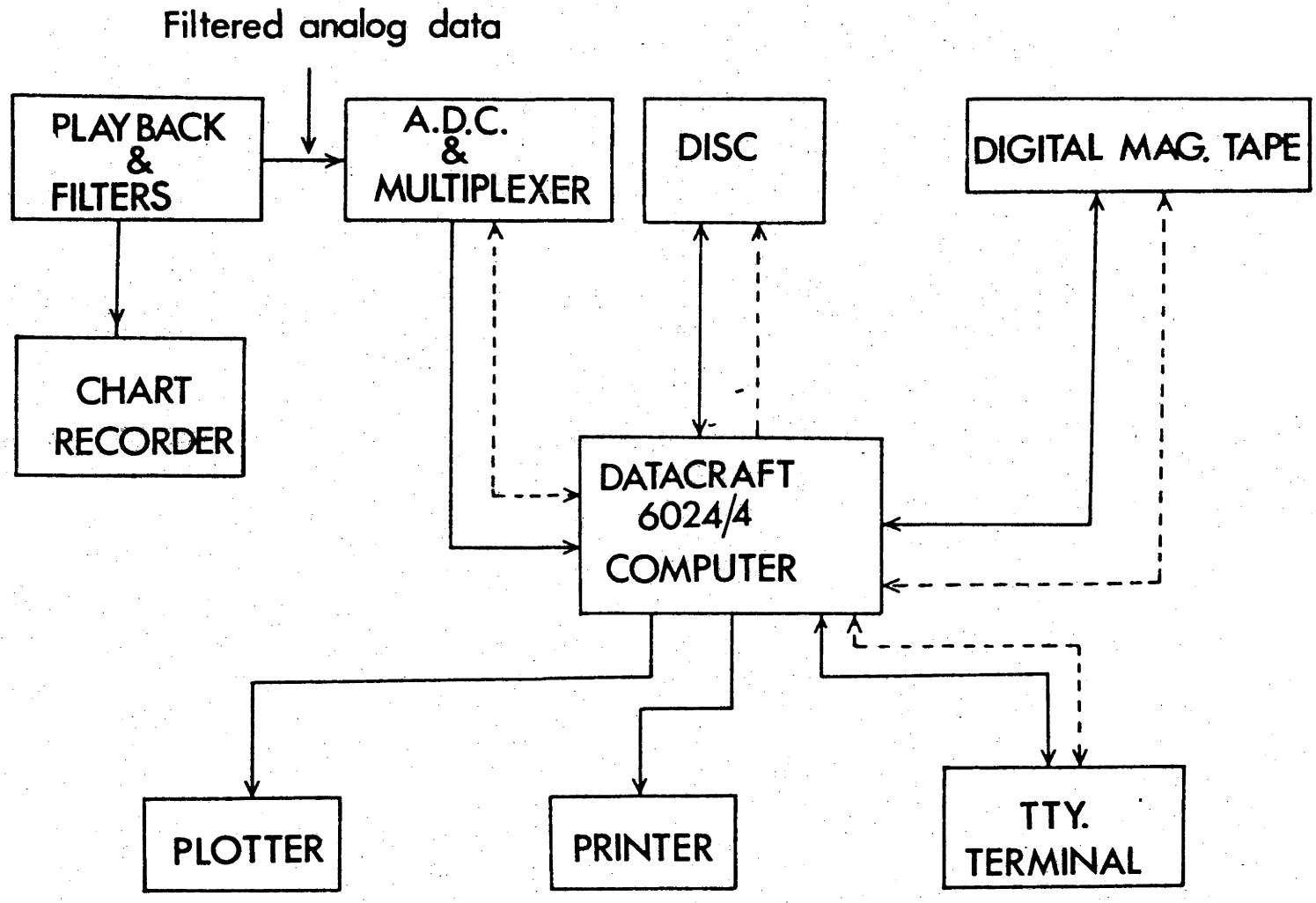

Figure 2.2 Block Diagram of Playback and Computer Systems.

TABLE 2.2

List of Earthquakes studied

Event No.	Date d/m/y	Origin Time (UT) h-m-s	Latitude (deg)	Longitude (deg)	Focal depth (km)	Magnitude (M_b)	Region
1	06/10/75	09-52-16.8	25.35F°S	179.89F°W	491.0	5.3	South of Fiji Islands
2	10/10/75	05-50-17.6	27.16Z°S	179.59 °W	583.0	5.8	South of Fiji Islands
3	17/10/75	01-59-31.4	23.27 °S	179.11 °W	556.0	5.1	South of Fiji Islands
4	31/10/75	16-02-51.5	23.53 °S	180.00 °E	526.0	5.2	South of Fiji Islands
6	12/11/75	21-02-15.3	4.02 °N	123.05 °E	199.0	5.4	Northern Celebes
7	19/11/75	06-18-33.7	24.01 °S	179.09 °E	551.0	5.8	South of Fiji Islands
8	02/12/75	23-22-28.1	3.11 °N	123.54 °E	174.0	5.4	Talaud Island
9	28/03/76	01-42-27.5	13.78 °N	144.73 °E	118.0	5.5	Mariana Islands
10	18/03/76	19-45-22.7	24.64 °S	179.98 °E	489.0	5.0	South of Fiji Islands
11	20/03/76	13-47-33.8	21.49 °S	179.31 °E	619.0	5.2	South of Fiji Islands
12	03/02/76	12-27-31.4	25.12 °S	179.72 °E	486.0	5.8	South of Fiji Islands
13	10/04/76	17-12-08.3	17.66 °S	178.46 °W	548.0	5.7	South of Fiji Islands
15	07/04/76	16-22-45A	13.44 °S	167.09 °E	193.0	5.0	New Hebrides Islands
16	23/04/76	18-33-07.2	22.20 °S	179.58 °W	563.0	4.9	South of Fiji Islands
17	27/05/76	16-52-38.9	19.18 °S	169.56 °E	273.0	5.2	New Hebrides Islands
18	20/05/76	22-51-44.8	31.09 °S	179.89 °W	380.0	5.2	Kermadec Islands
19	09/06/76	16-30-40.1	6.47 °S	151.43 °E	21.0	5.5	New Britian Islands
20	29/06/76	05-01-17.2	21.49 °N	143.01 °E	291.0	5.4	Mariana Islands
21	17/12/75	07-42-07.0	7.01 °S	155.75 °E	67.0	5.8	Solomon Islands
22	20/12/75	11-51-31.4	15.81 °S	167.92 °E	190.0	5.3	New Hebrides Islands
23	16/12/75	15-41-01.2	29.70 °N	137.87 °E	505.0	5.0	South of Honshu, Japan
24	14/01/76	15-30-04.3	32.45 °N	137.41 °E	405.0	5.2	South of Honshu, Japan
25	05/01/76	07-34-31.1	5.41 °S	154.48 °E	254.0	5.1	Solomon Islands
26	18/12/75	00-23-11.5	5.09 °S	151.27 °E	128.0	5.5	New Britain Islands
27	31/08/76	09-06-51.0	30.27 °S	177.97 °W	52.0	5.3	Kermadec Islands
28	05/08/76	13-37-14.7	7.00 °N	94.31 °E	87.0	5.8	Nicobar Islands
29	08/08/76	15-12-29.0	27.22 °N	143.25 °E	184.0	4.8	Volcano Islands
30	15/09/76	12-43-41.4	31.03 °S	179.67 °E	456.0	4.5	South of Kermadec Islands
31	19/10/75	14-49-55.1	21.53 °N	143.00 °E	309.0	5.4	Mariana Islands
32	26/09/76	21-06-00.0	3.53 °S	152.45 °E	457.0	5.1	New Ireland Islands
33	22/12/76	01-01-41.0	23.30 °N	143.72 °E	49.0	5.8	Bonian Island
34	02/10/75	18-40-49.2	18.00 °S	178.52 °W	599.0	5.1	Fiji Islands

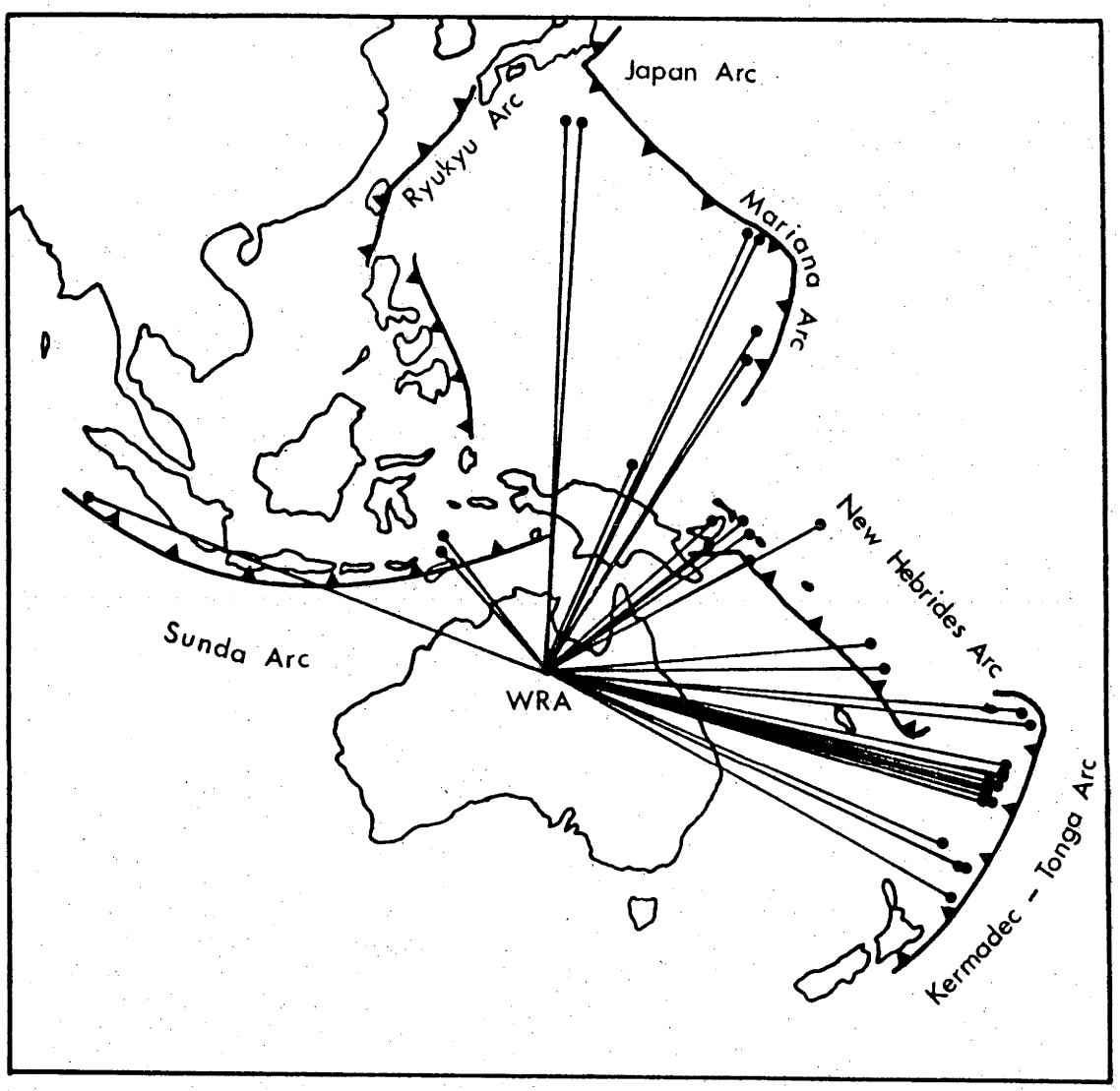

Figure 2.3 Equal distance projection map of the earth's surface with WRA co-ordinates at the centre. The map indicates the vertical projections of ray paths relative to the arc systems.

relationship between the age of the ocean floor being subducted and the dip angle of the down-going plate. The older the ocean floor the less the dip angle (Molnar and Atwater, 1978). Assuming that the Benioff zone is on the upper side of the slab, P and S phases from earthquake sources in the New Hebrides and Sunda arc zones must pass through the slab before reaching WRA. In all cases the ScP and PcP phases pass through the slab. Perturbations on Q values caused by the age and thickness of the material in the down-going slab through which the seismic wave travels are unknown. This will be explored more fully in Chapter 7.

2.2 Preliminary Data Processing

Azimuths and epicentral distances to WRA were calculated from the epicenter co-ordinates given in Table 2.2. In addition, the slownesses ($dt/d\Delta$) of each seismic phase were calculated from the Jeffreys-Bullen (J-B) tables. These calculated values are presented in Table 2.3. The azimuth and slowness were then used for stacking (sum and delay) the array data for each phase to a common point. Because limited information exists about possible station anomalies (Wright, 1970) each of the channels were equally weighted. The stacked channels would then represent the best average response of the earthquake under study (Mack, 1969).

Some precision can be expected to be lost by not implementing an adaptive array processing technique (beamforming) to determine the azimuths and slownesses for these seismic phases. However, at a sampling rate of 25 samples/second the best precision achieved from WRA data is 2 degrees of the actual azimuth and 0.2 sec/deg of the actual slowness (Ram Datt, 1977). The calculated values in Table 2.3 are therefore within the precision given by adaptive processing. Misalignment of the stacked data will mainly affect

TABLE 2.3
Calculated Earthquake Parameters

Event No.	Δ to WRA (deg)	P - Phase Travel Time (sec)	P - Phase dT/dΔ (sec/deg)	PcP - Phase Travel Time (sec)	PcP - Phase dT/dΔ (sec/deg)	ScP - Phase Travel Time (sec)	ScP - Phase dT/dΔ (sec/deg)	S - Phase Travel Time (sec)	S - Phase dT/dΔ (sec/deg)	Azimuth (deg)
1	42.29	430.4	7.9			718.6	4.0	773.3	14.4	106.00
2	41.16	428.8	8.0			706.4	4.0	774.6	14.2	101.25
3	41.65	420.4	8.0			705.4	4.0	755.0	14.4	102.92
4	42.42	428.5	8.0			711.9	4.0	734.9	14.6	103.31
6	25.55	285.0	9.3			315.7	2.9	518.2	17.4	338.80
7	41.54	420.2	8.0			705.2	4.0	754.3	14.4	104.00
8	24.54	305.1	9.4			725.2	2.8	549.9	17.9	338.38
9	35.07	402.7	7.9	513.5	2.9	767.6	2.9	725.0	15.3	17.68
10	42.38	430.5	7.9			718.1	4.0	773.0	14.4	104.74
11	43.24	429.5	7.9			701.2	4.0	770.5	14.2	100.54
12	42.04	429.4	7.9			718.6	4.0	770.7	14.4	105.66
13	44.59	444.5	7.8			717.7	4.1	798.2	14.1	95.16
15	32.01	368.3	7.9			743.2	3.3	671.2	15.4	83.30
16	42.92	430.1	7.9			706.8	4.0	778.6	14.3	101.41
17	33.15	371.8	8.5			675.6	3.5	736.1	15.4	94.64
18	42.41	439.9	8.1			500.0	4.0	790.2	14.5	114.63
19	21.31	287.6	10.1			757.9	2.4	533.7	15.3	53.37
20	42.06	429.7	8.1			755.7	4.0	798.3	14.6	12.06
21	24.45	314.3	9.7	533.0	2.1	747.8	2.8	577.2	17.7	61.08
22	32.20	369.9	8.6	534.7	2.7	562.5	2.7			88.02
23	49.53	484.1	7.5			745.6	4.2	876.0	13.6	3.09
24	49.53	510.6	7.5	577.8	3.6	775.3	4.2	922.9	13.5	3.90
25	24.36	296.2	9.7			705.1	2.8	533.0	14.2	56.40
26	22.17	286.4	9.7			725.2	2.6	521.4	17.6	50.34
27	44.93	483.9	8.0			824.9	3.9	873.9	14.3	112.75
28	49.06	508.3	7.3	597.3	3.6	813.5	4.2	911.3	14.2	302.16
29	42.87	460.0	8.0	569.5	3.3	783.2	4.0			12.00
30	41.72	431.0	8.2			724.3	4.0			117.44
31	42.13	443.8	8.0			753.8	4.0	798.0	14.6	12.06
32	24.08	277.8	9.0			661.8	2.8	499.7	15.7	49.50
33	44.51	438.8	8.0			819.8	4.1	873.0	15.1	13.06
34	44.51	439.1	7.7			708.8	4.1	790.8	14.1	95.64

the higher frequencies. For example, if two channels were stacked and the delay times were off by 0.17 second, a 3 Hz wave would add out. In addition, misalignment of the array will cause oscillations in power spectrums because of constructive and destructive interference. This effect and how to eliminate it will be considered in Chapters 5 and 6.

If the noise component (i.e. white noise, microseisms, and other seismic phases) can be considered random, the optimal amplitude noise reduction of the stacked record would be the square root of the number of channels used in the stack (Robinson, 1970). However, all the noise components cannot be considered as random, therefore the noise reduction will be somewhat less than the optimal value. Figure 2.4 through 2.10 are examples of the records used for stacking and the final results of the stacking procedure.

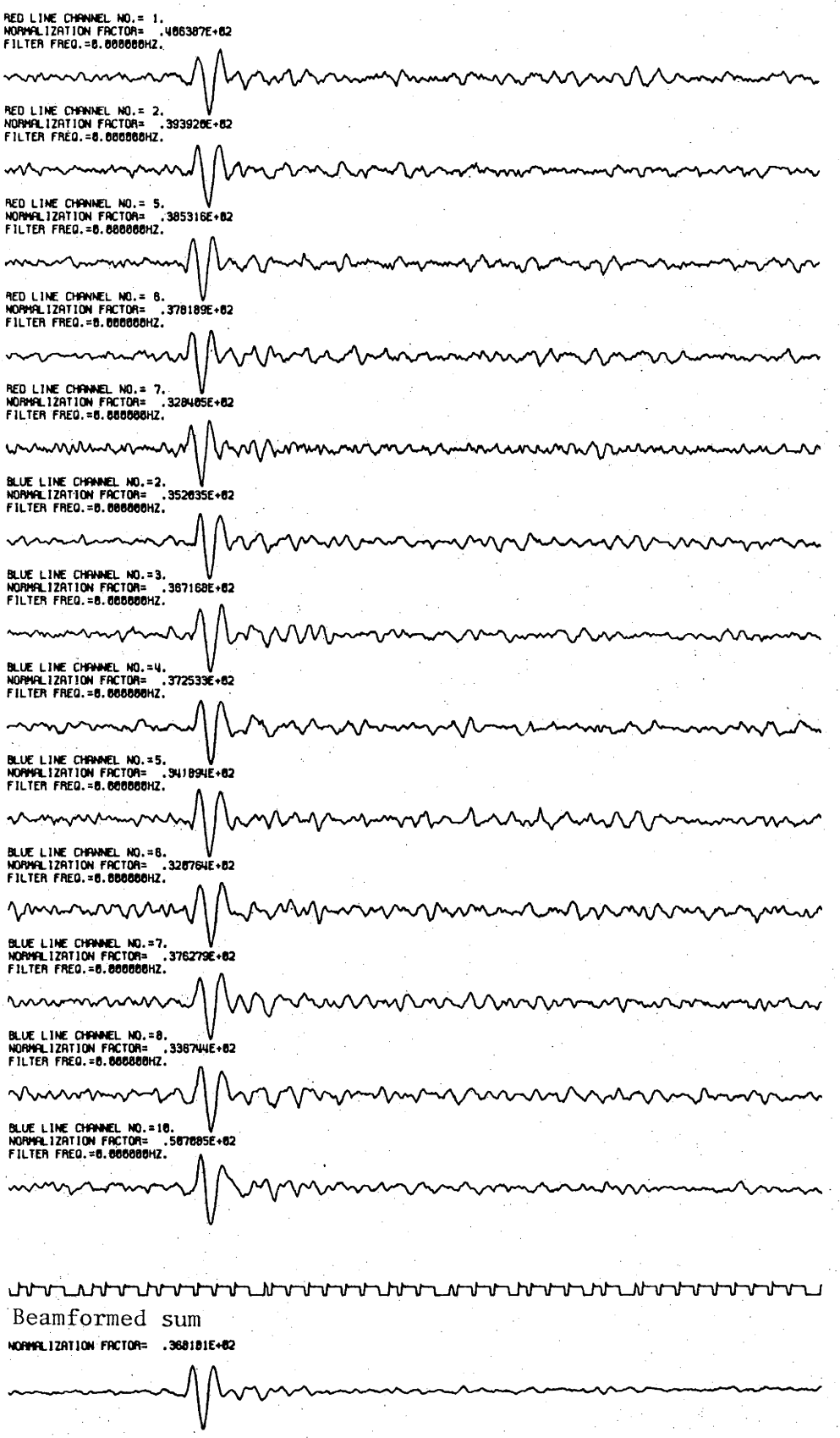

Figure 2.4 Seismogram of individual array channels, time record, and beamformed trace, for ScP phase of Event No. 3.

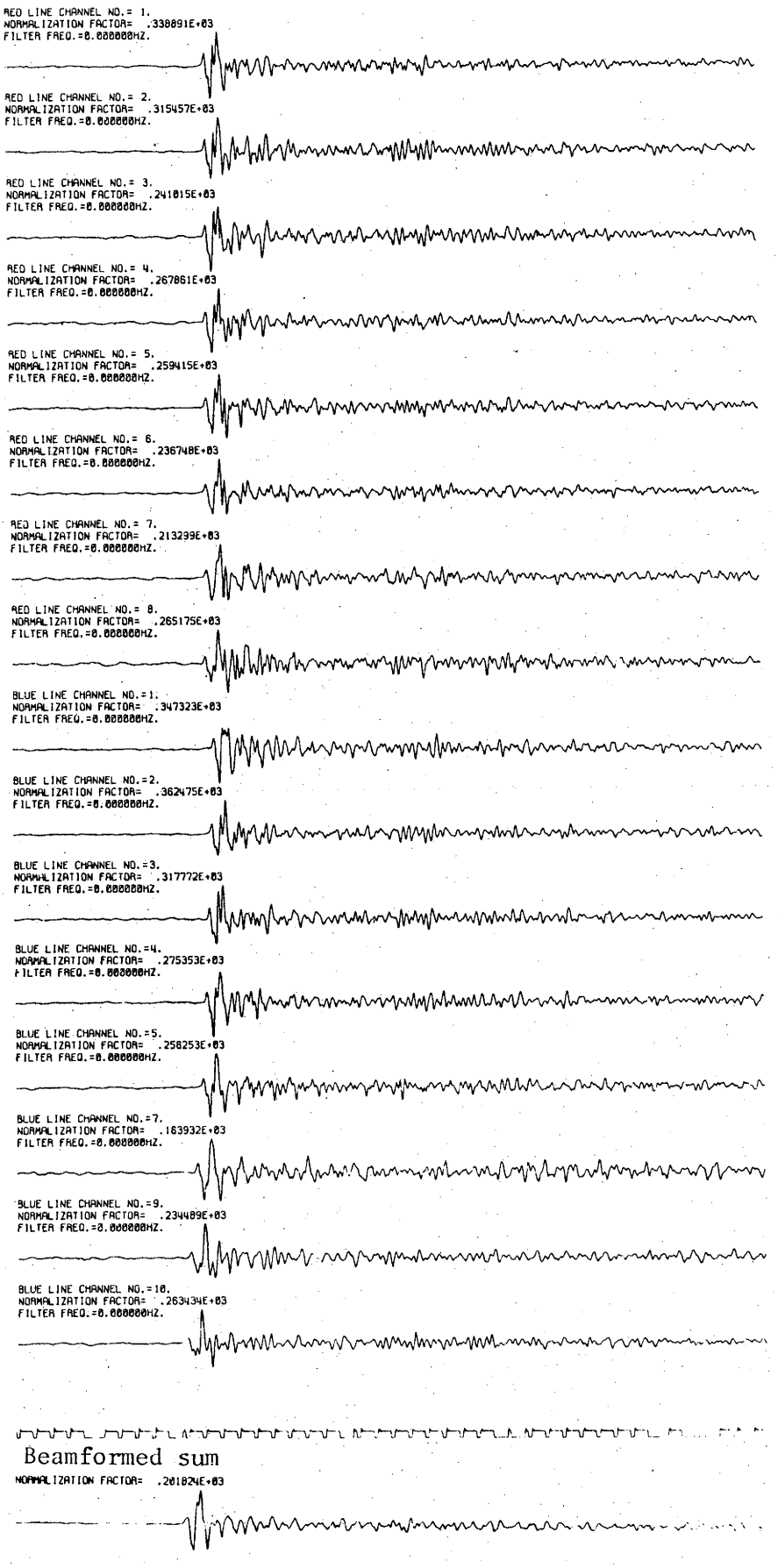

Figure 2.5 Seismogram of individual array channels, time record and beamformed trace, for P phase of Event No. 20.

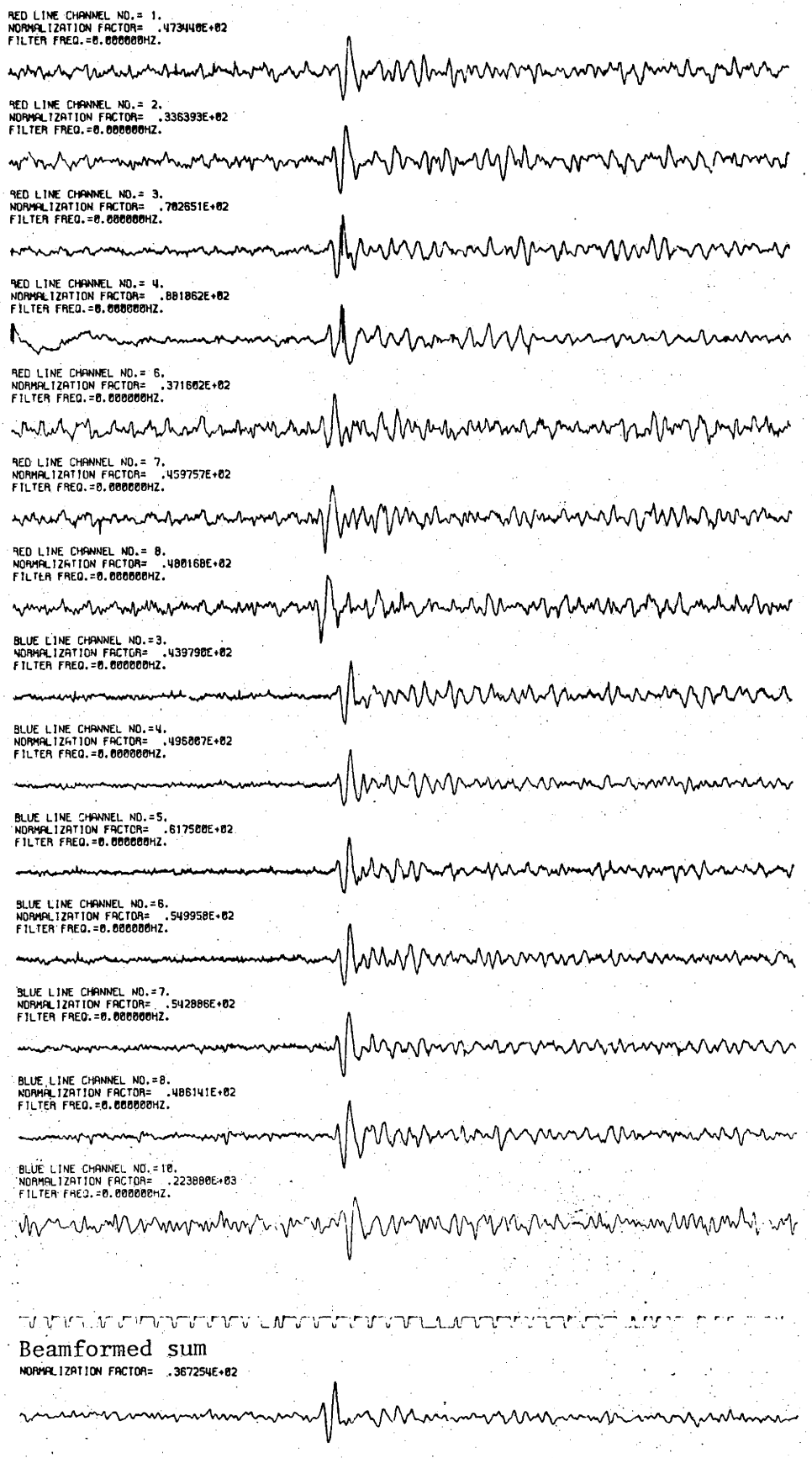

Figure 2.6 Seismogram of individual array channels, time record and beamformed trace, for P phase of Event No. 11.

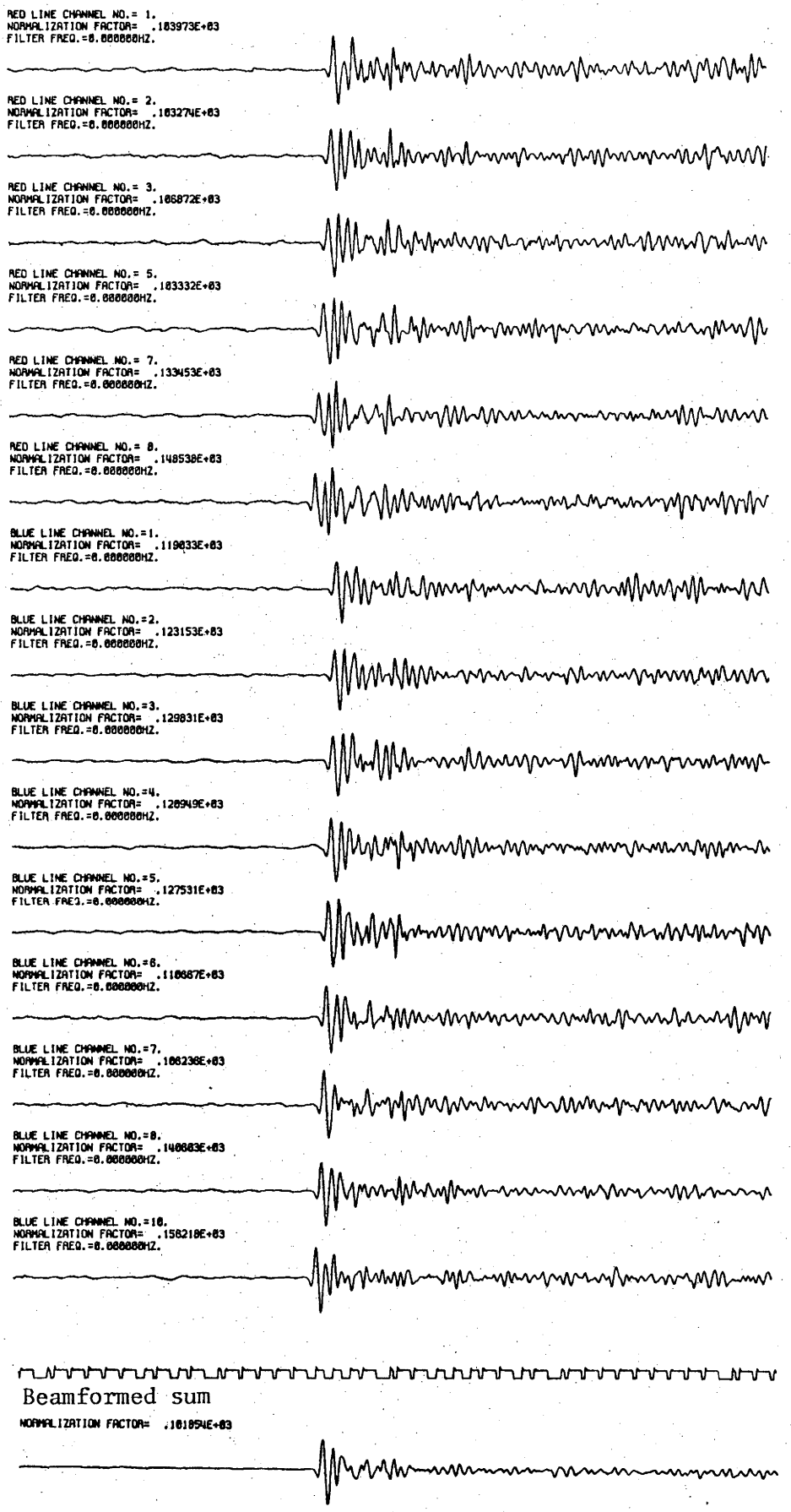

Figure 2.7 Seismogram of individual array channels, time record and beamformed trace, for P phase of Event No. 25 .

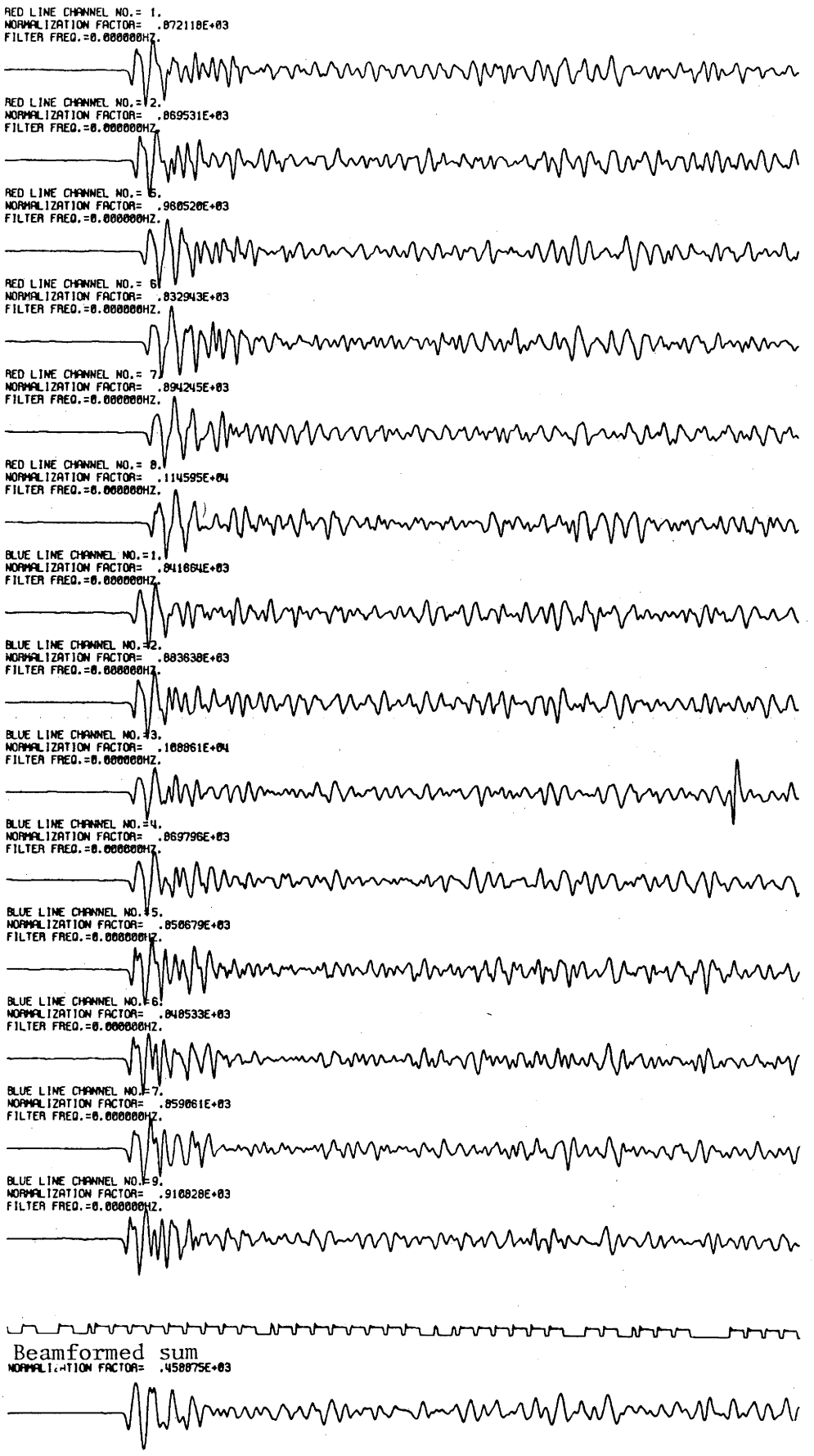

Figure 2.8 Seismogram of individual array channels, time record and beamformed trace, for P phase of Event No. 32.

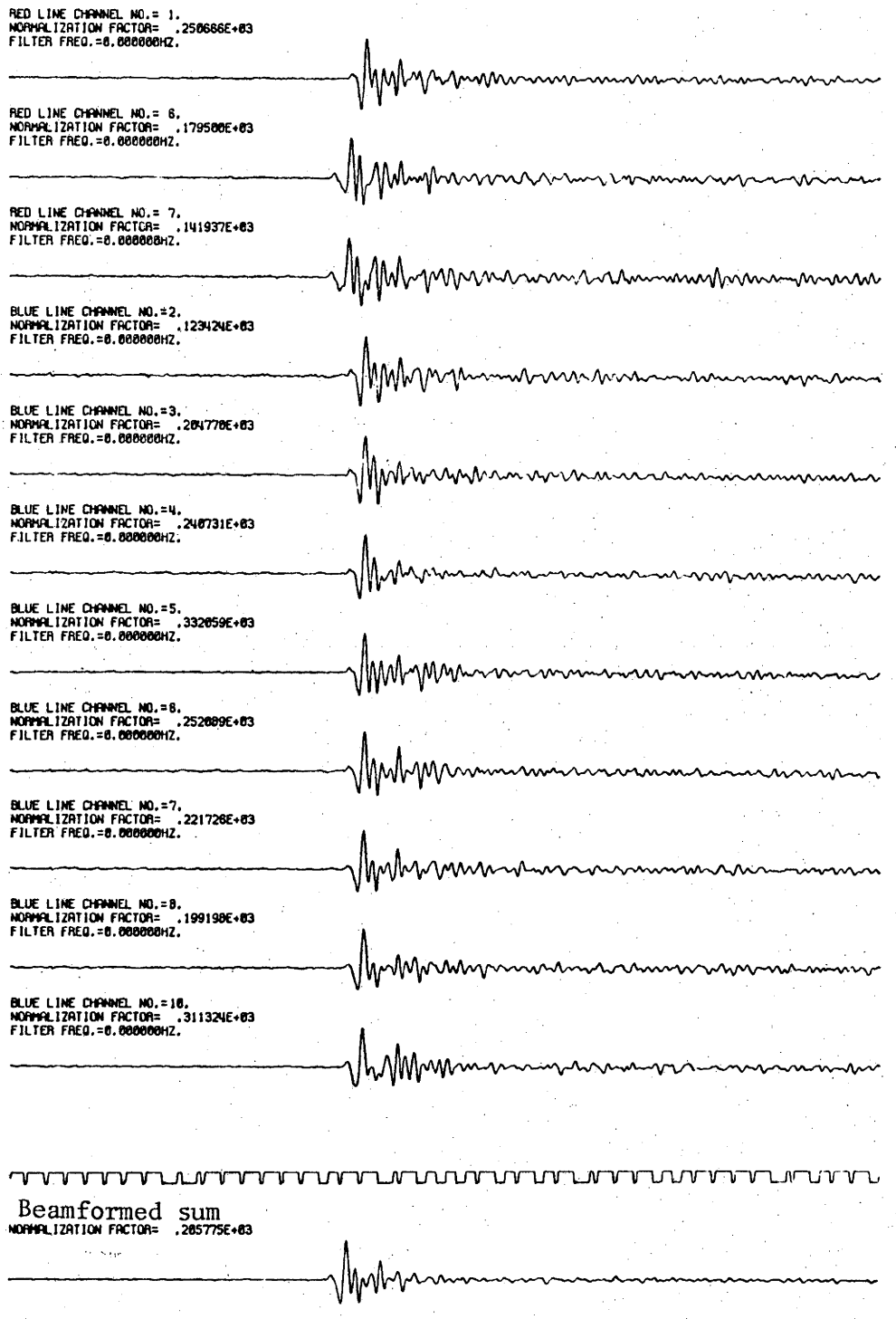

Figure 2.9 Seismogram of individual array channels, time record and beamformed trace, for P phase of Event No. 34 .

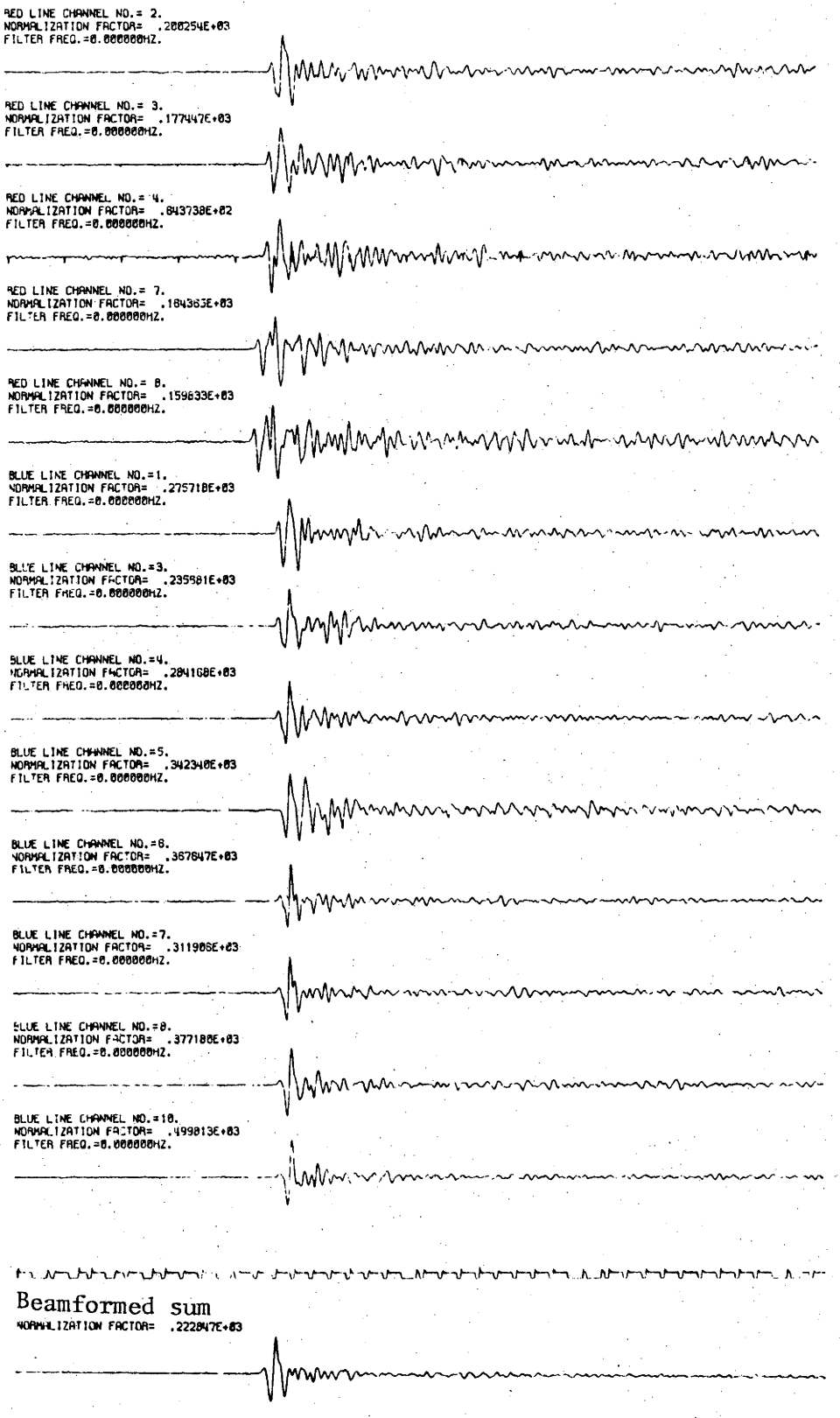

Figure 2.10 Seismogram of individual array channels, time record and beamformed trace, for P phase of Event No. 11.

CHAPTER 3

THE PHYSICS OF ATTENUATION

3.1 Introduction

If a substance is excited by a harmonic wave of elastic energy E, the substance dissipates the energy of the wave by a small amount dE per cycle. This energy loss can be defined in terms of the dissipation factor Q^{-1} (or quality factor Q)

$$\frac{2\pi}{Q} = -\frac{dE}{E} \qquad 3.1$$

where for the present it is assumed that Q is frequency independent. If in time t the initial energy E_o of the wave is reduced by this means to some value E, Equation 3.1 can be written as

$$-\int_{E_o}^{E} \frac{dE}{E} = \int_{o}^{t} \frac{2\pi}{Q} \cdot \frac{\omega}{2\pi}\, dt \qquad 3.2$$

Integrating,

$$E = E_o \exp(-\omega t^*) \qquad 3.3$$

where $t^* = t/Q$.

As a teleseismic wave passes through the earth it is attenuated by the material in its path. Because Q is not constant throughout the mantle, one must determine the Q_{AV}, or alternatively t* values, for many raypaths in order to assess the contribution to attenuation in various regions in the mantle. One method for determining the distribution of Q in the mantle will be the subject of a later chapter.

Bounds on Q_α/Q_β can be expressed to some degree in terms of rigidity μ,

bulk modulus K and density ρ. Using the propagation constant or complex wave $\bar{k}$, the phase and amplitude of a propagating body wave can be expressed as

$$\bar{k} = k + ik^* \tag{3.4}$$

or, in terms of complex compressional and shear velocities,

$$\bar{\alpha} = \alpha + i\alpha^*$$

and

$$\bar{\beta} = \beta + i\beta^*. \tag{3.5}$$

For the complex wave $\bar{k}$, the dissipation factor Q^{-1} of compressional waves and Q^{-1} of shear waves can be expressed, in terms of the above complex velocities, as follows:

$$Q_\alpha^{-1} = 2\alpha^*/\alpha$$

and

$$Q_\beta^{-1} = 2\beta^*/\beta. \tag{3.6}$$

Similarly the complex velocities can be written in terms of the complex bulk modulus $\bar{K}$, complex rigidity $\bar{\mu}$ and real density ρ:

$$\bar{\alpha}^2 = [\bar{K} + (4/3)\,\bar{\mu}\,]/\rho$$

$$\bar{\beta}^2 = \bar{\mu}/\rho. \tag{3.7}$$

Substituting Equations 3.7 into Equations 3.6, the dissipation factor for compressional and shear waves becomes:

$$Q_\alpha^{-1} = [K^* + (4/3)\mu^*]/[K + (4/3)\mu]$$

$$Q_\beta^{-1} = \mu^*/\mu. \tag{3.8}$$

Combining the above equations, the ratio of the dissipation factors for P

and S body wave phases can be written

$$\frac{Q_\alpha^{-1}}{Q_\beta^{-1}} = \left(\frac{\beta}{\alpha}\right)^2 [K^* + (4/3)\ \mu^*]/\mu^* \quad . \qquad 3.9$$

Anderson et al., (1965) plotted the quality factor ratios against the square of the body wave velocity ratios for several values of K^*/μ^*, as shown in Figure 3.1. They demonstrated that when $K^* = 0$ (which is the upper bound), Q_α/Q_β for mantle velocities is bounded as:

$$2.35 \leq \frac{Q_\alpha}{Q_\beta} \leq 2.60 \ . \qquad 3.10$$

Anderson et al., (1965) also constructed Q models for the earth on the assumptions of various Q ratios and compared experimental Rayleigh and Love wave data with the models. The Rayleigh and Love wave amplitude frequency curves calculated from the models are compared with the experimental data in Figure 3.2. As indicated by the figure, the best fit of the experimental data to the model data is given by $Q_\alpha = \frac{9}{4} Q_\beta$, implying that $K^* = 0$. They acknowledge, however, that experimental error in the data will allow values as high as $K^* = \frac{\mu^*}{2}$. Therefore the bounds for Q_α/Q_β could be as large as

$$1.8 \leq \frac{Q_\alpha}{Q_\beta} \leq 2.6 \quad . \qquad 3.11$$

Solomon and Toksoz (1970) determined, from ratios of differential t* data for P and S phases, a t_β^*/t_α^* value of 4.00 ± 0.77 at 10 seconds mid-period. The differential t* ratio divided by the mantle velocity ratio α/β gives a Q_α/Q_β range of

$$1.7 \leq \frac{Q_\alpha}{Q_\beta} \leq 2.7 \qquad 3.12$$

which is approximately the same as the estimate given in Equation 3.11.

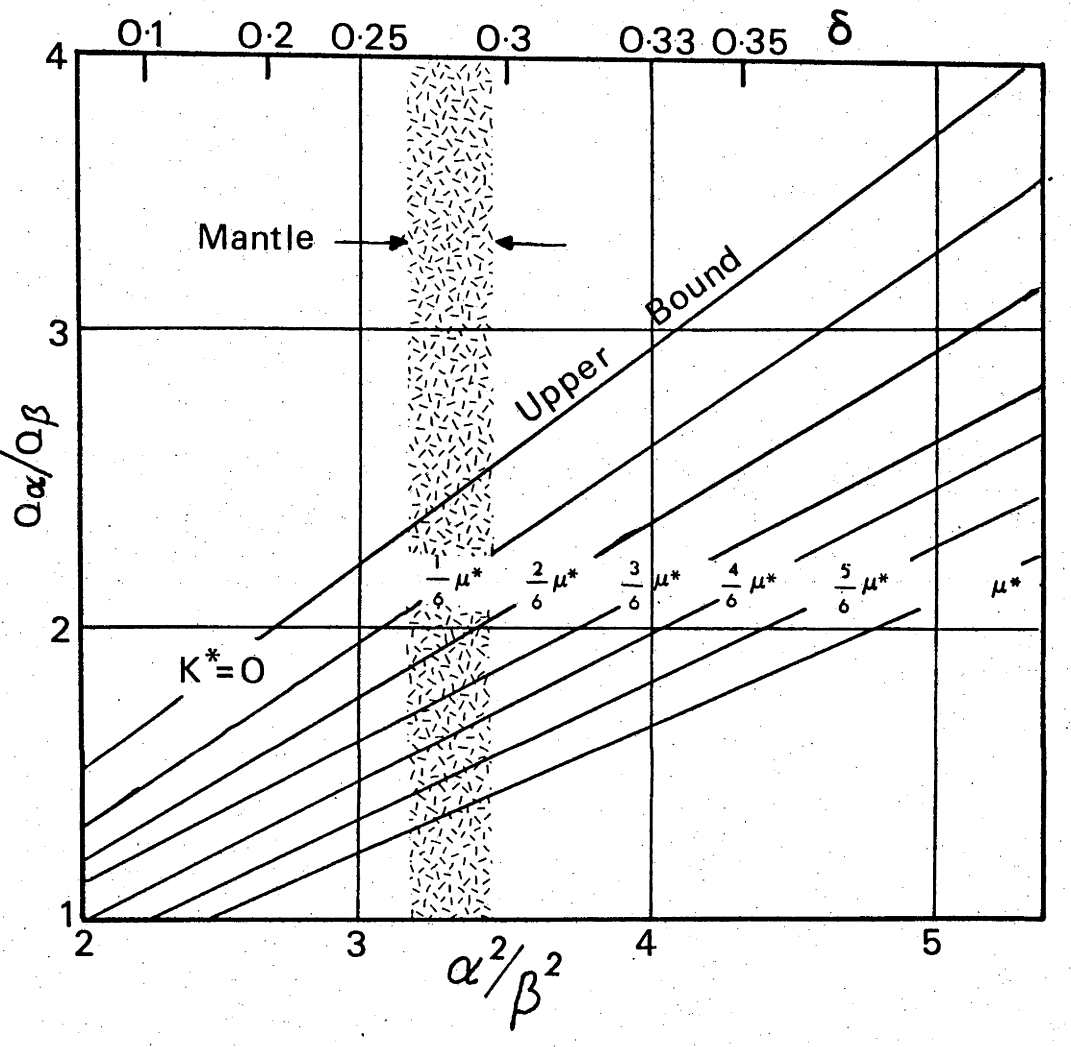

Figure 3.1 Ratio of longitudinal to shear wave quality factors as a function of the square of the longitudinal to shear wave velocity ratio with complex compressibility as a parameter. (After Anderson et al., 1965).

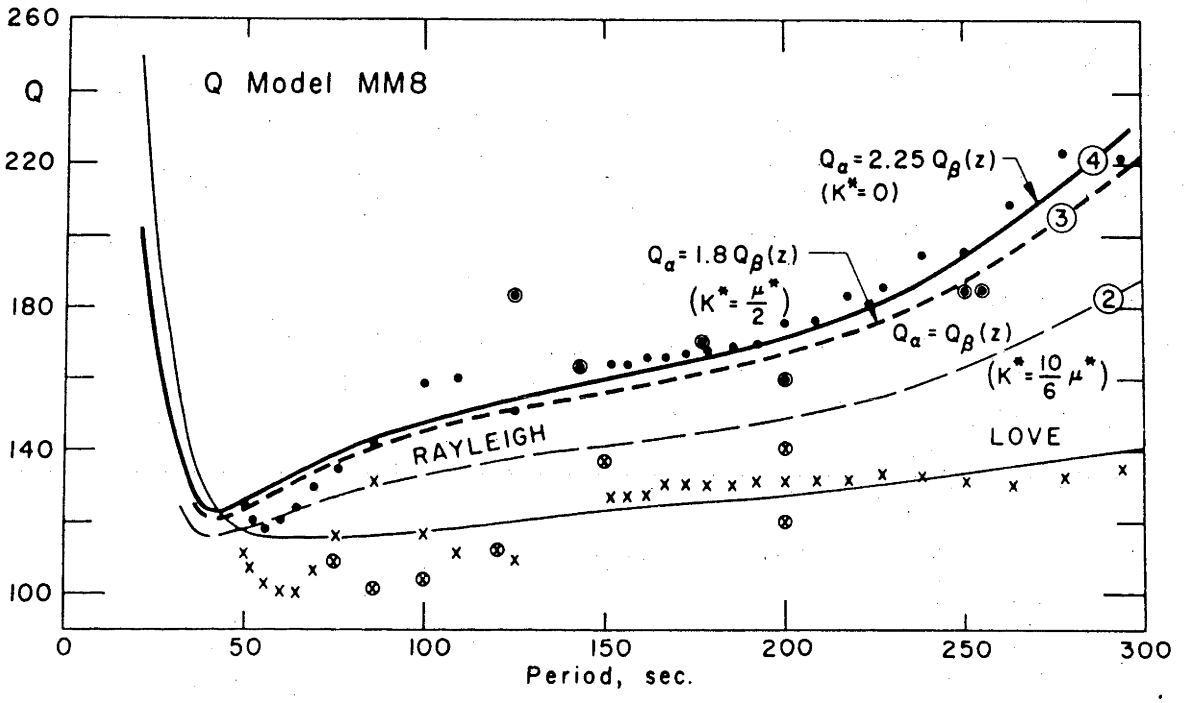

Figure 3.2 Attenuation data from Anderson et al., 1965 study for Love (X) and Rayleigh (.) waves. The circled data are from Savarensky et al., (1961), Ewing and Press (1954), Bath and Lopez Arroyo (1962), and Satô (1958). The curves are theoretical results for model MM8. (After Anderson et al., 1965).

Because there are large errors associated with both sets of data, the data are not sufficiently accurate to indicate a frequency dependence of Q. More accurate measurements need to be made at long periods in order to resolve the question. The spectral techniques discussed in Chapters 5 and 6 may be of value in obtaining more accurate Q_α/Q_β measurements at long periods in the presence of noise.

As pointed out above, a relationship $K^* = \frac{\mu^*}{2}$ for the complex bulk and rigidity moduli would imply a Q_α/Q_β less than 2.5. Since both Q's due to rigidity and bulk modulus are positive, Q_α and Q_β must satisfy

$$\frac{Q_\alpha}{Q_\beta} < 3/4\left(\frac{\alpha}{\beta}\right)^2 = \frac{1}{L} \quad . \tag{3.13}$$

Furthermore, the compressional or bulk quality factor Q_K can be expressed in terms of Q_α and Q_β and L (Anderson and Hart, 1978a,b):

$$Q_K = \frac{(1-L)\ Q_\alpha Q_\beta}{Q_\beta - L\ Q_\alpha} \quad . \tag{3.14}$$

This relationship will be discussed more fully in Chapter 7, when its implications for the data of this thesis are considered.

3.2 Mathematical Description

It has long been recognized that Q must be frequency dependent (Lomnitz, 1957a; Lamb, 1962; Jeffreys, 1965; Kogan, 1966a,b; Jackson, 1969; Jackson and Anderson, 1970; Randall, 1976). Laboratory measurements of dry solids appears to indicate a Q which is frequency independent (or nearly so) over a wide range of frequencies (Attewell and Ramana, 1966; Knopoff, 1964). Free oscillation, surface wave, and long

period body wave Q measurements do not give evidence of frequency dependence for the most part. Knopoff (1964) suggested that the various frequency-dependent Q mechanisms which occur in the earth's mantle combine to give an almost frequency-independent average Q. This mechanism-averaging hypothesis has been accepted to some degree up to the present (Liu et al., 1976). One approach has therefore been to develop a purely mathematical model in which Q is almost frequency independent, such that the principal of causality will not be violated. Using this approach various mathematical models have been developed to fit observed data (Kogan, 1966a,b: Futterman, 1962; Strick, 1967; Lamb, 1962; Kalinin et al., 1967; Azimi, et al., 1968; Gladwin and Stacey, 1974; Stacey et al., 1975). These models predict a change in phase velocity accompanying frequency-dependent Q in an absorbing media.

The principle of causality must be fulfilled before equation 3.3 is physically realizable. With a constant Q, equation 3.3. is non-causal, which would imply that an observer some distance away from a source emitting elastic energy would feel the effects of the source before the elastic energy was generated. For a pulse F(t,x) emitted from a source at a distance x, the following conditions must hold: If

$$F(t,o) = o \quad \text{at} \quad t < o$$

then 3.15

$$F(t,x) = o \quad \text{at} \quad t < o \quad .$$

The above pulse can be described in the frequency domain as

$$A(i\omega) = A_o(i\omega)\exp[-(k(\omega) + i\ \omega/v(\omega))x] \qquad 3.16$$

where $k(\omega)$ is the absorption coefficient and $v(\omega)$ is the phase velocity.

This equation gives an amplitude spectrum

$$|A(\omega)| = |A_o(\omega)| \exp(-k(\omega)x) \qquad 3.17$$

This is similar to Equation 3.3, except that now the exponential discriminate is expressed in terms of distance rather than time. The details of the term $|A_o(\omega)|$ will be discussed in Chapter 4; the main interest here is in the absorption coefficient $k(\omega)$, so for the present $|A_o(\omega)|$ will be taken as unity.

In Equation 3.16, if the absorption coefficient $k(\omega)$ is known, the phase component must meet the requirements of the Paley-Wiener condition. That is to say, if the phase velocity of a pulse travelling through a homogeneous isotropic medium is bounded by the frequency range $o<\omega<\infty$, a necessary and sufficient condition for the square integrable function $A(\omega) \geq 0$ to be the Fourier spectrum of a causal function is the convergence of the integral (Papoulis, 1962)

$$\int_{-\infty}^{\infty} \frac{|\text{Ln } A(\omega)|}{1 + \omega^2} \, d\omega < \infty \quad . \qquad 3.18$$

Because the pulse cannot exist before time zero, and assuming $|A_o(\omega)| = 1$, Equation 3.18 becomes

$$\int_{o}^{\infty} \frac{k(\omega)}{1 + \omega^2} \, d\omega < \infty \quad . \qquad 3.19$$

Therefore if the conditions given in Equations 3.15 and 3.19 are fulfilled, the described pulse is real and causal. Secondly, the pulse is of minimum phase type, in which the real and the imaginary parts of equation 3.16 are Hilbert Transform pairs. That is, if either the real or imaginary component is known, the other component can be formulated.

The above methods and conditions are general procedures for describing an appropriate mathematical model. None of the proposed models for the absorption coefficient $k(\omega)$ will be described in detail here. However, they can be placed into two general categories; either as a function of ω raised to some power (Lamb, 1962; Jeffreys, 1965; Strick, 1967; Jackson and Anderson, 1970), or as a polynomial type in terms of ω (Kogan, 1966a,b; Kalinin et al., 1967).

The choice of which type of absorption coefficient best fits the data presented in this thesis and data from other sources will be the subject of Chapter 7.

3.3 Phenomenological and Physical Descriptions

When materials are excited by acoustic energy in the laboratory, they exhibit an anelastic property known as internal friction. These materials are assumed to follow the equation for what is known as a standard linear solid, which in terms of the dissipation factor Q^{-1} is written (Zener, 1948)

$$Q^{-1} = \frac{A\tau\omega}{1 + \tau^2\omega^2} \qquad 3.20$$

where A is a constant related to the relaxed and unrelaxed moduli. Furthermore, τ is the relaxation time for the substance. It is possible for more than one physical mechanism to influence the material at one time. In such cases Equation 3.20 can be written as the summation

$$Q^{-1} = \sum_{i=1}^{N} \frac{A_i\tau_i\omega}{1 + \tau_i^2\omega^2} \quad . \qquad 3.21$$

For a seismic wave passing through material in the earth's mantle, some variation of A_i and τ_i would be expected.

Temperature and pressure may play a large role in the variation of the relaxation time τ. For a thermally activated relaxation mechanism, the relaxation time is given by the equation

$$\tau = \tau_o \exp[(E^* + PV^*)/RT] \qquad 3.22$$

which involves the activation energy E*, the activation volume V*, temperature T and pressure P. By varying the distributions of τ values in Equation 3.21, one could make any sort of frequency dependence or independence desired.

Equation 3.21 is the dissipation factor expected where there are a finite number of relaxation mechanisms; one could, however, expect a whole suite of relaxation mechanisms to be involved - effects such as atomic relaxation, grain size, etc. (Liu et al., 1976) - which would result in a continuous distribution of relaxation times. The dissipation factor for such a continuous distribution function $D(\tau)$ is

$$Q^{-1} = \int_{-\infty}^{\infty} D(\tau) \frac{\tau\omega}{1 + \tau^2\omega^2} \, d(\ell n\tau) \quad . \qquad 3.23$$

In principle, when Q^{-1} is known $D(\tau)$ can be determined (Gross, 1947). Such determinations require inversion of an integral (the right side of Equation 3.23), which can be subject to large error since Q^{-1} (the left side of equation 3.23) is not known in analytical form. This procedure is thus impractical at the present time.

Some physical models of the mantle have been proposed in the light of what is known about the attenuation, as well as other physical and chemical parameters for mantle materials. Anderson and Archambeau (1964) have proposed a thermally activated mechanism which assumes that internal friction has the form

$$Q^{-1} = C \exp[-(E^* + PV^*)/RT] \qquad 3.24$$

where E*, P, V*, R and T are the same as those in Equation 3.22. The constant C is independent of frequency. They argue that the apparent high attenuation in the upper mantle and low attenuation in the lower mantle can be explained by the variations in temperature and pressure in these regions. In the upper mantle the temperature conditions are expected to dominate, giving rise to high internal friction, whereas in the lower mantle the increase in pressure suppresses the effect of temperature, thereby reducing the internal friction.

Of the physical mechanisms likely to be important sources of attenuation in the mantle, most tend to have a strong frequency dependence. Anderson (1967) points out that a distribution of both physical and chemical properties may weaken any existing frequency dependence. For a multi-component, multiphase system with a distribution of grain sizes, an internal friction with a weak frequency dependence could be expected. Later, reviewing data on oxides at high temperatures, Jackson and Anderson (1970) found evidence, both theoretical and experimental, to support a stronger frequency dependence than previously supposed. In their thinking the most effective mechanisms seem to be those associated with partial melting, grain-boundary relaxation. This together with a high-temperature, internal-friction background obeys an equation of the form

$$Q^{-1} = (A/f) \exp[-(E^* + PV^*)/RT] \quad . \qquad 3.25$$

This is the same as Equation 3.24, except that C in the former equation is equal to A/f. As a result, the above equation predicts a quality factor Q proportional to frequency f.

Walsh (1968, 1969) discusses two models which simulate the structure of partially melted materials. The first model described the effect of

isolated lens-shaped inclusions of melt in a solid. In the second model, he considers a liquid phase which forms a continuous film of melt surrounding approximately-spherical solid grains. In Walsh's derivation of Q^{-1} for the first model it is assumed that the rigidity of the inclusion phase is small and that the dissipation factors for shear Q_β^{-1} and bulk Q_K^{-1} are proportional to the angular frequency ω. In the second model, however, Q_β^{-1} was found to be inversely proportional to angular frequency ω, and Q_K^{-1} directly proportional to ω.

Of the two models given by Walsh, the one in which the solid grains are surrounded by a thin film of melt material appears to be the most promising. Given a rock with its grain matrix randomly distributed throughout, as the rock is evenly heated under a confining pressure the first portions to melt are the contact points between the grains (Brace et al., 1967). Therefore Q_β^{-1} inversely proportional to ω seems preferable.

The bulk dissipation Q_K^{-1} directly proportional to ω derived by Walsh would imply a frequency dependent Q^{-1} for compressional waves as well. Since the rigidity and bulk modulus may vary with frequency, Q_α^{-1} would be expected to vary with frequency to some extent (Equation 3.8). This possibility was not discussed by Walsh.

As can be seen from this section, the frequency dependence resulting from internal friction can take on almost any form. It depends upon the phenomenological or physical parameters chosen to represent what occurs in the mantle. Such phenomena as grain-boundary damping, stress-induced ordering and dislocation (Gordon and Nelson, 1966) may contribute much to the overall seismic attenuation. With a combination of laboratory measurements and seismic field observations it may be possible to determine

eventually the physical nature of mantle material. Detailed knowledge of internal friction in the mantle as a function of frequency would provide information as to the possible physical mechanism. This is of course one of the objectives of this research.

CHAPTER 4

DISPLACEMENT AMPLITUDE SPECTRUM OF THE REFRACTION ARRIVALS

4.1 Introduction

The aim of this chapter is to describe the character of teleseismic records on seismograms. The recorded seismic energy can be thought of as a spike passing through a linear series of filters, which alters the transmitted energy in some way. In the frequency domain this series of filters can be written, in terms of displacement complex spectrum $A(\omega,r)$ at distance r, as follows:

$$A(\omega,r) = S(\omega)B(\theta)C_s(\omega)G(r)C_r(\omega,r)M(\omega,r)R(\omega,r)I_v(\omega)\omega \exp i(\pi/2) \qquad 4.1$$

where $S(\omega)$ = source spectrum, which corresponds to a source time function

$B(\theta)$ = source space function, where θ is direction

$C_s(\omega)$ = the effect of crust at the source on the source spectrum

$G(r)$ = geometrical spreading

$C_r(\omega,r)$ = the effect of crust at the receiver on the spectrum

$R(\omega,r)$ = reflection coefficients

$I_v(\omega)\omega \exp i(\pi/2)$ = instrumental displacement response

$M(\omega,r)$ = attenuation effects of the mantle.

Another term due to microseismic noise may be added to the above equation. However, this term will not be considered in the present discussion.

Equation 4.1 can also be written in terms of the amplitude and phase spectrum. The equation then becomes

$$|A(\omega,r)| = |S(\omega)||B(\Theta)||C_S(\omega)||G(r)||C_r(\omega,r)||M(\omega,r)||R(\omega,r)||I_v(\omega)||\omega| \qquad 4.2$$

and

$$\Phi_A = \Phi_S + \Phi_P + \Phi_I \pm 2\pi n \qquad 4.3$$

where Φ_A = phase of system

Φ_S = phase of the source

Φ_P = phase of the path, which includes effects of crustal response at the source and receiver, as well as reflection coefficients which may be frequency dependent

Φ_I = phase of the instrument.

Throughout most of this thesis, the main concern will be the power spectrum, which is simply the square of Equation 4.2. The phase spectrum is not important unless it becomes desirable to transform the amplitude spectrum back into the time domain, as in the construction of synthetic wavelets. In such cases the phase portion of the amplitude spectrum should be retained. Since the concern is to determine how the power spectrum changes with frequency, the linear terms in equation 4.2. are not of interest because they only contribute to the magnitude of the intercept value at zero frequency. These terms are the source space function $B(\theta)$, and geometrical spreading $G(r)$, which will therefore not be discussed further. It is also assumed the reflection coefficients are frequency independent when applicable. The attenuation response function $M(\omega,r)$ has been previously discussed in Chapter 3.

4.2 Removal of Spectral Responses

4.2.1 Instrument Response

Short period seismometers are not designed with attenuation studies in mind. They are designed to magnify high frequencies and suppress low

frequencies, in order to reduce the low frequency microseismic noise and give rise to sharp phase onsets unobscured by low frequency noise. While this type of distorting response has great advantages in both detection and travel time studies, a broad-band instrument with a wide flat frequency response would be more useful for attenuation studies. Nevertheless, the distorting frequency response of the instrument can be easily removed. Since the seismometer can be described as a simple mechanical system, its frequency response for a velocity spectrum can be written as

$$I_v(\omega) = |I_v(\omega)| \exp(i\Phi(\omega)) \qquad 4.4$$

where the amplitude response to the particle velocity at the earth's surface is

$$|I_v(\omega)| = \frac{K(f/f_n)^2}{[(1 - (f/f_n)^2)^2 + \zeta^2(f/f_n)^2]^{\frac{1}{2}}} \qquad 4.5$$

and its phase is

$$\Phi(\omega) = \tan^{-1} \frac{1 - (f/f_n)^2}{2\zeta(f/f_n)} \quad . \qquad 4.6$$

For the WRA array, the resonant frequency f_n of all seismometers is 1.0 Hz, with a damping constant ζ of 0.64. The magnification term K is identical for all the instruments. Using the above values the velocity amplitude and phase response functions are shown pictorially in Figures 4.1 and 4.2 respectively.

In general, after the amplitude or power spectrum of the portion of the seismograph is obtained the displacement response of the instrument is removed, so that the resulting spectrum is in terms of ground displacement.

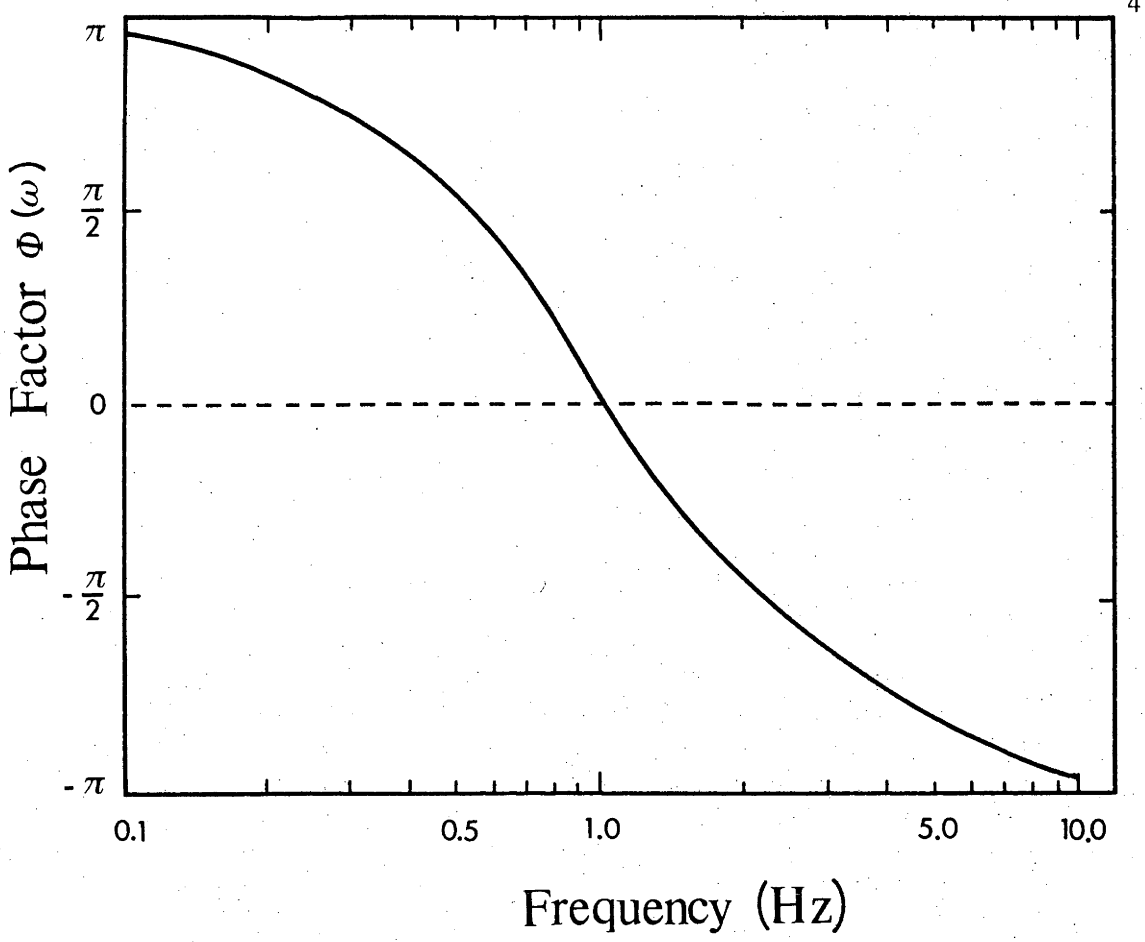

Figure 4.1 Seismometer velocity phase response.

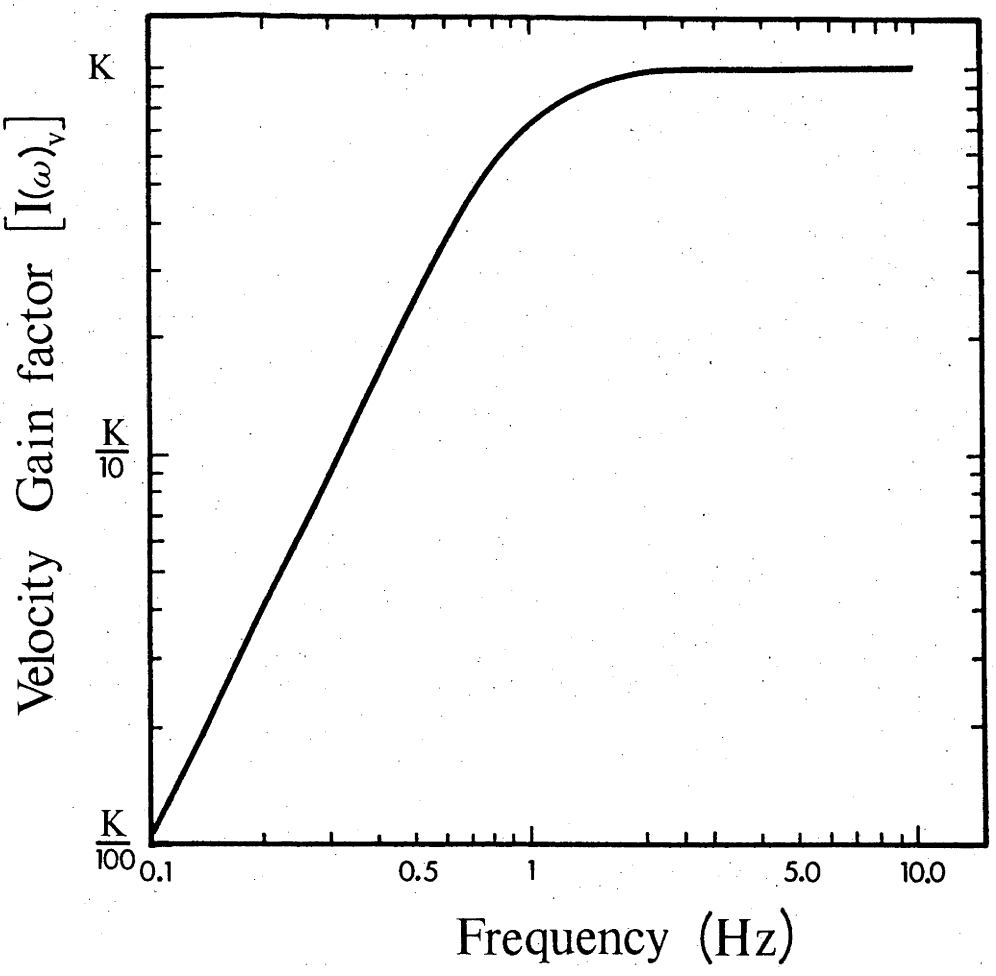

Figure 4.2 Seismometer velocity response.

In this case the best procedure is to remove the instrumental velocity response from the spectrum first. The extra ω in Equation 4.2 will be taken out with the source function. The advantage of doing so will become obvious in the next section.

4.2.2 Source Spectrum

In recent years much work has gone into determining the parameters of an earthquake source function, in particular its displacement spectrum. Despite all this effort, the source spectrum is still not well known, expecially at high frequencies.

Hanks and Wyss (1972) have shown in the application of Parseval's theorem that the high-frequency asymptotic behaviour of the source spectrum must involve a ω^n term, where n is at least -1.5 in magnitude. As pointed out by Randall (1973), if n is greater than -2 the time function of the source would involve an infinite discontinuity in velocity. Non-integer values of n would not be expected in a physical situation because the time function would have branch point singularities. Two possibilities have been considered in the literature: (1) n = -2 (Haskell, 1964; Aki, 1967; Brune, 1970, 1971; Wyss and Hanks, 1972; Hanks and Wyss, 1972) and (2) n = -3 (Savage, 1966; Frasier and North, 1978). The ω^{-2} model is most favoured because it implies a finite jump in velocity at the source. In this case, relaxation of the stress field in the source region would appear as a stress discontinuity, which gives rise to a wave front carrying a finite jump in velocity. In support of this, Aki (1967) tested the ω^{-2} and ω^{-3} models against experimental data, and his results gave a better fit for the ω^{-2} model. Theoretical considerations (Madariaga, 1977) for starting and stopping phases give a ω^{-2} high frequency asymptotic behaviour.

The ω^{-2} model seems to fit most data, both for very low stress-drops (Douglas and Ryall, 1972) and high stress-drops (Tucker and Brune, 1973). Also the ω^{-2} model has been applied to large earthquakes (Hanks and Wyss, 1972; Wyss and Hanks, 1972) with a high degree of success. Analytically the far-field displacement spectrum of square law theory is simple to apply to experimental spectra. Throughout this thesis, therefore, where a source model is required the ω^{-2} model will be used.

Brune's displacement spectrum $|S(\omega)|$ for the stress-drop source function is

$$|S(\omega)| = \frac{S(0)}{\omega_c^2 + \omega^2} \qquad 4.7$$

where $S(0)$ is an expression for the magnitude of the earthquake and ω_c is the corner frequency. It is difficult to determine accurately the corner frequency by just considering the displacement spectrum. This is especially true when effects of attenuation are involved.

If the velocity spectrum of the source is considered rather than the displacement spectrum, the problem can be partially circumvented. The square law velocity spectrum for a stress-drop source is

$$|S_v(\omega)| = \frac{\omega S(0)}{\omega_c^2 + \omega^2} \quad . \qquad 4.8$$

By differentiating Equation 4.8 with respect to ω, it can be shown that the velocity at the source is a maximum when

$$\omega = \omega_c \quad . \qquad 4.9$$

Therefore the corner frequency is accurately determined by the peak of the velocity spectrum.

According to Brune's stress-drop source theory, the ratio between the corner frequency of the P phase and the corner frequency of the S phase for the same earthquake should equal the ratio of their velocities, as shown in Figure 4.3 (Hanks and Wyss, 1972). For the earth's mantle, the ratio of V_α to V_β should lie between 1.76 and 1.80 (Anderson et al., 1965) or approximately $\sqrt{3}$.

Power spectra, to be discussed in the next two chapters, were determined for the P and S phases of the events listed in Table 2.2. After the instrument responses (Equations 4.5 squared) were removed from each of the raw spectra the maximum values (or peak values) of the resulting spectra were determined. These are listed in Table 4.1 along with their respective P-to-S corner frequency ratios. Only those events with poor signal-to-noise or system drop-outs were omitted from the determination given in Table 4.1. Note that the mean value of these events lies close to the $V_\alpha : V_\beta$ velocity ratio given by Brune's theory (Fig. 4.3), eventhough the standard error of the mean is quite large. The scatter in the corner frequency determinations could be caused by dipping layers (azimuth anomalies) at the receiving station (Kasahara, 1960). Other probable causes are variations in the epicentral distance and earthquake depth.

4.2.3 Crustal Response

In all work dealing with body wave Q measurements, the effect of the crust under the receiving station should be removed from the seismic wavelet before it is analysed. This is not always possible, however, because of limited knowledge of the effect of the crust. Underwood (1967) made a preliminary study of the crustal layering under WRA. His model for the first 2 layers, and the last two layers assumed by Barley (1977),

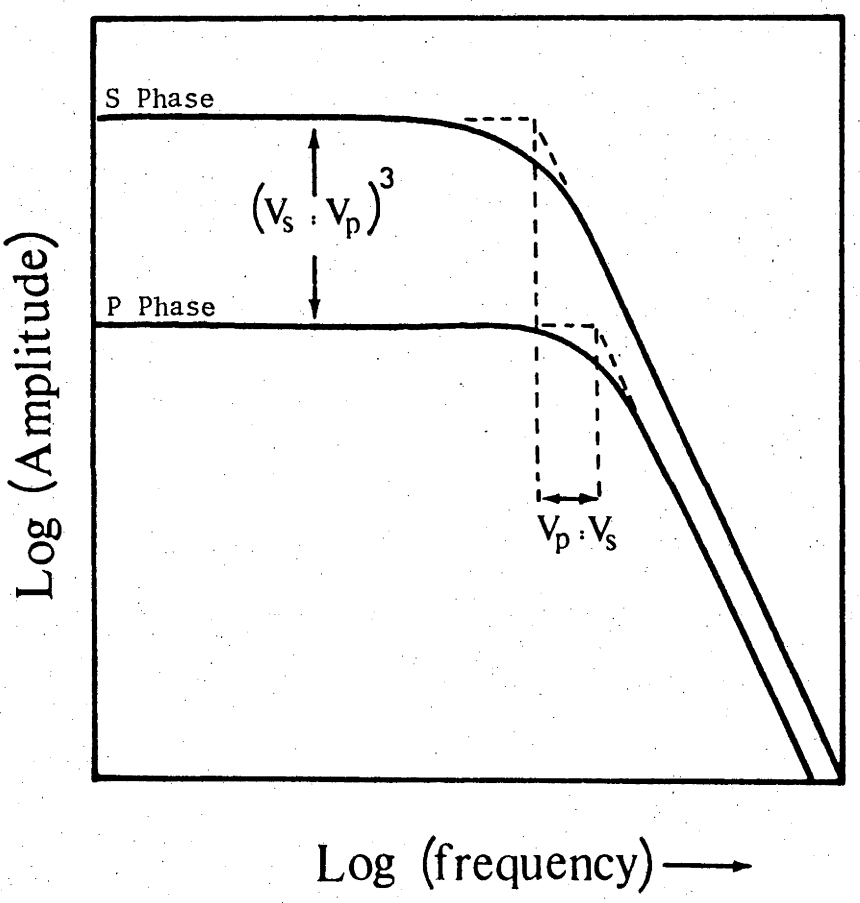

Figure 4.3 Brune's Source Spectrums for P and S phases (after Hanks and Wyss, 1972).

Table 4.1

P and S Corner Frequencies (C.F.) and their Ratios for Events listed in Table 2.2

Event No.	Magnitude (M_b)	P_{CF}	S_{CF}	P_{CF}/S_{CF}
1	5.3	1.59	0.90	1.77
2	5.8	-	1.13	-
3	5.1	0.87	0.81	1.07
4	5.2	1.63	0.76	2.14
5	-	-	-	-
6	5.4	1.67	1.07	1.56
7	5.8	-	0.61	-
8	5.4	1.24	0.85	1.46
9	5.5	1.09	0.66	1.65
10	5.0	1.67	0.73	2.29
11	5.2	1.20	0.97	1.24
12	5.8	0.94	0.68	1.38
13	5.7	0.91	1.18	1.30
14	-	-	-	-
15	5.0	1.25	0.85	1.47
16	4.9	-	1.01	-
17	5.2	-	-	-
18	5.2	1.44	0.66	2.18
19	5.5	0.84	0.57	1.47
20	5.4	1.40	0.87	1.61
21	5.8	1.61	0.47	3.43
22	5.3	0.90	-	-
23	5.0	0.73	0.92	0.78
24	5.2	0.99	0.65	1.52
25	5.1	1.56	0.76	2.05
26	5.5	1.69	0.48	3.52
27	5.3	-	-	-
28	5.8	1.05	0.58	1.81
29	4.8	1.09	-	-
30	4.5	-	-	-
31	5.4	1.70	0.65	2.62
32	5.1	1.48	1.01	1.47
33	5.8	0.92	0.65	1.42
34	5.1	1.34	0.77	1.74
			Mean	1.79 ± 0.66

are given in Table 4.2. It is not known how valid this model is, since the first two layers are based on only one refraction profile.

Only recently, some horizontal instruments have been installed at the array. These instruments combined with the vertical instruments should make it possible for a study of the transfer function of the crust to be undertaken (Bath, 1974). Because of insufficient horizontal data and time, the present author could not embark on this study. It is assumed here that local geological effects are smoothed by stacking the array as discussed in Section 2.2 of this thesis (Mack, 1969). Interference caused by reflected phases (echos) and refracted converted phases will be considered in Chapters 5 and 6.

4.3 Seismic Noise Structure and Its Influence on Spectra

The earth is never quiet. Noise generated from many sources is always present. In the short-period seismic band such noise arises mainly from Rayleigh and Love waves which are created by local conditions. Road traffic, trains and wind may contribute to the microseisms which exist in various localities. Noise can also be created by unidentified microearthquakes, multipathing and storms. Observations of seismic phases which arrive after the beginning of the earthquake record are contaminated by converted phases, signal-generated surface waves, scattered waves and waves reflected by and in the crust which contribute to the noise background.

Deconvolution of noise from signals has been studied for many years (Weiner, 1949; Burg, 1967; Capon et al., 1967; Kulhánek, 1968; Dash and Obaidullah, 1970; Lacoss, 1971; Capon, 1973). Difficulties arise when the noise is non-white and non-stationary, since most spectral techniques assume stationary random signals. Seismic noise cannot be considered either

TABLE 4.2

The Receiver Crustal Model assumed by Barley (1977) for WRA. $\alpha/\beta = \sqrt{3}$ ($\sigma = 0.25$) was assumed in each layer. Underwood (1967) determined $\alpha = 5.4 km.s^{-1}$ in Layer 1, $\alpha = 6.1 km.s^{-1}$ in Layer 2 from a refraction survey.

	α ($km.s^{-1}$)	β ($km.s^{-1}$)	ρ ($gmcm^{-3}$)	Thickness (km)
Layer 1	5.4		2.8	1.0
Layer 2	6.1		3.1	20.0
Layer 3	6.3		3.2	20.0
Layer 4	8.2		3.3	∞

white or stationary. If the data sequence under study is not random and stationary, only an estimate of the actual amplitude or power spectra can be obtained. The problem then becomes: which spectral method gives the best estimate of the actual spectrum with the noise removed? High resolution techniques have been developed in an attempt to eliminate noise (Burg, 1967; Capon, 1973; Ulrych and Bishop, 1975). These techniques, along with the more conventional Fourier spectral techniques, are examined in the next two chapters.

4.4 Relationships between Seismic Wave Energy, Magnitude and Corner Frequency

Early in the history of seismology, attempts were made to estimate the energy of an earthquake on the basis of some quantity measurable on seismograms (Richter, 1958). The square of the recorded seismic phase amplitudes at a fixed predominant period would be expected to be related to elastic wave energy leaving the source. If attenuation can be neglected, the recorded seismic amplitudes would therefore be proportional to the earthquake magnitude. Mathematically the relationship between earthquake energy (E) and its body-wave magnitude (M_b) can be written as

$$\log E = a + bM_b \qquad 4.10$$

where a and b are constants. In general, however, the predominant period on a seismogram is not fixed, making the above equation difficult to use.

Effort then was directed to a correlation between the predominant periods (T) (or more recently the source corner periods) and earthquake magnitudes. Furuya (1969) theoretically determined earthquake energy released from the ω^{-3} and the ω^{-2} source amplitude displacement models of Haskell (1966) and Aki (1967) respectively. He found that for both models

the released energy (E) has the general form

$$\log E = \log C_o + 2 \log C + 3 \log T \qquad 4.11$$

where C is equal to twice the stress drop divided by the rigidity and C_o is a function of the rupture, compressional and shear velocities, and density. Equating Equations 4.10 and 4.11, the relationship between the corner period (T) and the earthquake magnitude (M_b) becomes

$$\log T = \frac{1}{3} \log C_o + \frac{a}{3} - \frac{2}{3} \log C + \frac{b}{3} M_b \qquad 4.12a$$

or, in terms of frequency f,

$$\log f = \frac{1}{3} \log C_o - \frac{a}{3} + \frac{2}{3} \log C - \frac{b}{3} M_b \qquad 4.12b$$

since $f = 1/T$.

If attenuation effects are taken into account, a fifth term f(r) is added to Equation 4.12a,b which is a function of the attenuating ray path. Therefore as the attenuation due to the raypath increases, the "apparent" corner frequency will decrease for a given magnitude. The actual corner frequency becomes impossible to separate from source properties unless the attenuation properties are known.

Because it is preferable here to discuss the magnitude in terms of the corner frequency and the separation between source and attenuation properties, Equation 4.12b can be empirically written as

$$\log f = a' + b' M_b \qquad 4.13$$

Terashuna (1968) found, for microearthquakes ($M_b < 3$), $b' = -0.47$ and $a' = 1.79$ whereas Kasahara (1957) found, for large earthquakes ($M_b < 6.3$), $b' = -0.51$ and $a' = 2.59$. Using a range of magnitudes from 0 to 8, Furuya (1969) found a' and b' to be 1.6 and -0.43 respectively for P phases and 1.2 and -0.40 respectively for S phases.

The corner frequencies presented in Table 4.1 for the P and S phases are plotted in Figure 4.4 and 4.5. Since the magnitude range for these data is limited, a least squares fit could not be made. Assuming that the slope of Equation 4.13 given by Furuya is correct, a comparison of his equation (solid line) was made with the data in this study. The dashed lines are "visual" fits of the data. In the case of both S and P corner frequencies, the intercept a' is about -0.8 units higher than the values given by Furuya. The corner frequencies of the ScP phase data (Table 4.3) are plotted in Figure 4.6. Again the intercept value a' is much higher than the one given by Furuya and possibly higher than the S phase data. Since not many PcP phases are represented in Table 4.2, a plot of these data was not made. However, four out of the five corner frequencies indicate a greater intercept value a' than the P phase corner frequencies presented here.

The conclusion which can be drawn is that the attenuation factor for the data is much less than in the study of Furuya. This is not surprising since Furuya's study was in Japan. Under island arcs large low Q zones, presumably due to magma chambers exist (Oliver and Isack, 1967; Mitronovas et al., 1969; and Barazangi and Isack, 1971). However, WRA is in a shield region, where low Q zones are either weak or absent (Der and McElfresh, 1977). As a result, the corner frequencies presented in this thesis should be much closer to the actual corner frequencies than in Furuya's study. Furthermore, because the corner frequencies of the average ScP and PcP phase seem to be higher than for S and P phases respectively, Q in the lower mantle would be expected to be large.

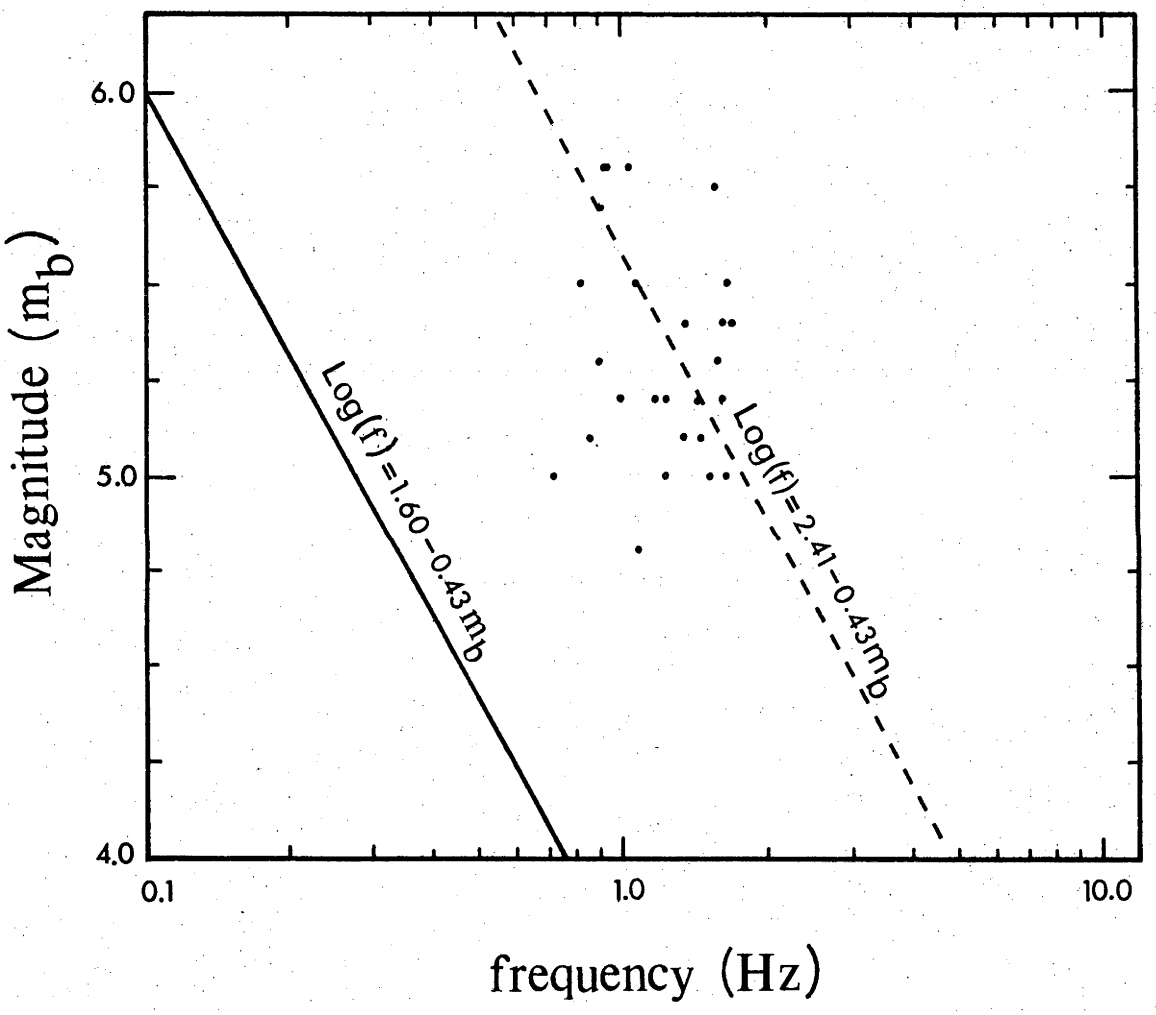

Figure 4.4 Magnitude vs. frequency for P phases given in Table 4.1.

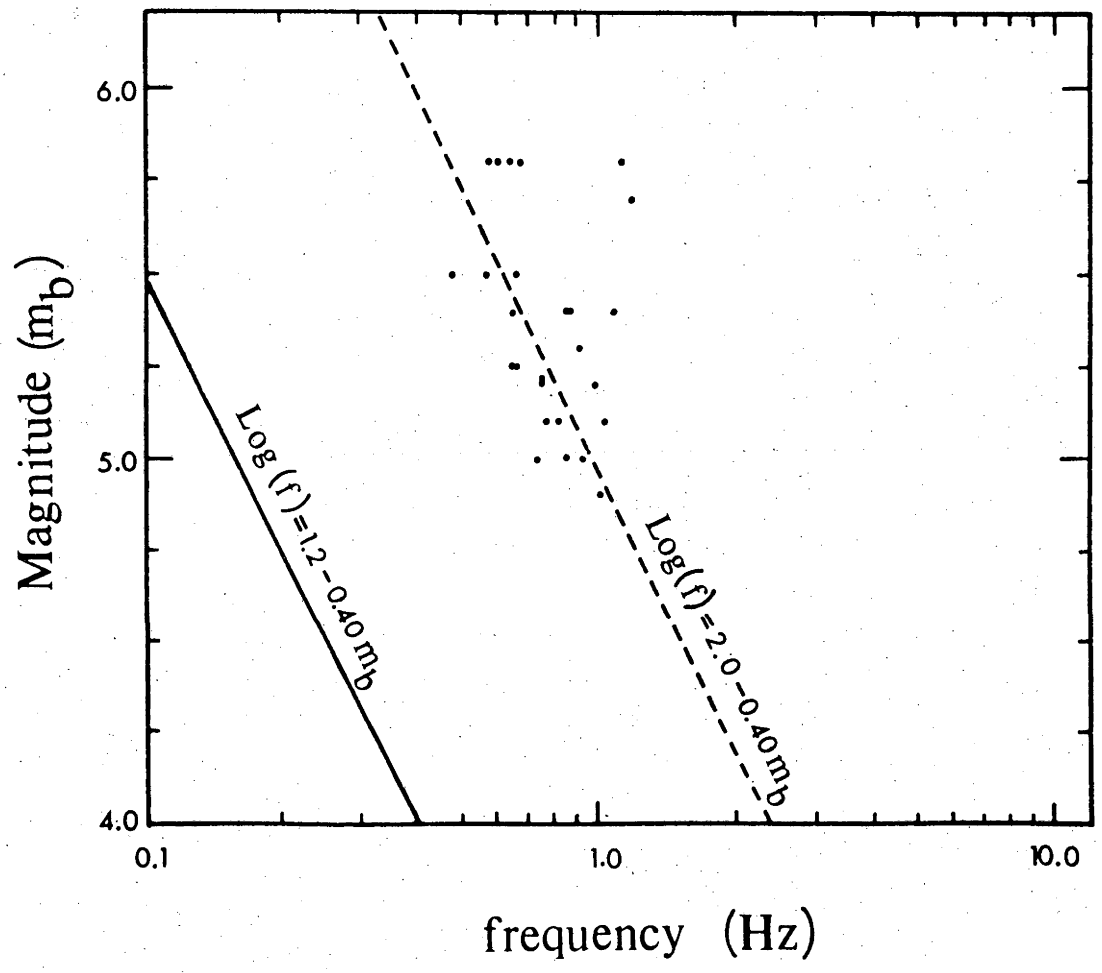

Figure 4.5 Magnitude vs. frequency for S phases given in Table 4.1.

TABLE 4.3

ScP Corner Frequencies (C.F.) for Events Listed in Table 2.1

Event No.	Magnitude (M_b)	PcP_{CF}	ScP_{CF}
1	5.3		1.01
2	5.8		0.98
3	5.1		0.74
4	5.2		1.01
5	-	-	-
6	5.4		1.33
7	5.8		0.74
8	5.4		1.24
9	5.5		0.80
10	5.0		0.90
11	5.2		1.21
12	5.8		0.81
13	5.7		1.14
14	-		-
15	5.0		0.81
16	4.8		0.95
17	5.2		0.61
18	5.2		0.81
19	5.5		1.05
20	5.4		0.68
21	5.8	0.91	0.63
22	5.3	1.40	-
23	5.0		0.85
24	5.2	1.10	1.13
25	5.1		1.11
26	5.5		0.99
27	5.3		0.81
28	5.8	1.11	1.09
29	4.8	1.18	0.95
30	4.5		0.84
31	5.4		0.64
32	5.1		1.06
33	5.8		0.79
34	5.1		0.72

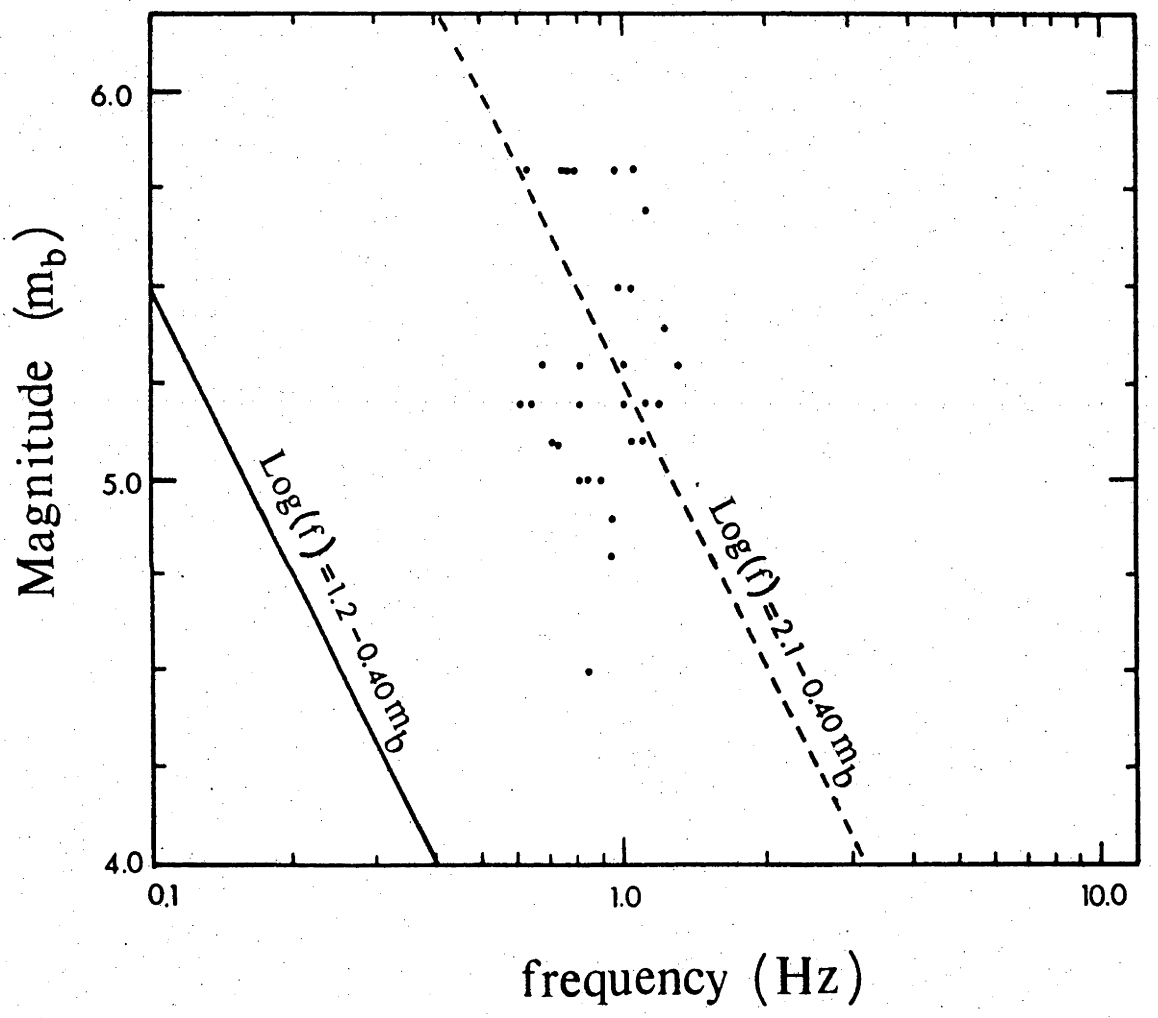

Figure 4.6 Magnitude vs. frequency for ScP phases given in Table 4.3.

CHAPTER 5

SPECTRAL ANALYSIS (UNSUCCESSFUL METHODS)

5.1 Introduction

The question as to the particular analytical technique which should be used to obtain the most information from a seismic wavelet has long been an outstanding problem in seismology. This chapter addresses itself to this problem, and in particular, to whether the time domain or frequency domain approach provides the best and most reliable information. In Section 5.2, the discussion will be centered around the advantages and disadvantages of both (time and frequency domain) techniques. As will be explained, the frequency domain approach is believed to be more appropriate for the type of analysis contained in this thesis.

Following Section 5.3 the remainder of the chapter will be devoted to the spectral techniques which proved to be unsuccessful in determining spectral power versus frequency of a seismic wavelet. As well as the more conventional Fourier spectral techniques, the autoregressive techniques of Yule-Walker (Ulrych and Bishop, 1975) and Burg's Maximum Entropy Method (Burg, 1967) will be discussed. After a discussion of the theory for each of these techniques, the methods will be tested through examples to demonstrate why they fail to give a reasonable estimate of spectral power.

5.2 A Comparison of Time and Frequency Domain Analysis

In order to compare the advantages and disadvantages of analysis in the time and frequency domains, synthetic transient signals will be examined. Starting with a simulated earthquake pulse $F(t,0)$ this pulse will be

modified by the transmission path so that when it arrives at a measuring instrument it will be F(t,x). The Fourier transform of such a pulse, as previously discussed in Chapter 3, will be

$$A(i\omega) = A_o(i\omega)\exp[-k(\omega) + i\phi(\omega)]x \qquad 5.1$$

where $A_o(i\omega)$ again is a function of the source spectrum, instrument response, etc., as discussed in Chapter 4. $k(\omega)$ is the real part of the attenuation function and $\phi(\omega)$ is its phase component. Now suppose that all the responses which make up $A_o(i\omega)$ can be easily represented in the time domain. This leaves only the response due to the attenuation portion of the pulse to be evaluated. As pointed out in Chapter 3, both $k(\omega)$ and $\phi(\omega)$ must be frequency dependent in order to fulfil the Paley-Weiner condition. If the attenuation for a path is unknown then $k(\omega)$ and $\phi(\omega)$ are both unknown, so that one is left with a trial-and-error approach to try to resolve the time domain counterparts for $k(\omega)$ and $\phi(\omega)$. This can be very difficult, especially when the pulse is received in a noisy environment. Small perturbations of a synthetic pulse which represents the real pulse may be mistakenly regarded as noise.

The problem is made much simpler in the frequency domain because $\phi(\omega)$ can be eliminated when the amplitude or power spectra are considered for determining the attenuation of the pulse travelling through the earth. As shown in Chapter 3, multiplying Equation 3.16 by its complex conjugate,

$$|A(\omega)| = |A_o(\omega)| \exp[-2k(\omega)]x \qquad 5.2$$

which is independent of $\phi(\omega)$. Once the relationship of $k(\omega)$ as a function of frequency is determined, the phase portion $\phi(\omega)$ can be determined by use of the Hilbert transform. The method employed to find the frequency

dependence will be discussed in Chapter 7. The advantage of using power spectral estimates will then become even more obvious.

An apparent advantage of using time domain methods is that a synthetic wavelet can be produced which looks very similar to a real seismic wavelet. Such methods, however, generally require trial-and-error estimates of the corner frequency and attenuation coefficient. This procedure can be very time-consuming. For this reason and other reasons given in this section the frequency domain approach will be used.

5.3 Seismic Phases Used to Demonstrate Spectral Methods

To obtain a good spectral estimate of a time series, the estimator depends on the type of time series under consideration. These types of time series can be autoregressive (AR), moving average (MA), or some mixture of AR and MA. If the specific type of time series is unknown, as in the case of seismic phases, one can approach the problem by attempting to fit the time series by several spectral methods which will be described in the succeeding sections. As a starting point, a synthetic time series can be designed from the spectral responses given in Chapter 4. Assuming for the present that the attenuation coefficient ωt^* (Chapter 3) is real with zero phase shift, a synthetic time series can be produced which is analytically exact. Therefore the time domain and frequency domain solutions are analytically an exact Fourier pair.

Four beamformed seismic traces of the P phase, arbitrarily chosen from the earthquakes listed in Table 2.2, are presented in Figure 5.1. Using the criterion given in the previous paragraph, four similar synthetic wavelets were made to be representative of the response produced by these

earthquakes and are also presented in Figure 5.1. These synthetic wavelets will be used to demonstrate the effectiveness of the spectral techniques presented in the following sections. If the spectral power spectra derived from these synthetics fit the power spectra analytically derived from these synthetic wavelets, it will be assumed the spectral method is appropriate for determining t* values of real seismic phase responses.

5.4 Fourier Power Spectral Density

5.4.1 Theory

There have been many computer programs written to estimate the power density of a time series. These programs use many different types of windowing functions and smoothing procedures. The designer of such a power spectrum estimator relies upon his personal preference and on the type of signal he is analysing to determine what parameters are required to give the best power estimate. Comparisons of some of the various methods of obtaining power spectral estimates can be found in Jenkins and Watts (1968). The technique used here was a periodogram with a cosine bell taper and it will be the only Fourier technique discussed.

For a time series x(t) sampled at N equally spaced points a time interval Δt apart, the discrete power spectrum P(f) can be computed from the equation

$$P(f_k) = \frac{2\Delta t}{N} \left| \sum_{n=o}^{N-1} x_n \exp(-j2\pi nk/N) \right|^2 \qquad 5.3$$

where k = 0,1,2,..., N-1. If the function x(t) is an analytical function, the power density spectrum can be calculated precisely. However, when there

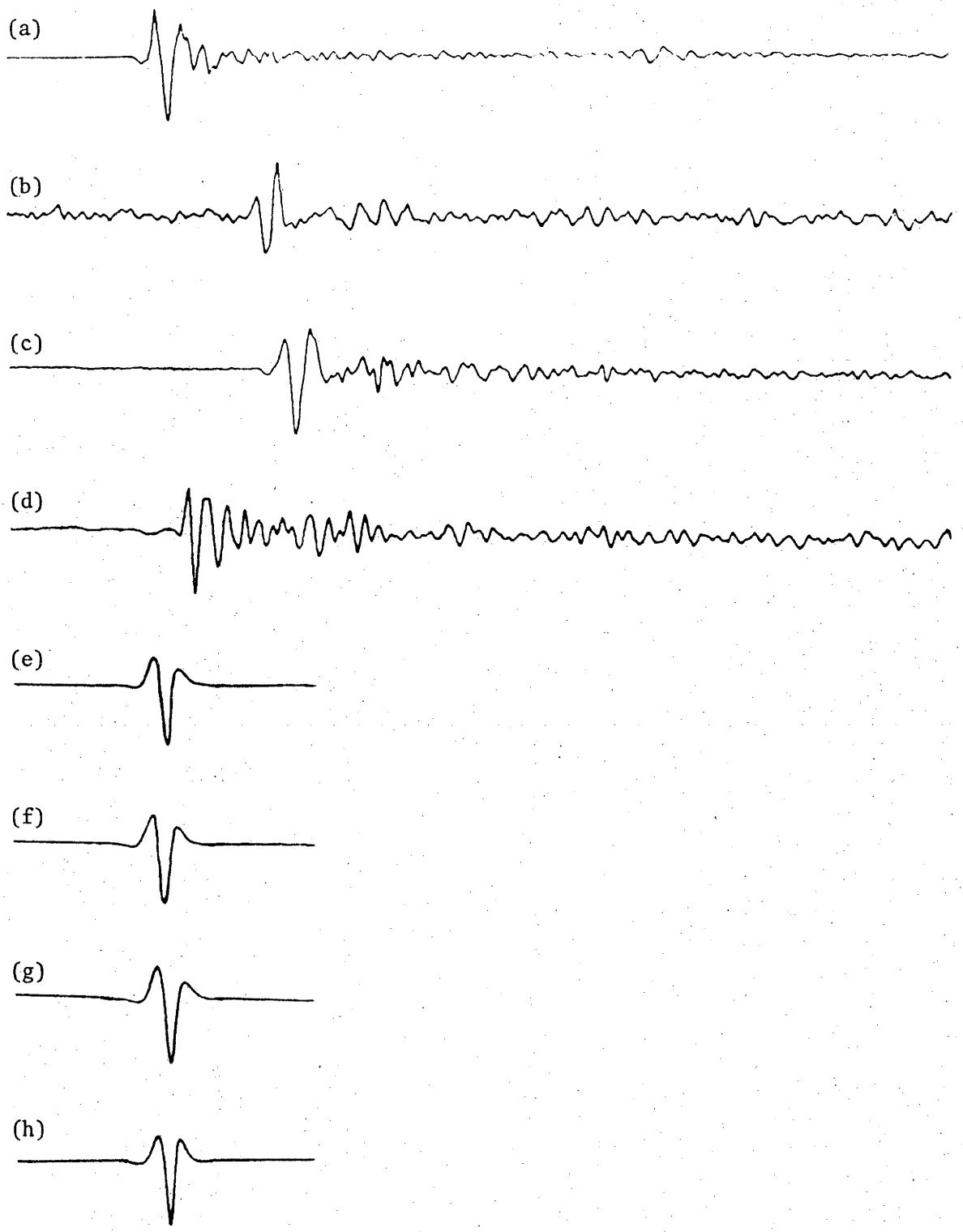

Figure 5.1 Beamformed P phase seismograms given in Table 2.2 for Events: (a) 3, (b) 15, (c) 24, (d) 32. Wavelets e, f, g, and h are non-dispersive synthetic representative of a, b, c, and d respectively. The time scale for all traces is 2 sec/cm.

are noise components involved in the time series, truncation of the time series becomes a problem, reducing the accuracy of the estimate. Using the periodogram method on a real time series, the power at each frequency increment has two degrees of freedom (Bendat and Piersol, 1971). The variance σ_k^2 is given by

$$\sigma_k^2 = P(\omega)^2 \quad . \tag{5.4}$$

One procedure available to reduce this variance is to segment the time series into 1 subsets (Welch, 1967). However, since seismic phases are short transient signals, such segmenting procedures are not possible. The procedure used in this thesis for reducing the variance is beamform stacking of the individual seismic channels. Assuming that the amplitude and phase of the noise contained in each channel are random, the optimal reduction in the variance for M channels is

$$\sigma_k^2 = P(\omega)^2/M \quad . \tag{5.5}$$

The above stacking procedure, before the power estimate is made, will keep the resolution as high as possible while keeping the spectral bandwidth as small as possible when dealing with short transient seismic phases.

Another problem in attempting to estimate the power contained in a transient seismic phase is its length. Generally in the short period range the wavelet is only a few seconds in length. Since the spectral bandwidth will be proportional to the reciprocal time length of the transient signal, the number of independent spectral estimates will be limited. In the case considered here, most of the spectral power contained in such a signal is in the frequency range 0.1 to 3.5 Hz, the number of usable resolved frequency estimates from such a power spectrum are generally less than 6.

This hardly provides enough resolved frequency estimates to determine t* values with any degree of accuracy. The number of resolved frequency estimates can be increased by assuming that before the transient seismic wavelet of interest arrives, and after it passes, there is no signal or noise. With this assumption any number of zeros can be added in front of and behind the transient pulse to extend the length of the time series. Some authors (Bendat and Piersol, 1971; Lines and Ulrych, 1977) feel that this may not be a statistically sound method for determining a power spectrum. Furthermore, these authors feel that undesirable side lobe effects may occur. In the following section the stability and resolution of the Fourier power spectrum will be tested using the padded zeros assumption.

5.4.2 Fourier Periodograms Used

In determining the power spectrum the following procedure will be applied:

(1) The seismic phase of interest is delayed and stacked (the beamforming discussed in Chapter 2).

(2) The first initial wavelet of the seismic phase is set up for analysis.

(3) A 10% cosine taper is applied to the wavelet. This is to reduce the effect of other phases and to avoid individual correction of large numbers at the beginning and end of the data.

(4) A discrete estimate of the power in the wavelet is made at frequency intervals of 0.01 hertz. This is computationally identical to padding on zeros to the time series and using a fast Fourier transform to obtain the power spectrum.

(5) Any frequency component less than the reciprocal of time length of the data was not considered as an adequate measurement of power. In other

words, there must be at least one complete sinusoid in the windowed data before a power estimate can be made.

5.4.3 Examples of the Fourier Periodogram Method

Attempts to estimate the power spectrum of the synthetic time series given in the introduction of this chapter result in an exact fit of its power compared with the theoretical power. This is not surprising since the synthetic time series contains no noise components as well as beginning and ending on a zero mean. For a real transient time series it is very difficult to determine the exact beginning and ending of such a time series because of the existence of interfering seismic phases and noise components. Attempts to truncate the synthetic time series, within reasonable limits, also results in an estimated power spectrum very close to the theoretical spectrum.

Application of the periodogram method to real data gives resulting power spectrums which are quite different from those derived from synthetics. Figure 5.2 through 5.5 are examples of the resulting real power spectra obtained from the data given in Figure 5.1. The only correction made to these power spectra is the removal of the instrumental response. Note the spectral minima which are present in Figures 5.2 to 5.5. In fact, similar minima, at frequency intervals corresponding to the time length of the truncated time series are throughout the power spectrum, though they are not obvious. Maxima also occur at frequency intervals half-way between adjacent minima. This focusing and defocusing of power can be attributed to undersirable side-lobe effects (Bendat and Piersol, 1971; Lines and Ulrych, 1977). Smoothing the power spectrum by averaging can be used to

Figure 5.2 Truncated Fourier Power spectrum of example (a) in Figure 5.1. The points of truncation are shown for this real seismic velocity wavelet in the upper right hand corner of figure. The time scale for the seismic velocity wavelet is 2 sec/cm. Note the large dip in the spectrum at approximately 2.6 Hz caused by the truncation.

Figure 5.3 Same as Figure caption 5.2 except that it is the truncated power spectrum of example (b) in Figure 5.1.

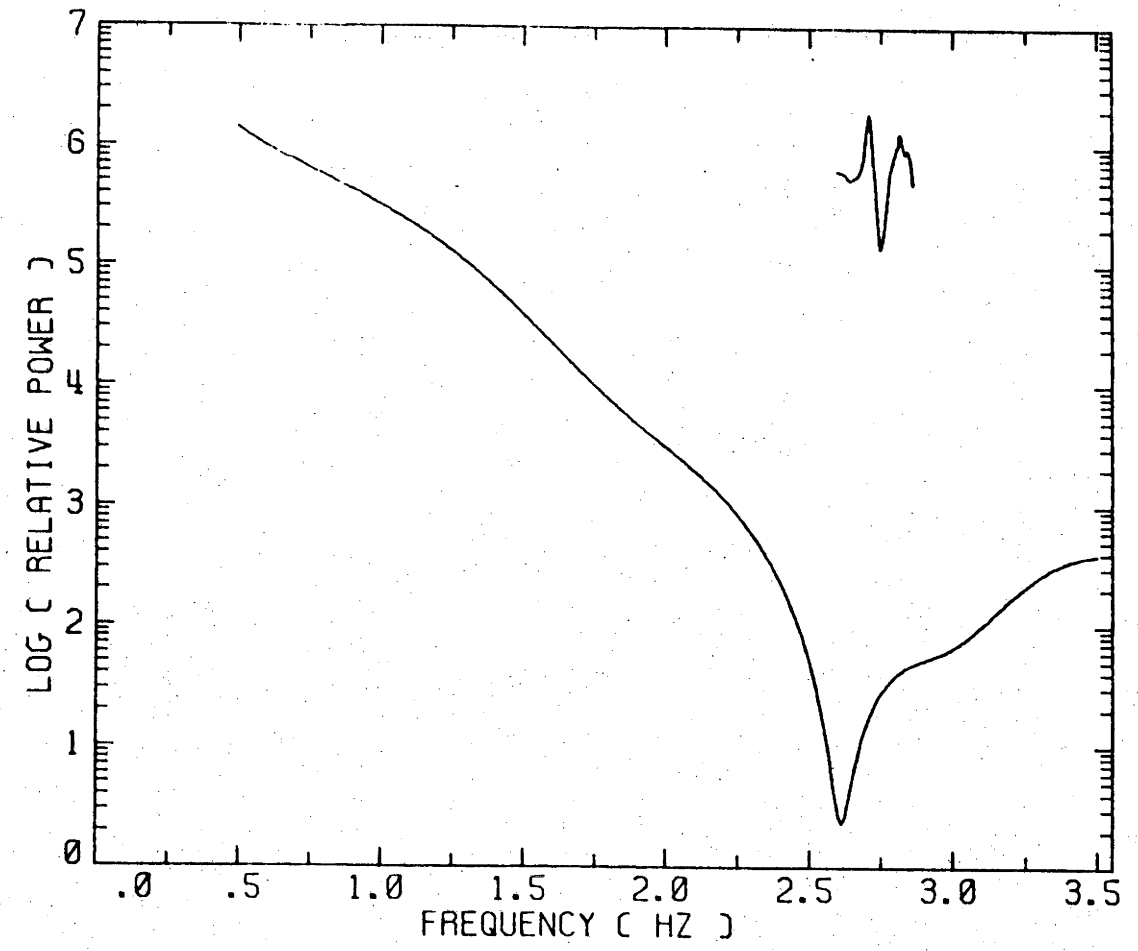
LOG (RELATIVE POWER)
0
1
2
3
4
5
6
7
.0
.5
1.0
1.5
2.0
2.5
3.0
3.5
FREQUENCY (HZ)

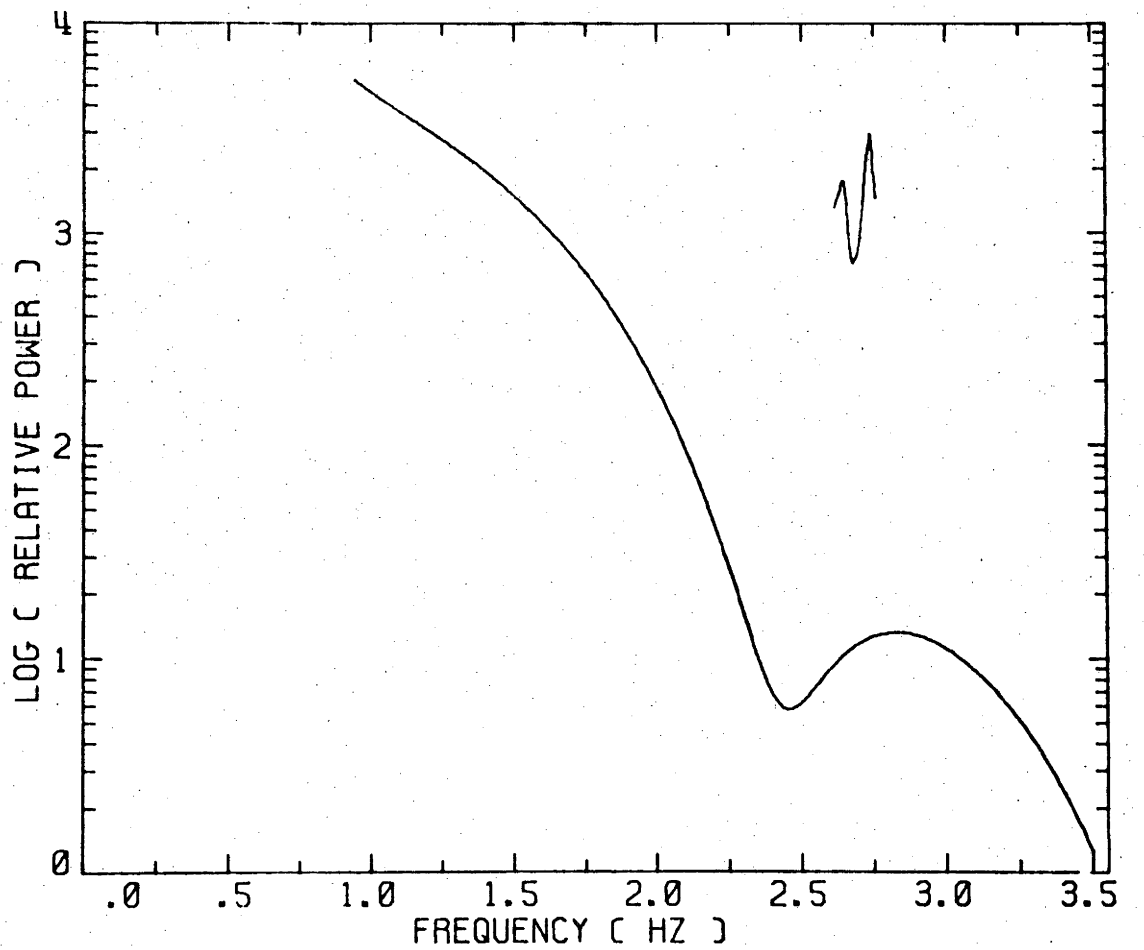
LOG (RELATIVE POWER)
0
1
2
3
4
.0
.5
1.0
1.5
2.0
2.5
3.0
3.5
FREQUENCY (HZ)

Figure 5.4 Same as Figure caption 5.2 except that it is the truncated power spectrum of example (c) in Figure 5.1. Note that the dips due to truncation are not as severe as those in Figures 5.2 and 5.3.

Figure 5.5 Same as Figure caption 5.2 except that it is the truncated power spectrum of example (d) in Figure 5.1. Note the dips due to truncation are not as severe as those in Figures 5.2. and 5.3.

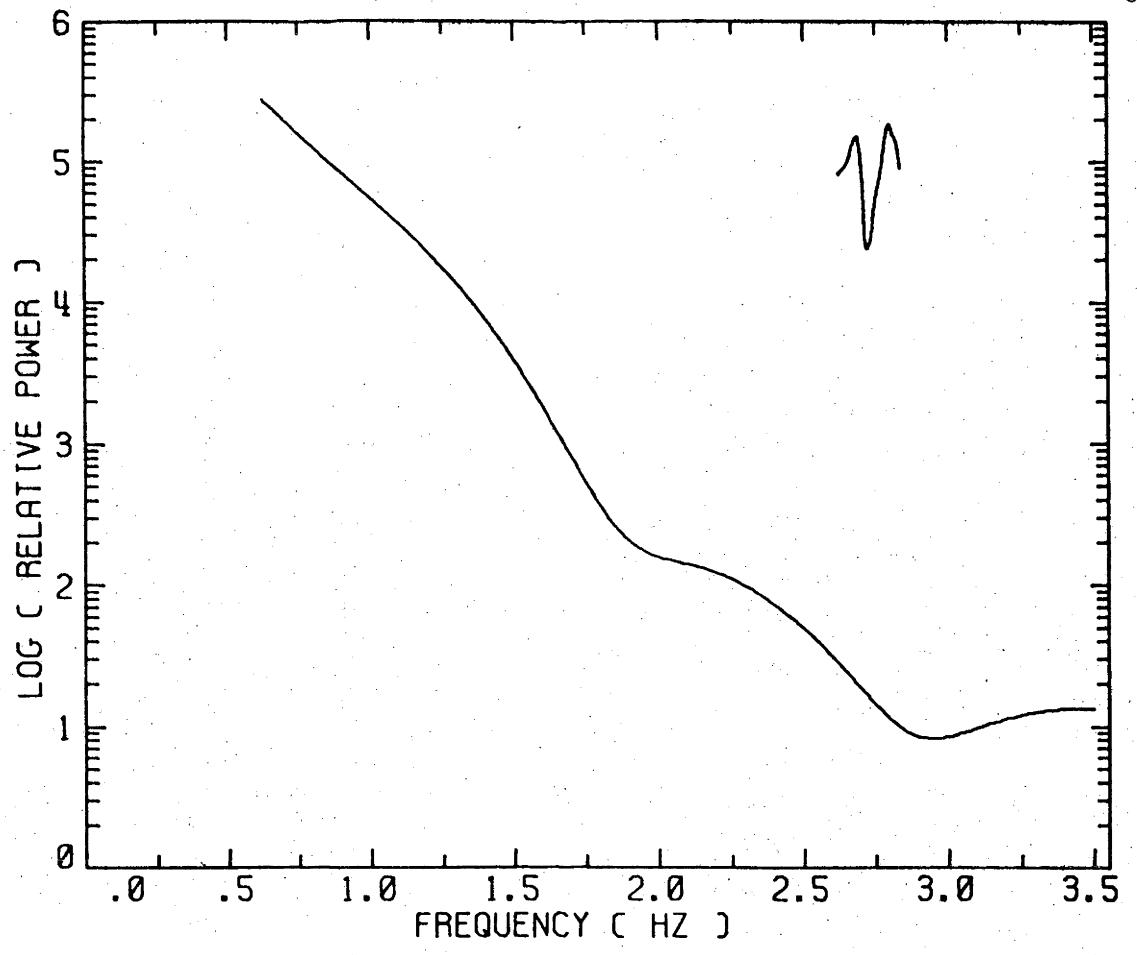
LOG (RELATIVE POWER)
0
1
2
3
4
5
6
.0
.5
1.0
1.5
2.0
2.5
3.0
3.5
FREQUENCY (HZ)

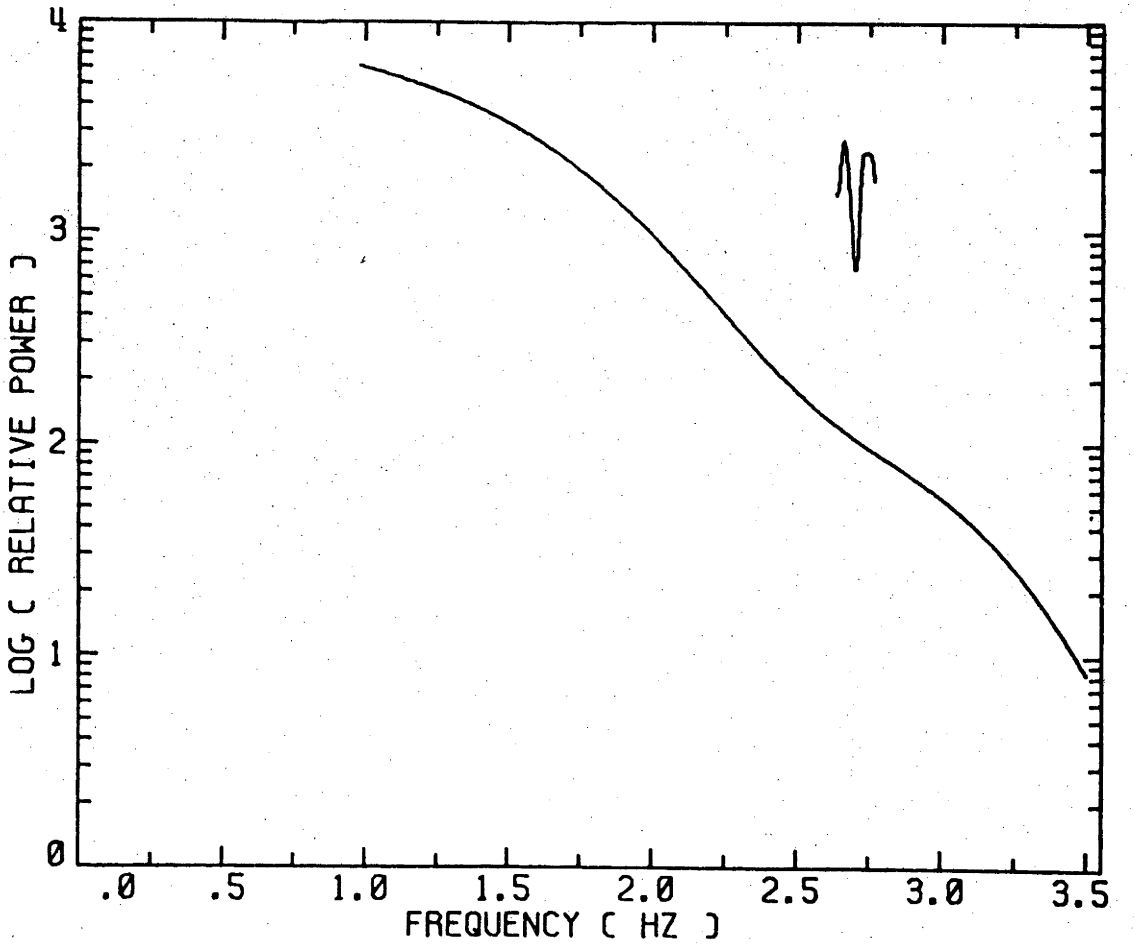
LOG (RELATIVE POWER)
0
1
2
3
4
.0
.5
1.0
1.5
2.0
2.5
3.0
3.5
FREQUENCY (HZ)

compensate for side lobe effects; loss of resolution and biasing of the power processing of transient seismic data will be explored next, in an attempt (i) to remove side lobe effects; (ii) to increase spectral resolution; and (iii) to reduce biasing effects.

5.5 Parameter Fitting Spectral Estimates

5.5.1 Theory

Parameter fitting spectral methods for estimating power in a time series have become popular because of their ability to determine estimates of power from a short time series. The inability to determine the exact autocorrelation function for short time series may lead to problems in stability and resolution using Fourier techniques.

The parameter fitting spectral technique is built around the idea that if white noise is passed through a particular impulse response filter the resulting time series x(t) will have a power spectrum which is identical to power spectrum of the observed signal. The autoregressive process which satisfies this time series filter is

$$x(t) = -\alpha(1)x(t-1)-\alpha(2)x(t-2) - \ldots -\alpha(L)x(t-L) + u(t) \qquad 5.6$$

where $\alpha(k)$ are the coefficients which are defined by the impulse response of the process, out to L known lags. If the process is reversed starting with x(t) (the time series which is observed), the impulse response necessary to form a white noise series with the same length L can be developed. The output of such an impulse response filter is then

$$u(t) = x(t) + a(1)x(t-1) + \ldots + a(L)x(t-L) \qquad 5.7$$

where a(k) are the coefficients of the white noise filter. By minimizing

the mean square value of the filter output the values of a(1) ..., a(k) are selected and must satisfy the equation

$$[1,a(1), \ldots, a(L)] \begin{bmatrix} R(0) & \ldots & R(L) \\ \vdots & \ddots & \vdots \\ R(L) & \ldots & R(0) \end{bmatrix} = [P,0, \ldots] \qquad 5.8$$

where the right hand side of the above equation is the estimated prediction error and R(0), ..., R(L) are the known autocorrelations, which is a Töeplitz matrix of the autocorrelation series. The series 1, a(1), ..., a(L) is then a hindsight prediction error filter. It predicts what the future values of the time series are going to be, based upon past values. Also it follows that if the time series under study is really generated from a white noise process, the a(k)'s in Equation 5.7 are equal to the values $\alpha(k)$'s in Equation 5.6.

Equation 5.8 is generally known as the normal equation (accredited to Yule, 1927 and Walker, 1931) and is called the prediction error filter. If 1, a(1), ..., a(L) are known, the unknown autocorrelations can be extended by prediction. The power in the time series can then be calculated, based upon the known and predicted values of the autocorrelations, by performing a Fourier transform. However, it is much easier to determine the power in the time series by obtaining the frequency response function of the prediction error filter. That is, if the output of the filter is white with power spectral density P, and the time series is sampled at Δt seconds, the power P(f) of the time series becomes

$$P(f) = \frac{P}{\left| \sum_{j=o}^{L} a(j) e^{-i2\pi jf\Delta t} \right|^2} \quad . \qquad 5.9$$

One of the main difficulties in determining a power spectrum in this way has been in deciding what to use as the discrete autocorrelation function. Given a time series x(1) ..., x(t), the conventional formulas for obtaining an estimate of autocorrelation function are

$$R(j) = \frac{1}{T+1} \sum_{k=o}^{N} x(k)x(k+j) \qquad 5.10$$

and

$$R(j) = \frac{1}{T+1-|j|} \sum_{k=o}^{N} x(k)x(k+j) \quad . \qquad 5.11$$

In order to estimate the power, which must be positive for all values, the autocorrelation matrix (Töeplitz matrix) given in Equation 5.8 must be positively defined. For this reason Equation 5.10 is used to determine the autocorrelation coefficients for the Yule-Walker approach. However, the first autocorrelation formula does give a positively defined Töeplitz matrix but assumes that the time series is extended with zeros, thereby biasing the estimate. The second autocorrelation formula above (Equation 5.11) is an unbiased estimate of autocorrelation but can result in a non-positively defined Töeplitz matrix.

Burg (1967) has provided a method for determining another estimate of the autocorrelation. The following paragraphs will demonstrate the method in which the error prediction coefficients can be determined.

Since there is no significant statistical difference between forward and backward time for a time series which is an interval from a stationary random process specified by x(t), the forward prediction error $e_+(t)$ in terms of its forward prediction coefficient a(k) can be written as

$$e_+(t) = x(t) + a(1)x(t-1) + \ldots + a(L)x(t-L) \qquad 5.12$$

and its backward prediction errors series

$$e_-(t) = x(t-L) + a^*(1)x(t-L) + \ldots + a^*(L)x(t) \qquad 5.13$$

where $a^*(k)$ are the complex conjugates of $a(k)$. The cost function is then defined as

$$J = \sum_{t=L}^{N} \{|e_+(t)|^2 + |e_-(t)|^2\} \quad . \qquad 5.14$$

The above equation equally weights e_+ and e_- to find the $a(k)$, $k = 1, \ldots, L$ which minimize J. After the $a(k)$'s have been determined the spectral power can be estimated through the use of Equation 5.9. Although the above approach is a valid one, it does not guarantee that the autocorrelation matrix given in Equation 5.8 is non-negatively defined. Therefore Burg proposed to predict ahead one prediction error point from the previously known ones. In other words, given the error series e_+ and e_- as defined above for the forward error filter $[1, a(1), \ldots, a(L)]$ and the backward error filter $[a^*(1), \ldots a^*(L)]$ respectively, a new error series ε_+ and ε_- can be developed by predicting ahead one point, which gives rise to the new forward prediction error filters $[1, a'(1), \ldots, a'(L+1)]$. The one point ahead prediction error filters can be calculated by Levinson's recursion algorithm (Levinson, 1947) giving

$$\varepsilon_+(t) = e_+(t) + ce_-(t) \qquad 5.15$$

and

$$\varepsilon_-(t) = e_-(t) + c^*e_+(t) \qquad 5.16$$

where c and its complex conjugate c* are constants. Again making use of the cost function, the constants c and c* can be selected such that

$$J = \sum_{t=L+1}^{T} \{|\varepsilon_+(t)|^2 + |\varepsilon_-(t)|^2\} \qquad 5.17$$

is minimized. Such minimization guarantees that the constants c and c* are less than one. Further, the calculation of the one-ahead prediction error filter guarantees the Töeplitz matrix in Equation 5.8 to be positively defined. After the series [1,a'(1), ..., a'(L+1)] has been determined the spectral power can be calculated using Equation 5.9. For clarity a pseudo-flow chart of Burg's recursion is shown in Figure 5.6.

The only requirement left is the determination of the number of prediction error filters necessary to describe the time series completely. Too few filter coefficients will make the power spectrum appear smeared out, but on the other hand too many filter coefficients may cause the power spectral estimate to have sporadic spikes in the final spectrum. The method for determining the proper number of filter coefficients used in this thesis for the Yule-Walker and the Maximum Entropy power estimates is the Final Prediction Error (FPE) criterion (Akaike, 1969a,b).

The basic idea behind FPE is as follows. It would be expected that as the number of filter coefficients increased the residual estimate prediction error would decrease. However, when the filter coefficients are applied to a new sample of the autoregressive process, they will be out of tune with this new sample. Therefore the mean square error will increase. FPE takes these two factors into account and calculates the average mean square error. These two factors can be combined into a simple mathematical expression for N data points and the prediction distance L. Hence

Figure 5.6

Details of Burg Recursion
(After Lacoss, 1977)

Initialize:

$$p = \frac{1}{T+1} \sum_{t=0}^{T} |x_t|^2$$

$$L = 0$$

Define:

$$c_{++} = \sum_{t=L+1}^{T} |e_+(t)|^2$$

$$c_{--} = \sum_{t=L+1}^{T} |e_-(t-1)|^2$$

$$c_{+-} = \sum_{t=L+1}^{T} e_+(t) e_-^*(t-1)$$

Then:

$$c = \frac{-2c_{+-}}{(c_{++}) + (c_{--})}$$

$$p \rightarrow (1-|c|^2)p$$

$$\begin{bmatrix} 1 \\ a_1 \\ \cdot \\ \cdot \\ \cdot \\ a_L \\ a_{L+1} \end{bmatrix} \rightarrow \begin{bmatrix} 1 \\ a_1 \\ \cdot \\ \cdot \\ \cdot \\ a_L \\ 0 \end{bmatrix} + c \begin{bmatrix} 0 \\ a_L \\ \cdot \\ \cdot \\ \cdot \\ a_L \\ 1 \end{bmatrix}$$

$$L \rightarrow L+1$$

$$e_+(t) \rightarrow e_+(t) + ce_-(t-1)$$

$$e_-(t) \rightarrow e_-(t-1) + c^* e_+(t)$$

$$FPE = \frac{N + (M+1)}{N - (M+1)} P \qquad 5.18$$

where P is the estimated prediction error given on the right-hand side of Equation 5.18. If, however, the mean is removed from the time series under consideration, the above equation becomes simply

$$FPE = \frac{N + M}{N - M} P \quad . \qquad 5.19$$

The theory above is a brief outline of the ingredients needed to get an estimate of the spectral power of a time series by parameter fitting techniques. The following sections will discuss what happens when these spectral techniques are applied to both synthetic and real data.

5.5.2 Examples of the Parameter Fitting Technique

Using the synthetic wavelets developed in Section 5.3 of this chapter, the power spectra derived from the parameter fitting method are compared with the exact Fourier power spectra of these synthetic wavelets. Figures 5.7 through 5.10 and Figures 5.11 through 5.14 are examples of the parameter fitting method using the Yule-Walker approach and the maximum entropy approach respectively. In the following paragraphs, the resolution and stability will be examined in order to determine if these technqiues can be considered appropriate for analyses of this type of wavelet.

According to Akaike's (FPE) criterion only 8 or 9 prediction error coefficients are necessary to describe fully a wavelet's time series as shown in the upper right-hand corner of the figure. However, applying the prediction error coefficients to Equation 5.9 to obtain the power spectra

Figure 5.7 A comparison of the exact Fourier power spectrum (solid line) of the non-dispersive synthetic wavelet given in Figure 5.1e with the Yule-Walker spectral method (dashed line).

Figure 5.8 Same as for Figure 5.7 except that the example is for the spectrum of the wavelet given in Figure 5.1f.

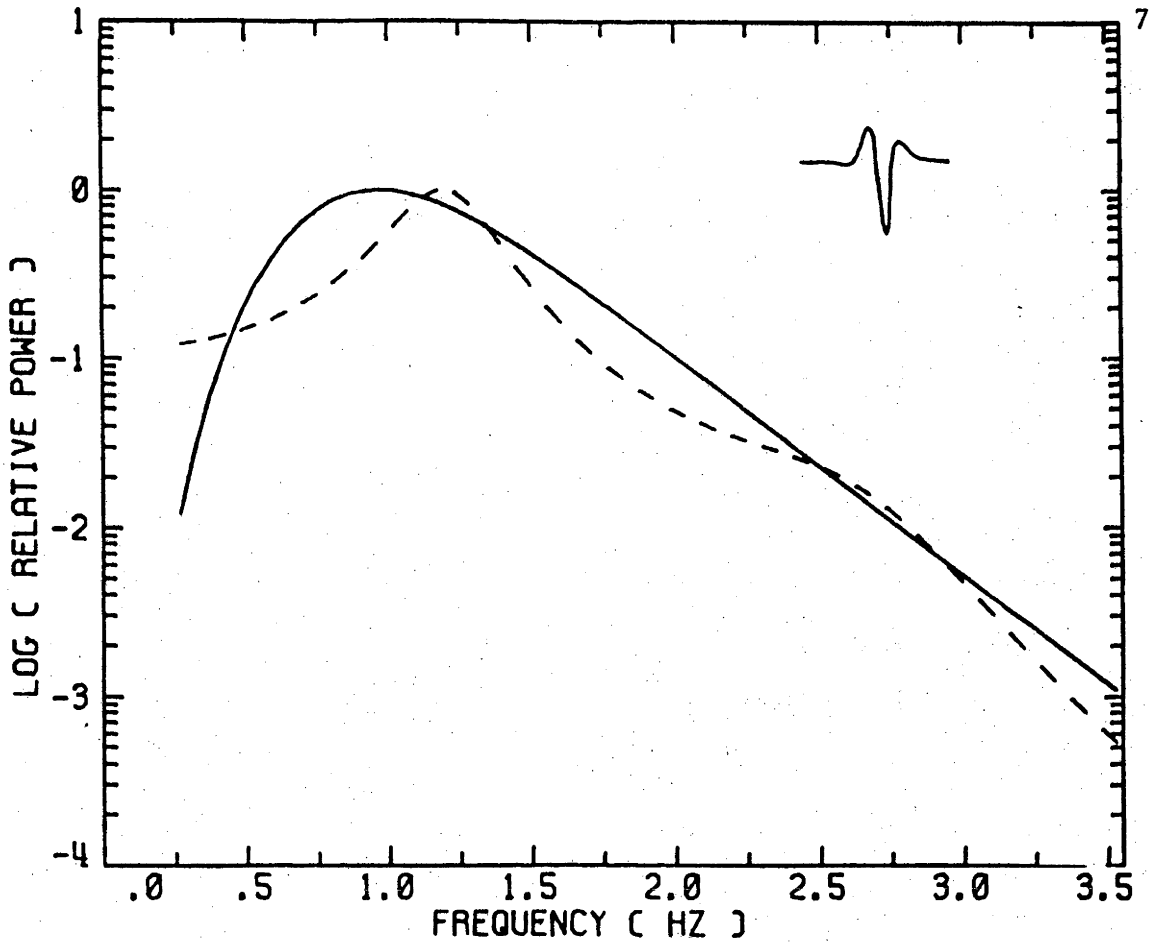
LOG (RELATIVE POWER)
1
0
-1
-2
-3
-4
.0
.5
1.0
1.5
2.0
2.5
3.0
3.5
FREQUENCY (HZ)

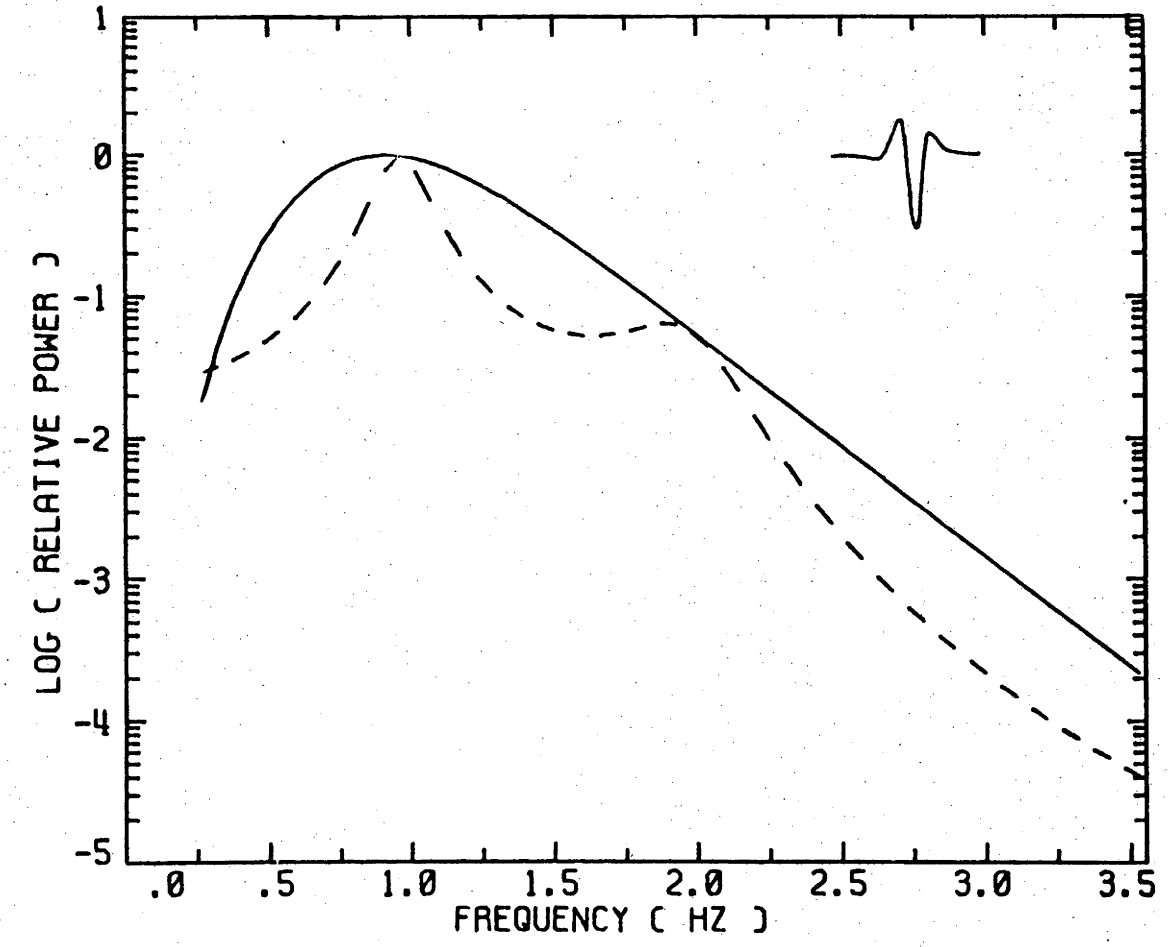
LOG (RELATIVE POWER)
1
0
-1
-2
-3
-4
-5
.0
.5
1.0
1.5
2.0
2.5
3.0
3.5
FREQUENCY (HZ)

Figure 5.9 Same as for Figure 5.7 except that the example is for the spectrum of the wavelet given in Figure 5.1g.

Figure 5.10 Same as for Figure 5.7 except that the example is for the spectrum of the wavelet given in Figure 5.1h.

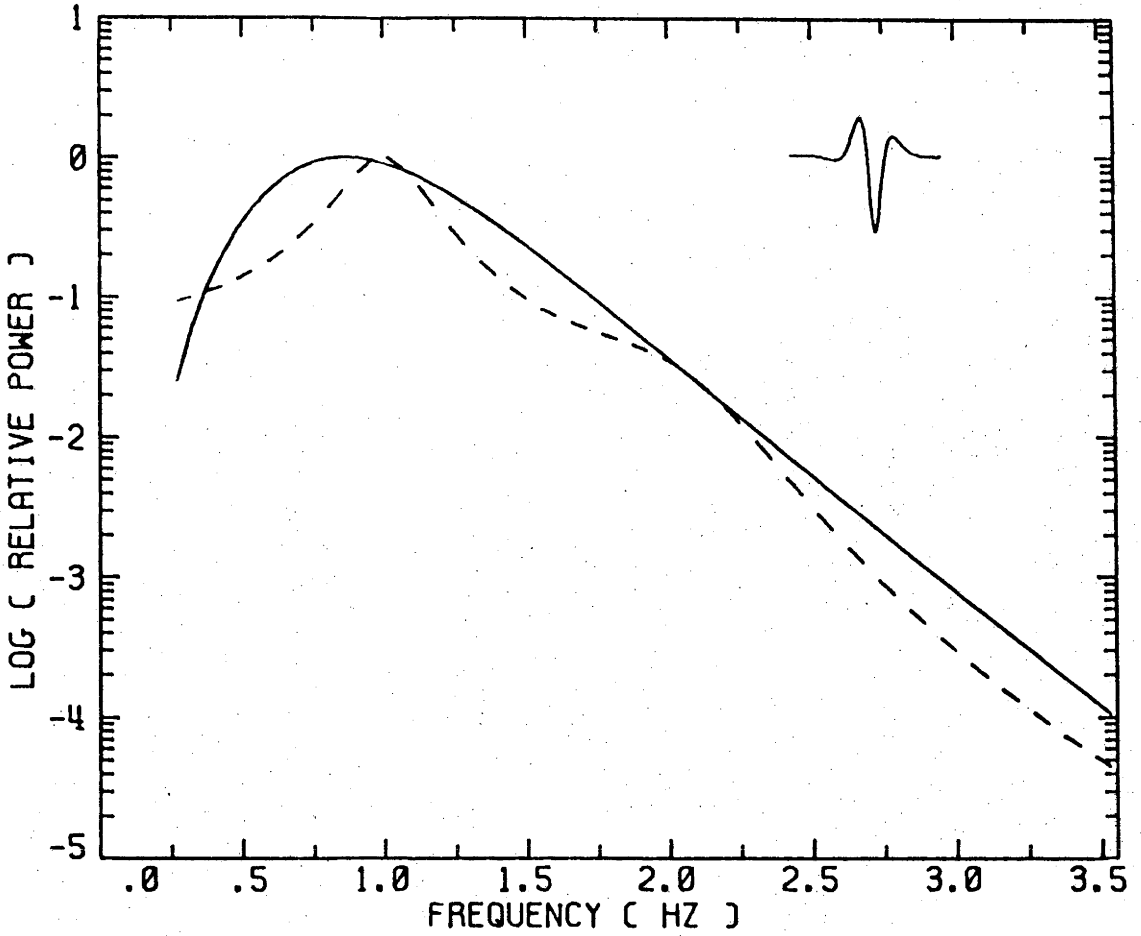
LOG (RELATIVE POWER)
1
0
-1
-2
-3
-4
-5
.0
.5
1.0
1.5
2.0
2.5
3.0
3.5
FREQUENCY (HZ)

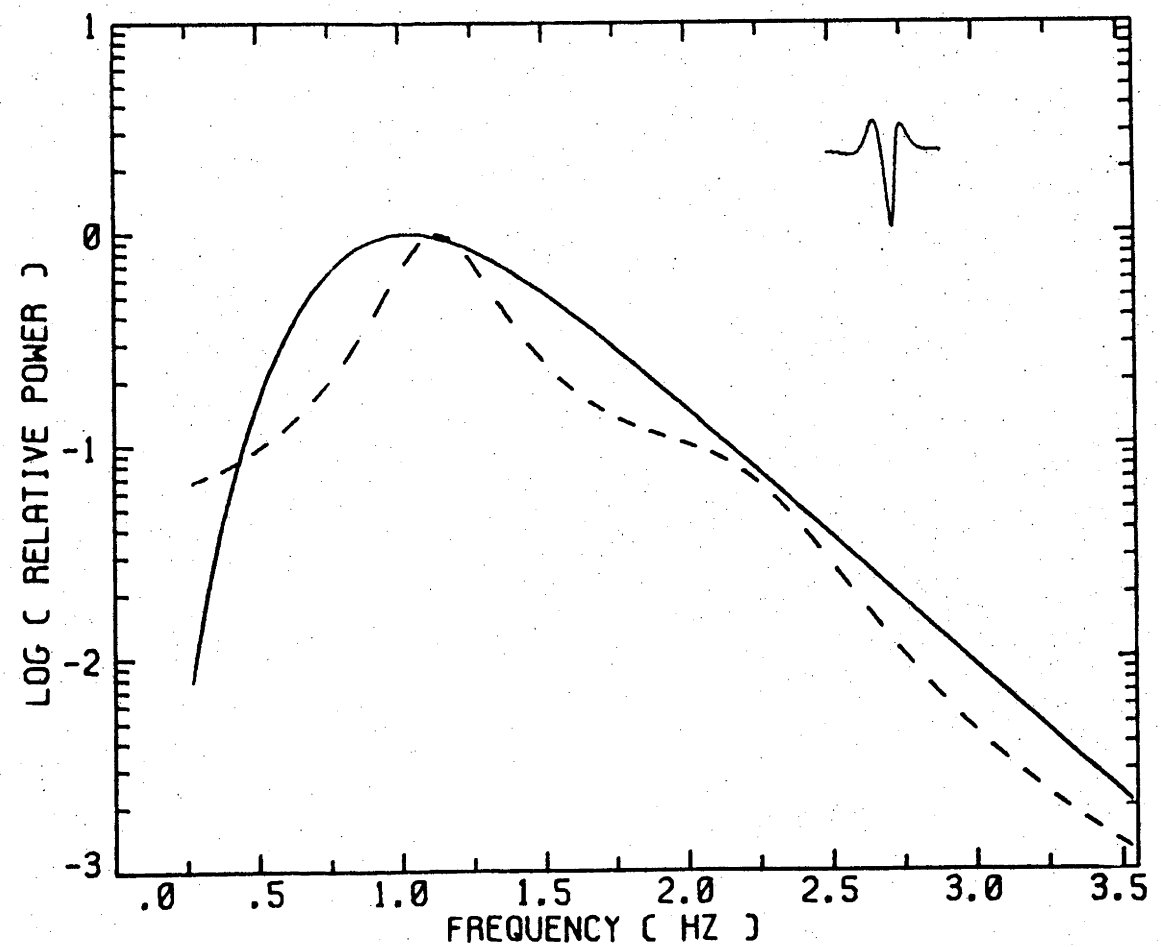
LOG (RELATIVE POWER)
1
0
-1
-2
-3
.0
.5
1.0
1.5
2.0
2.5
3.0
3.5
FREQUENCY (HZ)

Figure 5.11 A comparison of the exact Fourier power spectrum (solid line) of the non-dispersive synthetic wavelet given in Figure 5.1e with Burg's Maximum Entropy spectral method (dashed line).

Figure 5.12 Same as for Figure 5.11 except that the example is for the spectrum of the wavelet given in Figure 5.1f.

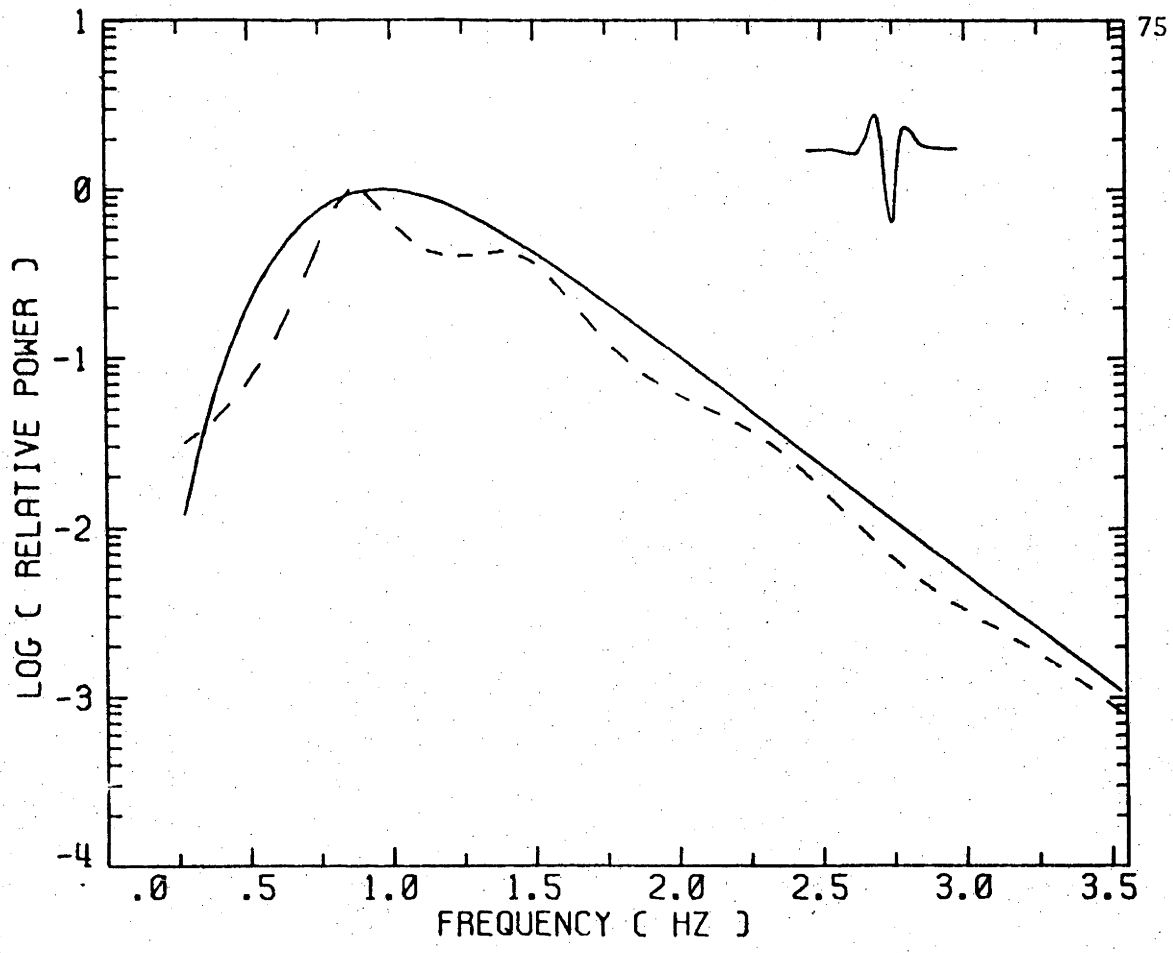
1
0
-1
-2
-3
-4
LOG (RELATIVE POWER)
.0
.5
1.0
1.5
2.0
2.5
3.0
3.5
FREQUENCY (HZ)

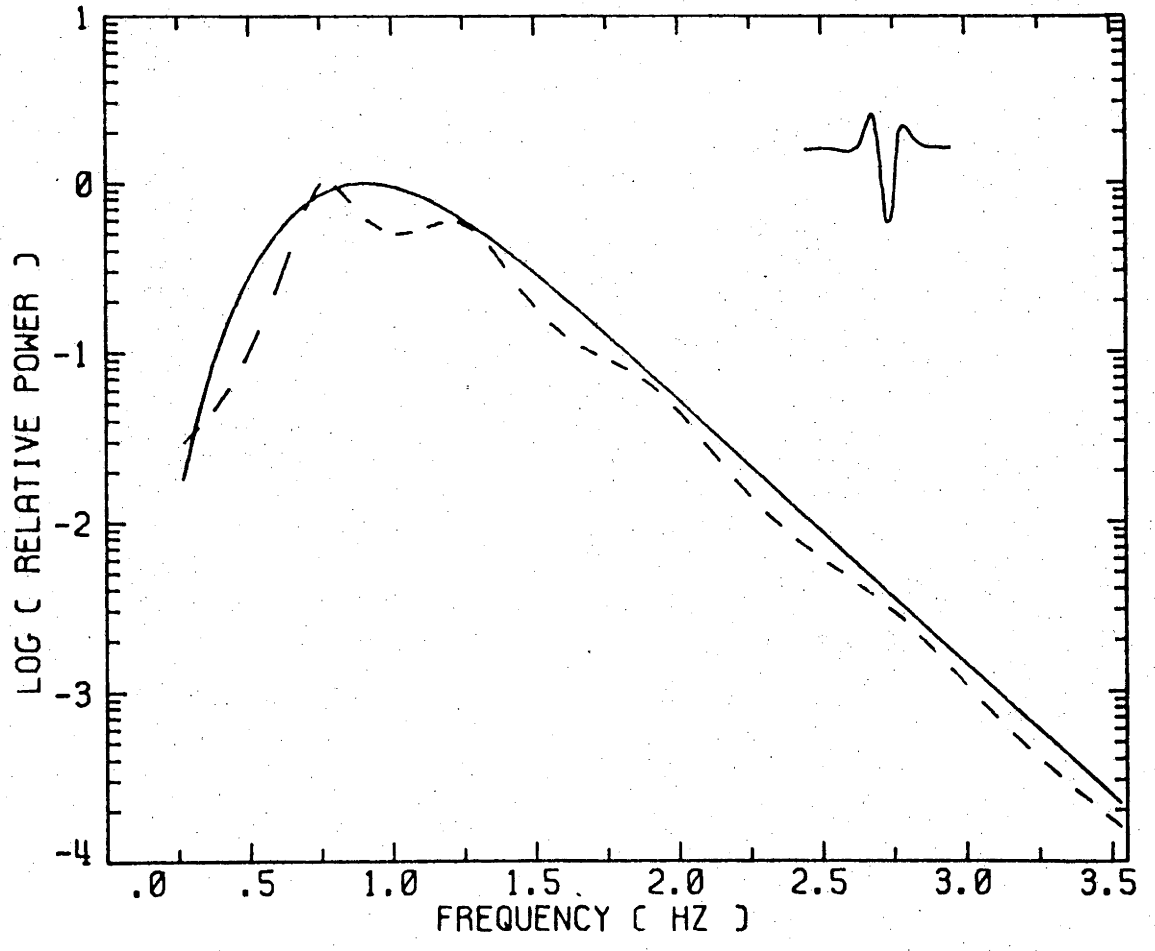
1
0
-1
-2
-3
-4
LOG (RELATIVE POWER)
.0
.5
1.0
1.5
2.0
2.5
3.0
3.5
FREQUENCY (HZ)

Figure 5.13 Same as for Figure 5.11 except that the example is for the spectrum of the wavelet given in Figure 5.1g.

Figure 5.14 Same as for Figure 5.11 except that the example is for the spectrum of the wavelet given in Figure 5.1h.

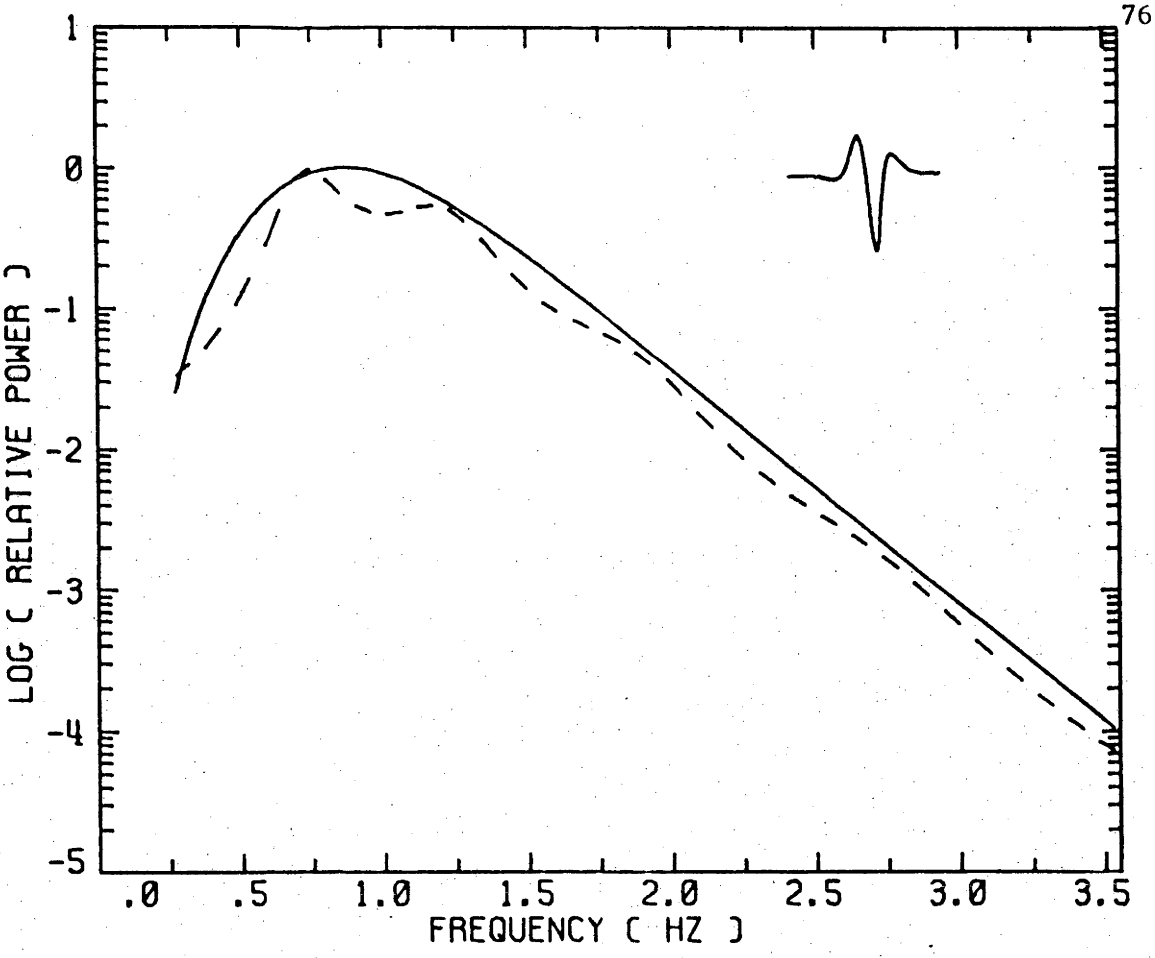
1
0
-1
-2
-3
-4
-5
LOG (RELATIVE POWER)
.0
.5
1.0
1.5
2.0
2.5
3.0
3.5
FREQUENCY (HZ)

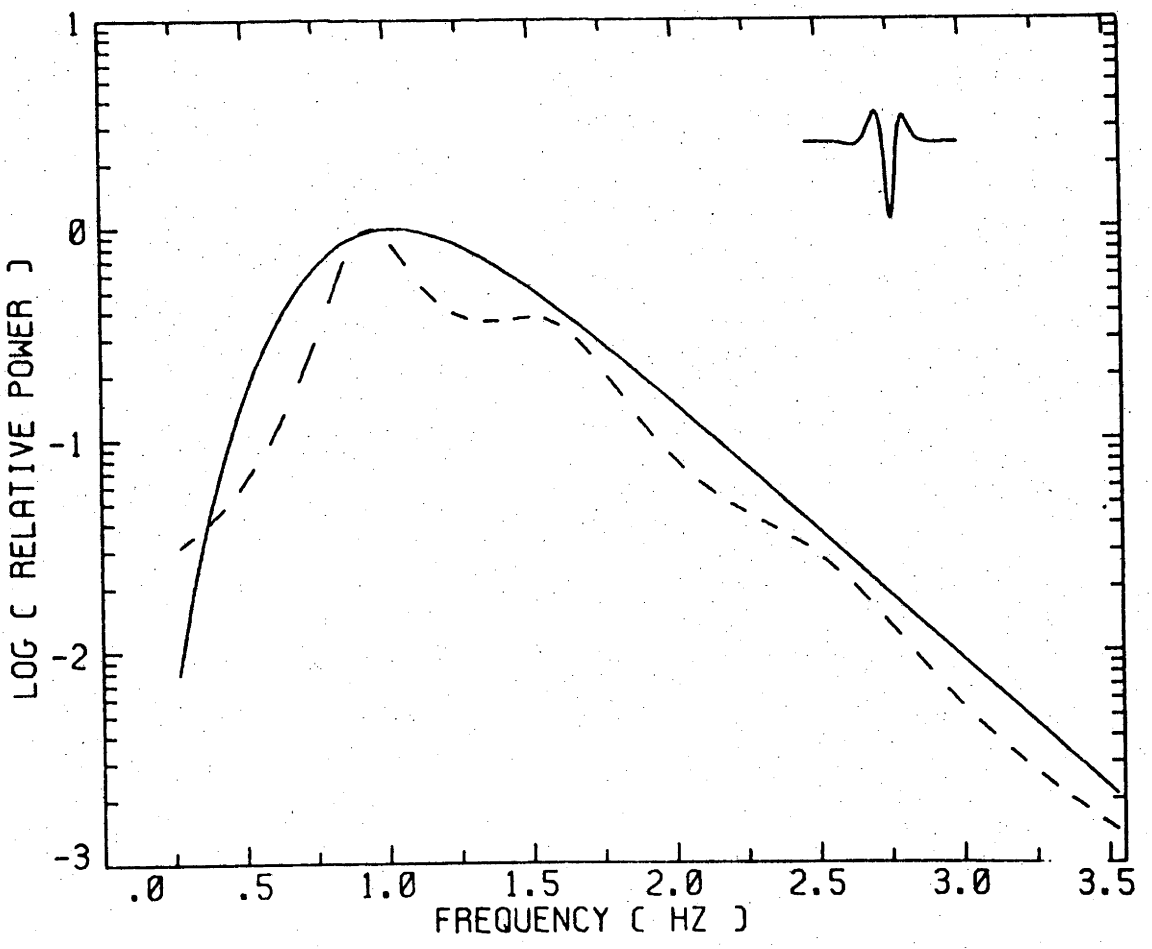
1
0
-1
-2
-3
LOG (RELATIVE POWER)
.0
.5
1.0
1.5
2.0
2.5
3.0
3.5
FREQUENCY (HZ)

for these wavelets, the most striking features are the predominant peaks which occur in these spectra. These peaks in no way follow the spectra determined analytically. As can be seen, these peaks are concave inward from the maximum spectral value rather than outward as indicated by the actual spectrum. This inward concaving of the Yule-Walker spectral peaks make the determination of t* values using frequencies lower than the peak useless. In order to obtain reliable values for t* and reduce the standard error, as much as possible of the total dynamic range of the frequency spectrum must be used. Another important consideration is the location of the (Y-W) spectral peak. As indicated by the figures, these peaks are displaced toward the higher frequency range. This occurrence will cause difficulties in location of the source function's corner frequency. Burg's maximum entropy method (MEM) has some of the same difficulties as the Yule-Walker method: again the spectral power is concave inward towards the (MEM) spectral peak and the low frequency power is poorly determined. However the peak power of the maximum entropy method coincides more closely to the correct spectral peak. Furthermore, the power fit for the frequency at the right of the peak value is better than that given by the Yule-Walker method eventhough these spectra have a more oscillatory character. The reason for this is that over twice the number of prediction error coefficients are required to define the time series wavelets using Burg's method than for the Yule-Walker method. Lastly, the MEM gives a better spectral fit to the correct spectra when the predominant frequency tends towards the low-frequency end of the spectrum. As a result, the best MEM spectra would occur when the predominant frequency is zero, which is generally not the case.

Eventhough the above parameter-fitting technique has the advantage of

not subjectively picking windowing functions and lag lengths as in the case of Fourier techniques, they do not appear to give spectra with enough stability to determine the attenuation properties of seismic phase wavelets. Basically the reason is that seismic phase wavelets are not autoregressive time series. Seismic wavelets are either moving average (MA) or autoregressive moving average (ARMA) time sequences. Attempts to parameterize a seismic phase wavelet in terms of an autoregressive series is therefore invalid. On the other hand, modelling a time sequence by a moving average process or moving average autoregressive process is difficult (Jenkins and Watts, 1968; Chatfield, 1975) because efficient explicit estimators cannot be found.

Based upon the above conclusion, that seismic wavelets are not autoregressive in nature, examples of real seismic time series analysed by these methods will not be included because of their improper fit to synthetic data. Seismic wavelets in a noise environment would only result in a power spectrum improperly parameterized.

5.6 Conclusions about Time Domain, Fourier, and Autoregressive Spectral Methods

As pointed out previously the time domain method of determining the corner frequency of the source spectrum and the attenuation factor t* is considered to be an inadequate approach because it is basically a trial and error method. Such a method may lead to wrong values for both the corner frequency and attenuation factor t* but still, in the presence of noise, give the appearance of being a good fit to real data. Even in the case where a constructed synthetic wavelet is compared with real data and the fit is poor, one could argue that the real data is perturbed by noise. Such

an argument would therefore call upon the "insight" of the observer to subjectively "eyeball" his estimate of the time wavelet in noise. An "eyeball" estimator cannot be considered to be an analytical estimator because it calls upon the built-in prejudices of the observer and not on hard data.

A second objection to fitting synthetics to real data is the lack of knowledge about the phase component of the attenuation factor t*. One could use a variety of theoretical phase components for the attenuation factor (Futterman, 1962; Strick, 1967) but the actual phase relationship of attenuation for the short period seismic waves remains unobserved. Therefore the only remaining approach would be to "guess at" the phase relationship of attenuation, which may lead to incorrect synthetics for matching with real data. Such a matching of real data with synthetic data may appear to be correct but could also be substantially wrong.

A third objection to time domain fitting can be raised. The shape of the wavelet being estimated will be dominated by the predominant frequency. The high frequency roll-off will have little influence on the shape of a derived synthetic wavelet, especially over a limited band of frequencies. This frequency roll-off is precisely the information needed to determine the quality factor Q.

The examples given in this chapter demonstrate that power spectral estimates are not without their drawbacks. Dealing with real data, it was found that side lobe effects perturb the resulting Fourier power spectrum, making it difficult to determine where the spectral information is at the white noise level. Tapering data before the spectrum is determined does not appear to eliminate this side lobe effect. Spectral smoothing leads

to a very biased spectrum. t*'s determined by a smoothed spectrum will therefore be biased. All-pole filter technqiues of Yule-Walker and Burg tend to peak the spectrum to the point where it becomes useless for determining the attenuation factor with any degree of success. Methods which describe power spectra more accurately than the above methods will be discussed in the following chapter.

CHAPTER 6

SPECTRAL ANALYSIS (SUCCESSFUL METHODS)

6.1 Introduction

As shown in the last chapter, when the time series is short, poor estimates of spectral power are obtained if Fourier and parameter fitting techniques are used, the chief reason being the convolution of the sinc function into the spectra in the case of Fourier analysis and the inability to model the time series as an autoregressive sequence in the case of parameter-fitting techniques. To overcome these difficulties, two more spectral techniques have been tested to determine if they are appropriate for estimating t* values. Specifically the spectral techniques considered were (i) the Maximum Likelihood Method (Capon, 1973; Lacoss, 1971); and (ii) the Homomorphic Deconvolution Technique (Oppenheim et al., 1968; Oppenheim and Schafer, 1975). The remainder of this chapter will be devoted to the theoretical and practical application of these techniques to transient short period seismic wavelets.

6.2 Maximum Likelihood Method (MLM)

6.2.1 Theory

The Maximum Likelihood Method (MLM) was developed by Capon et al., (1967) to estimate the spectral amplitudes of a seismic event for a given frequency based upon the noise statistics. This method looks at the noise prior to the first arrival and designs a window in an optimal way (in frequency-wavenumber space) to minimize the noise while passing the signal

without distortion. Later, Lacoss (1971) showed how this technique could be extended to the frequency domain and return a power spectrum for single channel data. A good mathematical description of this method is given by Kanasewich (1973) and will be highlighted here.

Suppose one wishes to design a filter having an impulse response W, with an input y, to return an output x. If the input consists of complex sinusoids of amplitude A with a zero mean noise term ε produced by a random process, the input signal y can be written as

$$y_k = Ae^{+i2\pi f\Delta tk} + \varepsilon_k \qquad 6.1$$

where Δt is the sampling interval and k is the time index. The convolution of the filter with the input signal would therefore yield the output signal x, where

$$x_k = \sum_{n=1}^{N} W_n y_{k+1-n} \quad . \qquad 6.2$$

For a sinusoid to be passed through the filter without distortion or delay, the following condition must exist

$$Ae^{i2\pi fk\Delta t} = \sum_{n=1}^{N} AW_n e^{i2\pi f\Delta t(k+1-n)} \qquad 6.3$$

or simply

$$1 = \sum_{n=1}^{N} W_n e^{i2\pi f\Delta t(1-n)} \quad . \qquad 6.4$$

This equation can be easily written in matrix form

$$1 = [E^{*T}][W] \qquad 6.5$$

where

$$[W] = \text{col}[W_1, W, \ldots, W_N] \qquad 6.6$$

and

$$[E] = \text{col}[1, e^{i2\pi f\Delta t}, \ldots, e^{i2\pi f\Delta t(n-1)}] \quad . \tag{6.7}$$

The filter should also pass the complex conjugate of the signal without distortion so that

$$1 = [E^T][W] \quad . \tag{6.8}$$

In order to optimize the determination of the power in the signal, the variance of the zero mean noise must be minimized.

The variance of the output can be expressed as simply the expectation, E, of the squared output.

$$\sigma^2 = E(x_k)^2 \quad . \tag{6.9}$$

In matrix form the above equation becomes (Kanasewich, 1973)

$$\sigma^2 = [W^{*T}][A][W] \tag{6.10}$$

where $[W^{*T}]$ is the complex conjugate matrix of the filter and A is an NxN Töeplitz correlation matrix formed from the autocorrelation coefficients.

To minimize the variance with the conditions given by Equations 6.4 and 6.8, Capon related these two equations in terms of an undetermined multiplier, λ, and minimized them with respect to the unknown filter coefficients, W_n.

$$\frac{\partial}{\partial[W_n]} \{[W^{*T}][A][W] - \lambda([E^{*T}][W - 1)]\} = 0 \tag{6.11}$$

This yields a set of equations which, when expressed in matrix notation, becomes

$$[A][W] = \frac{\lambda}{2}[E^*] \quad . \tag{6.12}$$

By multiplying both sides of the equation by the inverse of [A] and substituting [W] using Equation 6.8, the above equation becomes

$$\frac{1}{[E^T]} = \frac{\lambda}{2}[A^{-1}][E^*] \tag{6.13}$$

or

$$\frac{\lambda}{2} = \frac{1}{[E^T][A^{-1}][E^*]} \quad . \tag{6.14}$$

Making use of Equation 6.12 the above equation can be written in terms of the filter matrix [W]

$$[W] = \frac{[A^{-1}][E^*]}{[E^T][A^{-1}][E^*]} \quad . \tag{6.15}$$

Since the vector [W] is now known, it is a simple matter to write the transposed complex conjugate of the vector and solve for the output variance in terms of $[A^{-1}]$, $[E^T]$ and $[E^*]$ using Equation 6.10. After some mathematical manipulation the variance of the output becomes

$$\sigma^2 = \frac{1}{E^T A^{-1} E^*} = P_L \tag{6.16}$$

P_L is the maximum likelihood spectral power estimator given by Lacoss (1971).

Generally, the maximum likelihood method (MLM) is used on stationary random time series because such a series can be segmented to obtain the power of each individual segment (Welsh, 1967). Averaging of these power spectra in effect increases the number of degrees of freedom of the estimate, and thereby decreases the noise variance of the power estimate for each

individual frequency. The relationship between this single channel estimate and its variance is unknown at this time (Lacoss, 1971). Also, the numbers of autocorrelation lags necessary to describe efficiently the MLM power spectrum is unknown. The analysis of synthetic data may shed some light as to the number of autocorrelation coefficients necessary to describe the MLM power spectrum as well as the spectrum's resolution and stability properties. These properties will be considered in the next section.

6.2.2 Examples of the Maximum Likelihood Method (MLM)

Considering first noise-free synthetic data (Figure 5.1) it was found that the best MLM power spectral estimate (Figures 6.1 and 6.2) is provided by using the autocorrelation function (Equation 5.10) given in Section 5.5.1. The number of autocorrelation coefficients used corresponds to the number of digital data points in the time series interval, thereby taking advantage of all possible values. Fewer lags than this lead to a calculated power spectrum which tends to deviate further from the analytical spectrum as the number of lags is decreased. This effect therefore gives rise to a calculated power estimate with a larger power content beyond the predominant frequency than is actually present, eventhough, using all the available autocorrelation coefficients, the calculated MLM spectrum will tend to indicate a smaller t* value than is actually present.

Another important consideration is the spectral dynamic range of the method. To determine this property a larger attenuation factor t* is imposed on the noise-free synthetic time series to extend the dynamic range of power in the frequency range of interest. The analytical power spectra (solid line) along with the MLM solution dashed line are given in Figures

Figure 6.1 A comparison of the exact Fourier power spectrum (solid line) of the non-dispersive synthetic wavelet given in Figure 5.1h with the Maximum Likelihood spectral method (dashed line).

Figure 6.2 Same as for Figure 6.1, except that the example is for the spectrum of the wavelet given in Figure 5.1g.

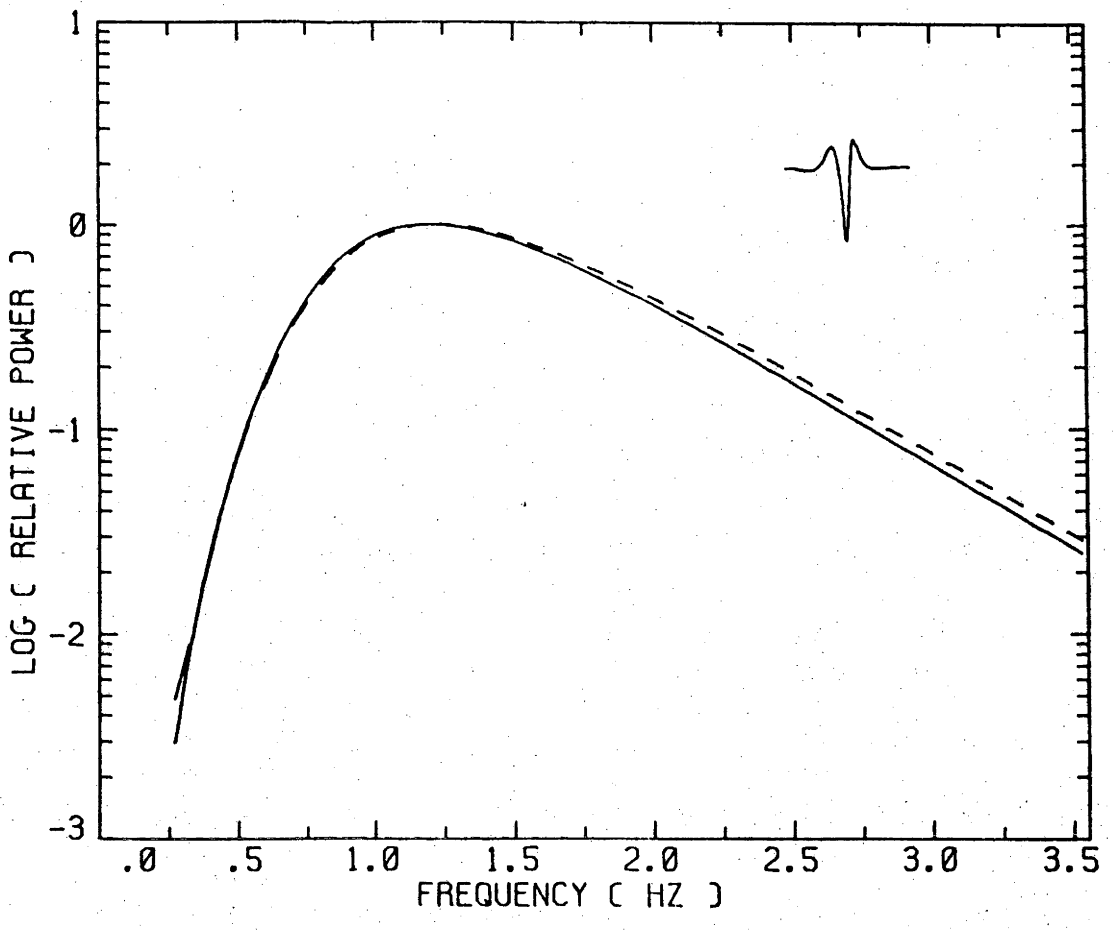
1
0
-1
-2
-3
LOG (RELATIVE POWER)
.0
.5
1.0
1.5
2.0
2.5
3.0
3.5
FREQUENCY (HZ)

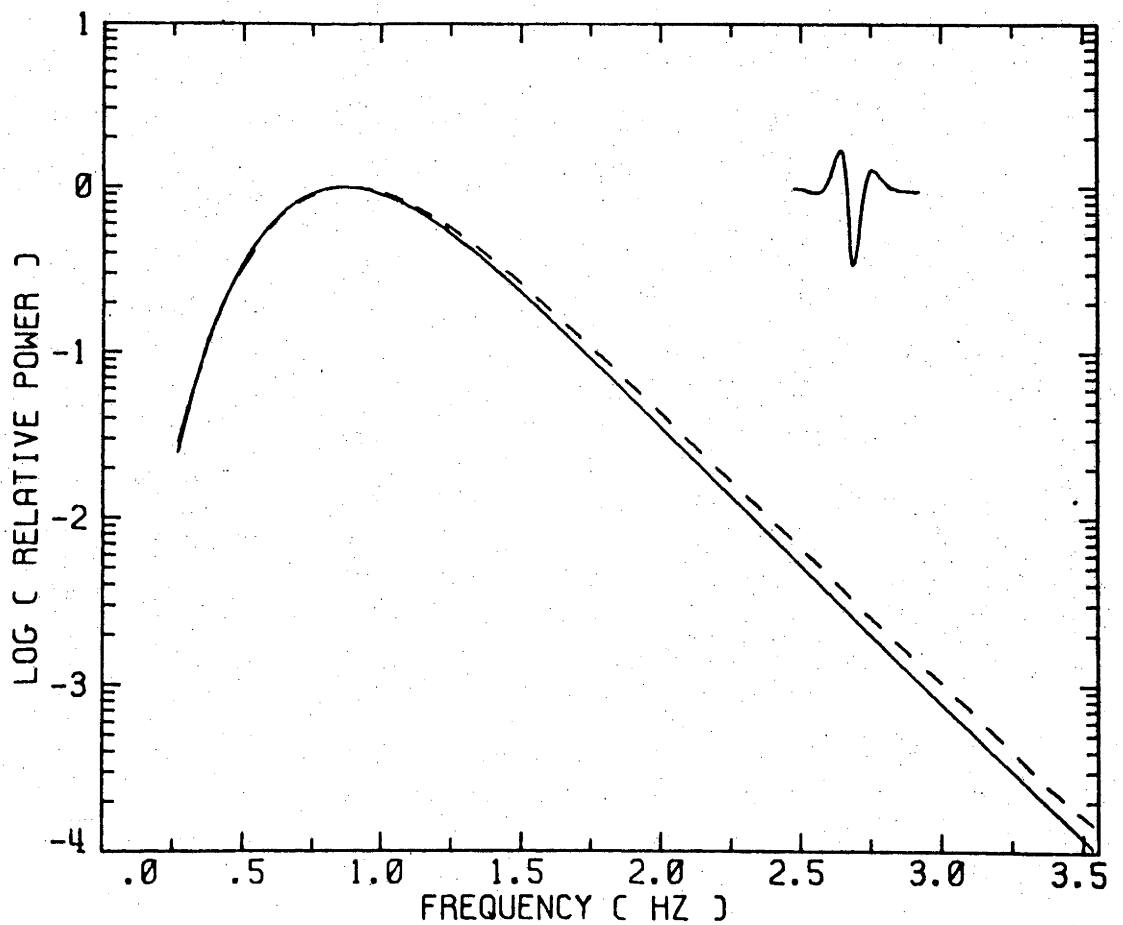
1
0
-1
-2
-3
-4
LOG (RELATIVE POWER)
.0
.5
1.0
1.5
2.0
2.5
3.0
3.5
FREQUENCY (HZ)

6.3 and 6.4. It can be seen from these figures that the usable dynamic range is no greater than 48 dB. As will be shown, a better power estimate can be achieved by pre-whitening the time series with a quasi-difference filter (Jenkins and Watts, 1968; Koopmans, 1974) prior to the computation of the MLM spectrum. Such a filtered time series Y(t) can be written in terms of its actual time series X(t) representation as

$$Y(t) = X(t) - \alpha X(t-1) \qquad 6.17$$

where the constant α determines the response of this high pass filter. The spectral response $|G(\omega)|^2$ of this filter can then be written as

$$|G(\omega)|^2 = 1 - 2\alpha \cos \omega + \alpha^2 \qquad 6.18$$

and the phase as

$$\phi(\omega) = \tan^{-1} \left(\frac{\alpha \sin \omega}{1 - \alpha \cos \omega}\right) \quad . \qquad 6.19$$

Pre-whitening the time series serves to reduce the amount of low frequency power and broadens the overall spectrum, giving rise to a more balanced spectrum. A time series with a gentle sloping of spectral power on both sides of a main peak in the spectrum leads to an analysis which gives a better representation of power present in a spectrum than those time series whose spectra are distorted in some other fashion. Pre-whitening the time series (Equation 6.17) and post-colouring the modified MLM spectra by the division of Equation 6.18 were tested through the use of synthetic data. The same synthetic wavelets used in Figure 6.3 and 6.4 were used and examples of pre-whitened and post-coloured estimates are given in Figure 6.5 and 6.6 respectively. Comparing these figures it can be readily seen that the actual spectrum (dashed line) in the pre-filtered case is a much closer fit

Figure 6.3 A comparison of exact Fourier Power Spectrum (solid line) and the Maximum Likelihood spectrum (dashed line) for the highly attenuated non-dispersive synthetic wavelet given in the upper right hand corner. The parameters are 1.0 second and 1.0 Hz for the t* and the corner frequency respectively.

Figure 6.4 The same as for Figure 6.3 except that t* is equal to 1.2 seconds.

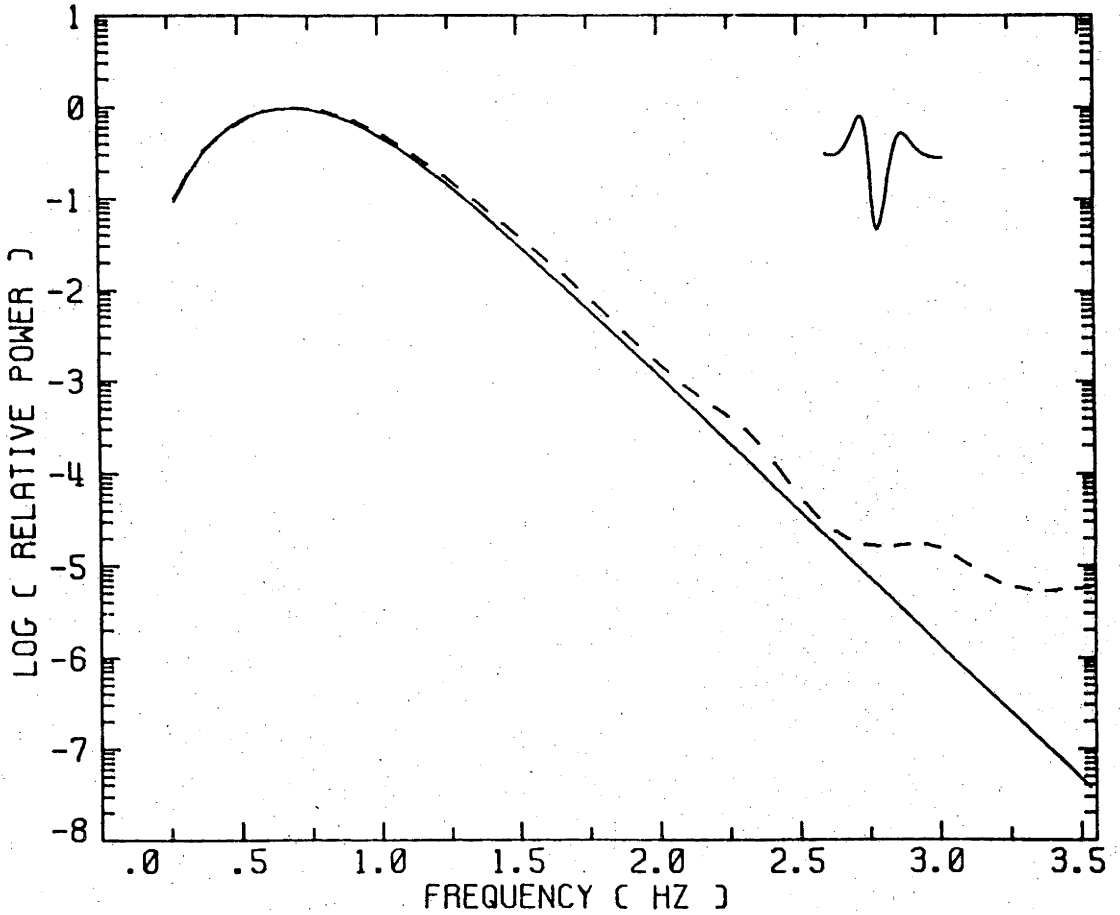
LOG (RELATIVE POWER)
1
0
-1
-2
-3
-4
-5
-6
-7
-8
.0
.5
1.0
1.5
2.0
2.5
3.0
3.5
FREQUENCY (HZ)

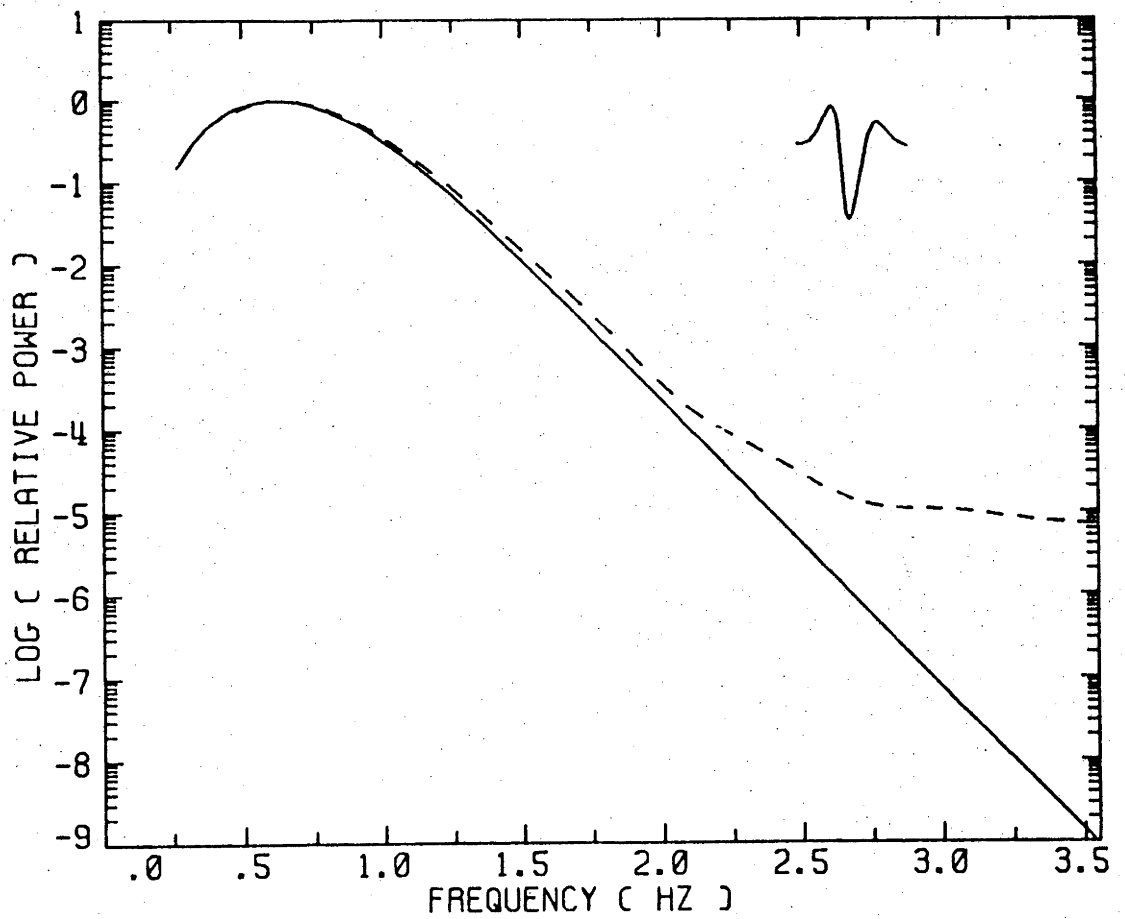
LOG (RELATIVE POWER)
1
0
-1
-2
-3
-4
-5
-6
-7
-8
-9
.0
.5
1.0
1.5
2.0
2.5
3.0
3.5
FREQUENCY (HZ)

Figure 6.5 Same as for Figure 6.2 except that the non-dispersive synthetic wavelet was pre-whitened and post-coloured using the first difference equation given in text. The pre-whitening coefficient α is 0.35.

Figure 6.6 Same as for Figure 6.4 except that the non-dispersive synthetic wavelet was pre-whitened and post-coloured using the first difference equation given in text. The pre-whitening coefficient α is 0.55.

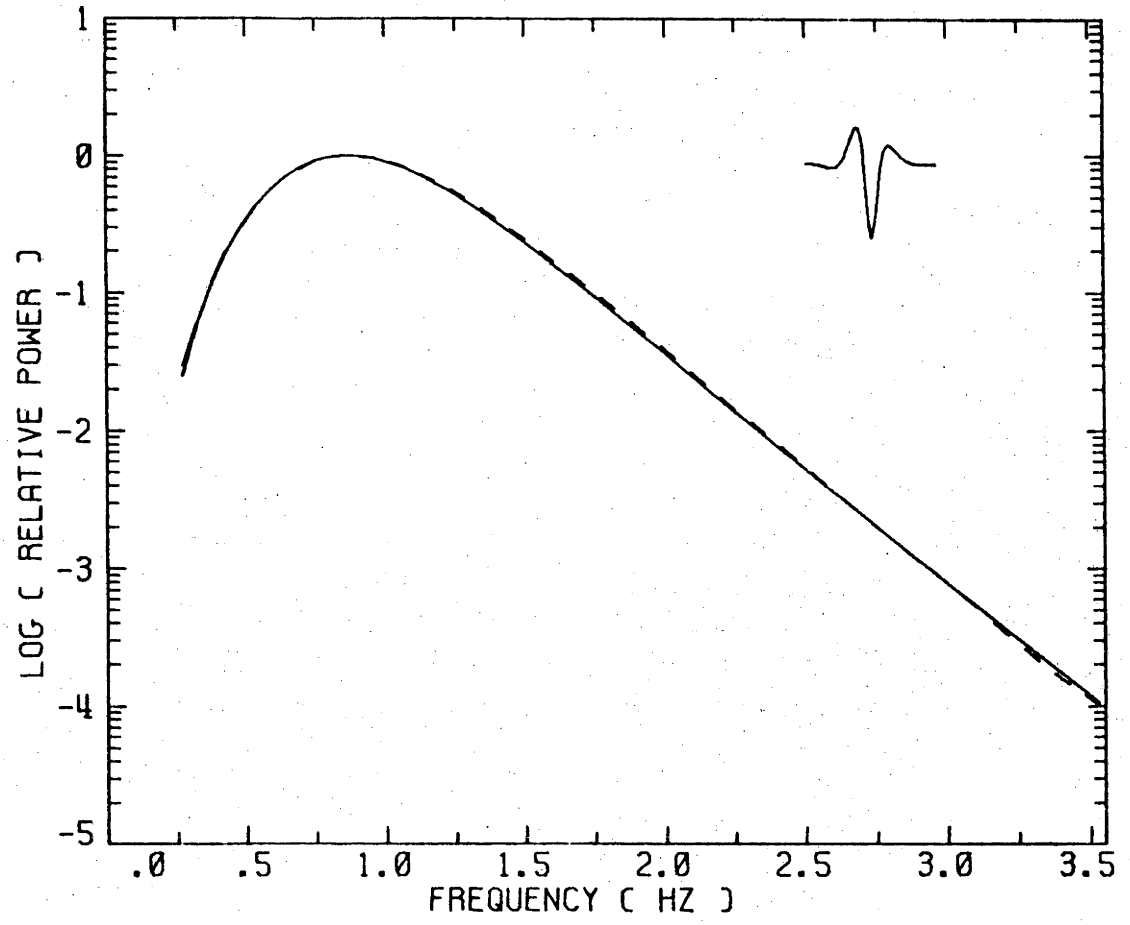
LOG (RELATIVE POWER)
1
0
-1
-2
-3
-4
-5
.0
.5
1.0
1.5
2.0
2.5
3.0
3.5
FREQUENCY (HZ)

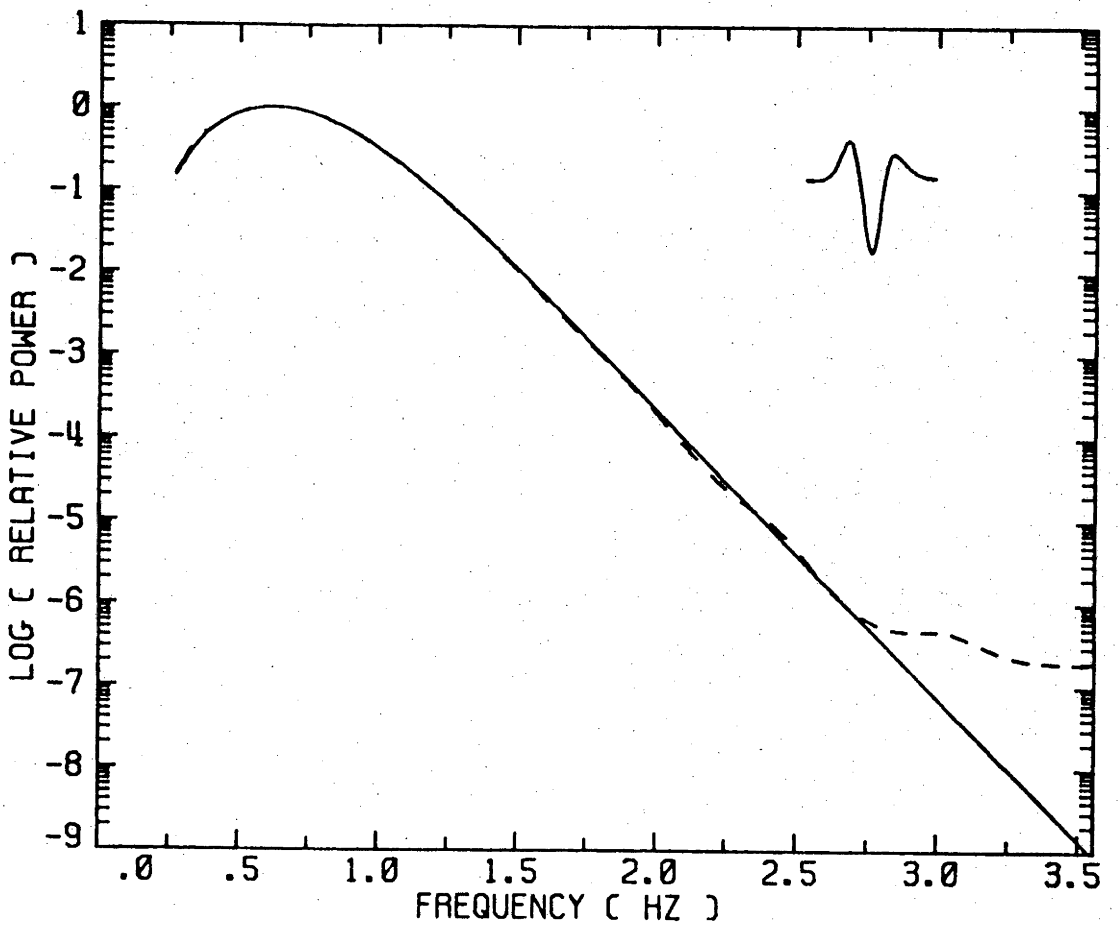
LOG (RELATIVE POWER)
1
0
-1
-2
-3
-4
-5
-6
-7
-8
-9
.0
.5
1.0
1.5
2.0
2.5
3.0
3.5
FREQUENCY (HZ)

to the exact (solid line) spectrum than the unfiltered case. What is more, in the extremely attenuated case in Figure 6.6 the power dynamic range is increased some 16dB over that given in Figure 6.4. The main problem in the above procedure is to determine the best choice of the constant α. No analytical method of determining α has been found by this author. The values of α given in Figure 6.5 and 6.6 were found by a trial-and-error procedure. It may be possible, however, to predict the best value of α based upon a preliminary estimate of the predominant frequency or the high frequency of roll-off using synthetic data. A graph of α versus the predominant frequency or the high frequency roll-off would lead to an empirical choice of α. This procedure for picking α serves only to improve the MLM power estimates for data considered in this thesis. It may not in itself be a sufficient method for pre-whitening spectra of another type.

Another method for pre-whitening spectra which may be useful is to estimate the first few autoregressive prediction error coefficients by the methods described in the previous section. Convolving these prediction error coefficients with the time series under study should yield a pre-whitened time series with most of the dominant power removed. Since most spectral techniques work best on a spectrum which is flat, the MLM should therefore return high resolution for this whitened spectrum. Post-colouring the MLM spectrum should yield a power spectrum very close to the actual power contained in the time series under study.

A third pre-whitening method is to make use of infinite - or finite - duration response filters. Many examples of IIR and FIR digital filters can be found in the literature (Oppenheim and Schafer, 1975). Great care must be taken to ensure that the pre-whitening filter does not ramp too fast between the passband edge and stopband edge frequencies. Another problem

with this type of filter is ripple which is associated with the filter response. The design of such filters should be made to suppress such ripple so that their influence will be insignificant upon post-colouring. The use of IIR and FIR digital filters will cause phase distortion in the time series to be pre-whitened. However, since the concern here is only in the real part of Q, the phase distortion presents no problem.

Upon applying the above techniques to real P phase data given in the previous section, the MLM spectra were found to be much smoother than those spectra obtained by the Fourier transform method. This is because the MLM adapts itself appropriately to the windowed data (Lacoss, 1971, 1977). Furthermore, the pre-whitened and post-coloured method gives a better spectral representation of this real data.

As in the Fourier power spectra (Figure 5.2 through 5.5), the only thing removed from the MLM spectra (Figure 6.7 through 6.10) is the instrumental response. The dashed lines in these figures are the least-squares fit, to be discussed in a later chapter, on the MLM spectra. The dot-dash lines in Figure 6.7 through 6.10 are the extension of the data not used in determining the least-squares fit. These data are considered to be at the baseline of the spectra and only representative of white noise.

In conclusion, the best estimate of the power content for a real segment of seismic time data is obtained from the pre-whitened and post-coloured MLM power spectrum. Adaptive windowing of the data is far more superior than Fourier spectral technique approaches when the time series is short. No peaking of the spectral power occurs around the predominant frequency as in the case of the Yule-Walker or Burg's Maximum Entropy methods. The only problem that still remains is coherent noise (i.e. microseisms, crustal reflections, etc.) which is not discriminated

Figure 6.7 Maximum Likelihood Spectral estimate (solid line) of the truncated seismic P phase wavelet shown in Figure 5.1a with the displacement instrumental response removed. The dahsed line is the least-squares fit (to be discussed in Chapter 7) for source and attenuation responses, while the dot-dash line is the portion of the data not used for the fit. Specific values for the corner frequency (C.F.) and t* are 1.08 Hz and 0.462 ± 0.063 seconds respectively. Note the slight curvature in the dashed line due to the source spectrum.

Figure 6.8 Same as for Figure 6.7 except that the truncated seismic wavelet given in Figure 5.1b was used. The calculated values for the corner frequency (C.F.) and t* are 1.25 Hz and 0.297 ± 0.052 seconds respectively. Note that all data were used for the least squares fit.

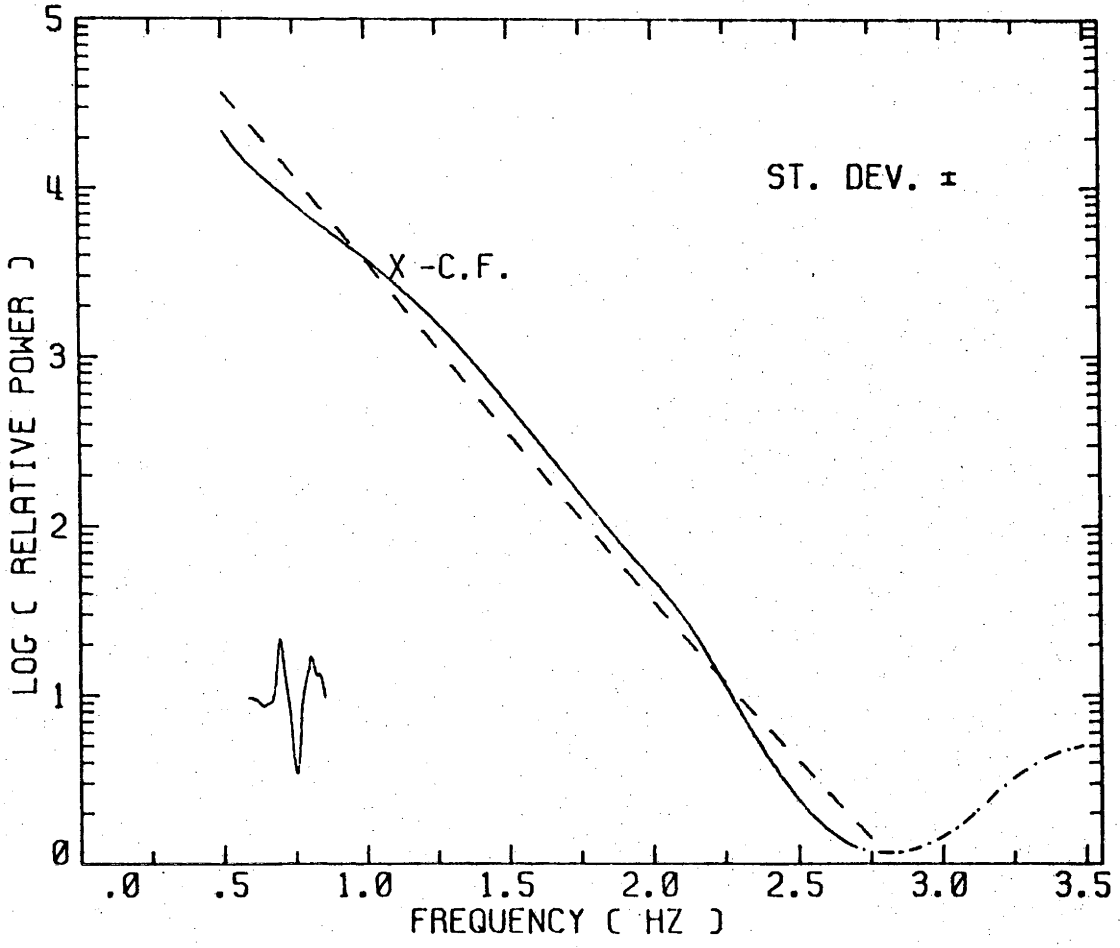
ST. DEV. ±
X -C.F.
LOG (RELATIVE POWER)
FREQUENCY (HZ)
5
4
3
2
1
0
.0
.5
1.0
1.5
2.0
2.5
3.0
3.5

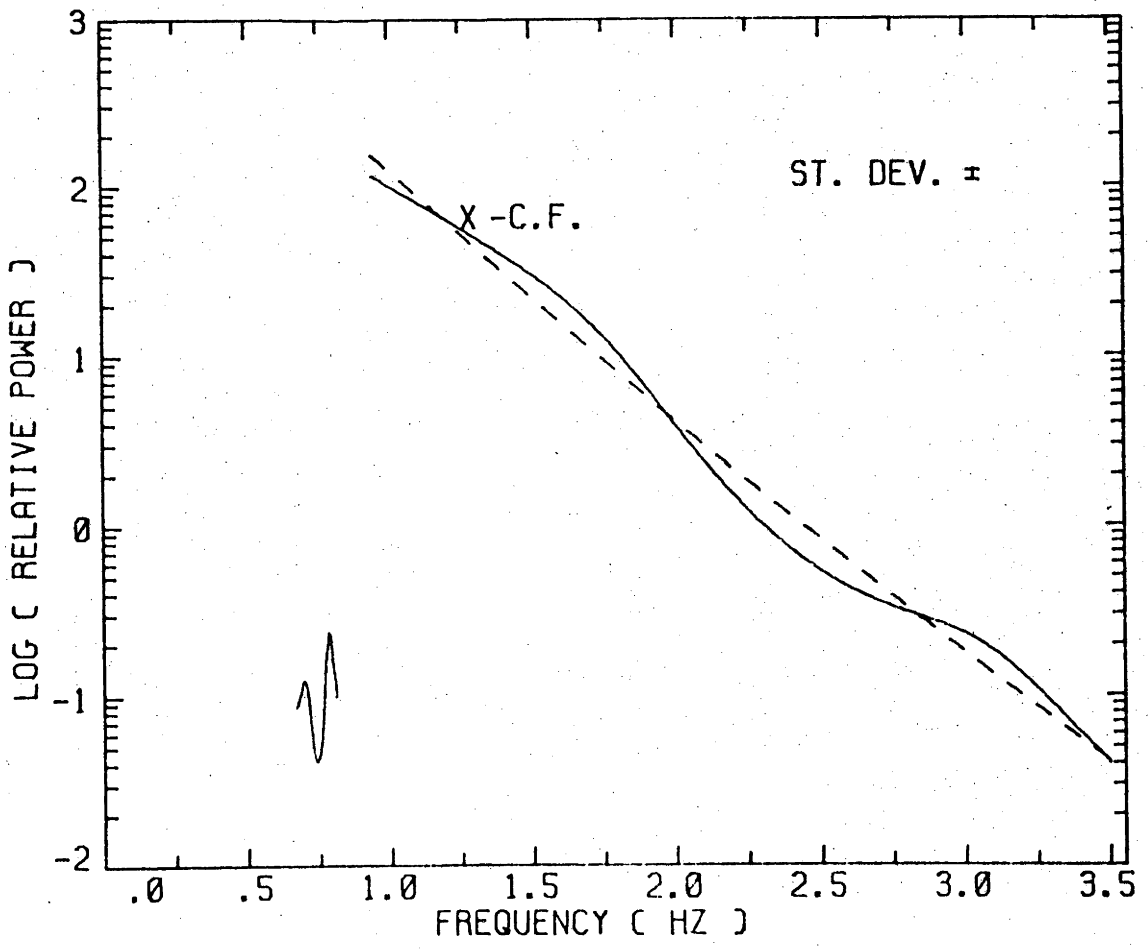
ST. DEV. ±
X -C.F.
LOG (RELATIVE POWER)
FREQUENCY (HZ)
3
2
1
0
-1
-2
.0
.5
1.0
1.5
2.0
2.5
3.0
3.5

Figure 6.9 Same as for Figure 6.7 except that the truncated seismic wavelet given in Figure 5.1c was used. The calculated values for the corner frequency (C.F.) and t* are 0.98 Hz and 0.434 ± 0.066 seconds respectively. The dot-dash line is the data not used for the least squares fit.

Figure 6.10 Same as for Figure 6.7 except that the truncated seismic wavelet given in Figure 5.1d was used. The calculated values for the corner frequency (C.F.) and t* are 1.46 Hz and 0.210 ± 0.056 seconds respectively.

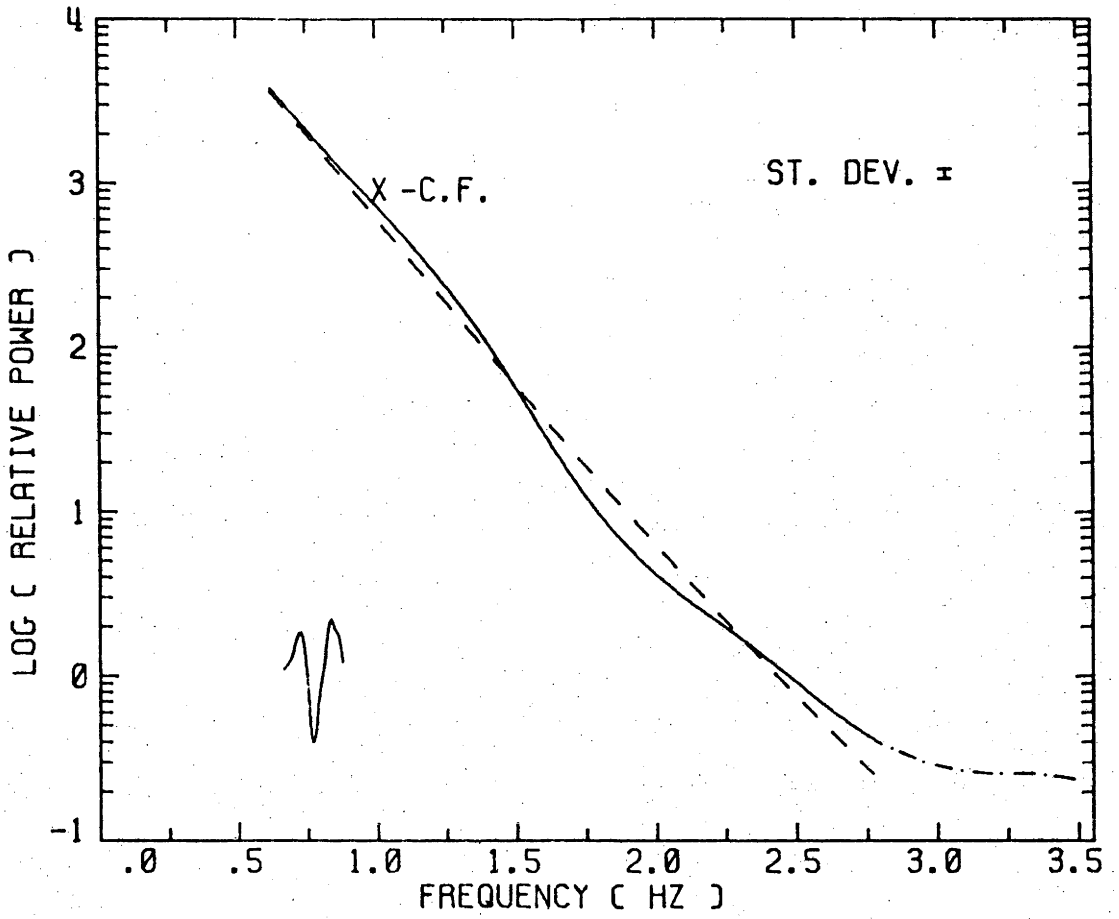
4
3
2
1
0
-1
LOG (RELATIVE POWER)
X -C.F.
ST. DEV. x
.0
.5
1.0
1.5
2.0
2.5
3.0
3.5
FREQUENCY (HZ)

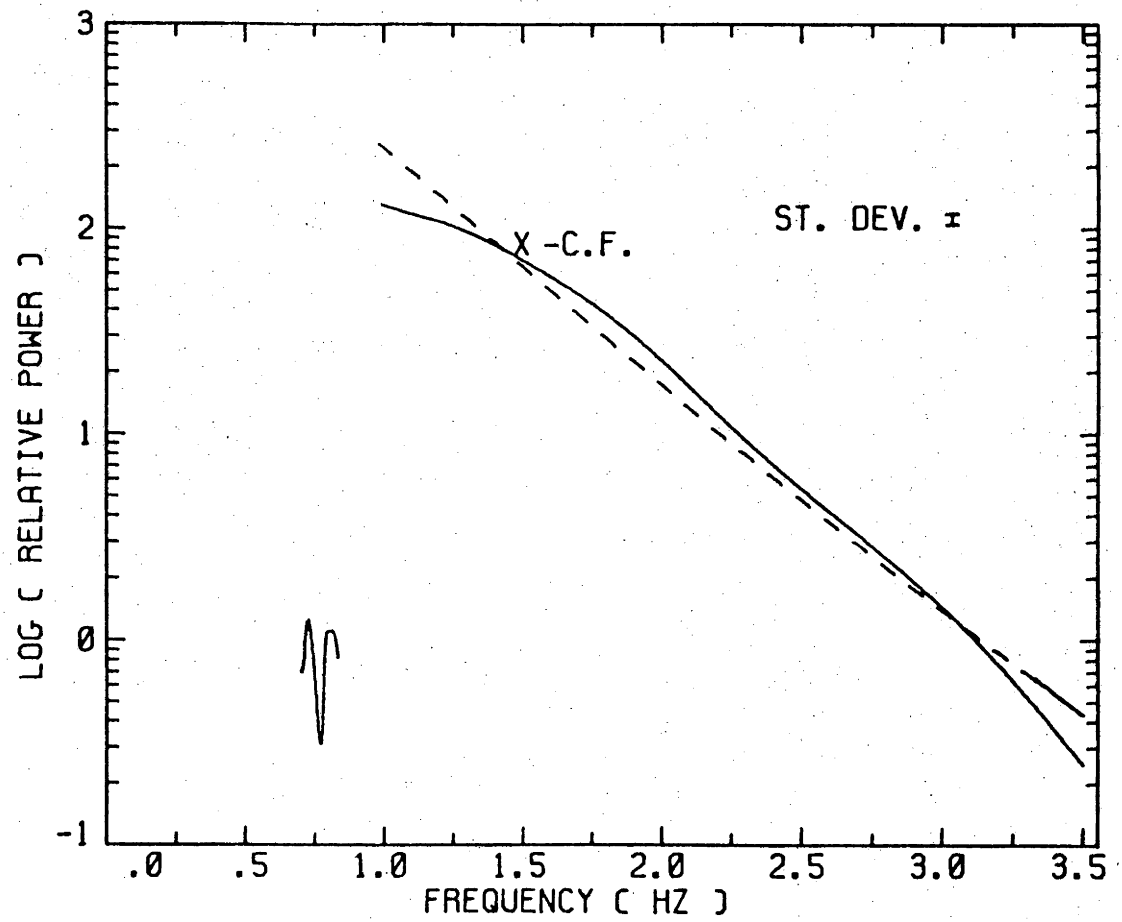
3
2
1
0
-1
LOG (RELATIVE POWER)
X -C.F.
ST. DEV. x
.0
.5
1.0
1.5
2.0
2.5
3.0
3.5
FREQUENCY (HZ)

against by any of the spectral methods thus far considered. Noise discrimination will be considered in the section on Homomorphic Deconvolution.

6.3 Estimation of t* by Homomorphic Deconvolution

6.3.1 Theory

As pointed out in previous sections, an estimate of the true power spectrum cannot be made by a parameter-fitting modelling technique because the time series is not a true autoregressive time sequence. The Maximum likelihood method does appear to window a truncated time series properly because of insensitivity to the edges of the data. However MLM cannot account for correlatable noise properties or impulse responses which may be present in the windowed seismic time series under study. As pointed out in the last section, use of the Fourier transform to obtain a power spectrum, as shown in Section 5.4, leads to undesirable side-lobe effects. The removal of the two above-mentioned undesirable effects may be eliminated by non-linear spectral techniques such as Homomorphic Deconvolution. This technique has been extensively studied by Oppenheim, Schafer and Stockton (1968), who show how it can be effectively used for image enhancement and echo removal. Later, Ulrych (1971), Ulrych et al., (1972), and Lines and Ulrych (1977), used this technique to remove the impulse response of the crust from the primary seismic wavelet. Ulrych (1971) suggests that homomorphic deconvolution may be useful for the determination of attenuation in the earth. A brief outline of this technique will be given here to demonstrate how it can be applied to determining t* values.

In principle, the technique transforms a time series which consists of multiplied or convolved terms into a time series which consists of terms

in addition. Mathematically this is achieved by the following steps:

(1) Compute the Fourier transforms of the seismic wavelet time series X(n).

(2) Compute log of the amplitude spectrum and unwrap the phase spectrum in order to make the total expression analytical (Oppenheim and Schafer, 1975). Generally at this point the linear phase component is removed.

(3) Compute the inverse Fourier transform of the amplitude and phase spectra resulting in the complex cepstrum $\hat{X}(n)$.

(4) Filter the complex cepstrum by linear filtering. This process separates the various components of the spectrum. How this is done will be explained later in an actual example.

(5) Compute the Fourier transform of the filtered complex cepstrum.

(6) Compute the exponential of the Fourier transform and replace the linear component of the phase removed in Step 2.

(7) Compute the inverse Fourier transform to recover the deconvolved wavelet.

Figure 6.11 shows, by means of a block diagram, the above steps. From this diagram it is easy to see that if no filtering is done, the time sequence X(n) will return the same time series X(n) at the end of the processing. This must be true in order that this estimating method is a consistent one.

A serious drawback to homomorphic deconvolution is the correct procedure for unwrapping the phase position of the estimate in Step 2. This phase unwrapping becomes more difficult if random noise is present in the time series being analysed, the reason being that the phase portion of the noise is random, resulting in an uncertainty in the direction in which the phase spectrum should go . To overcome this problem Tribolet (1977)

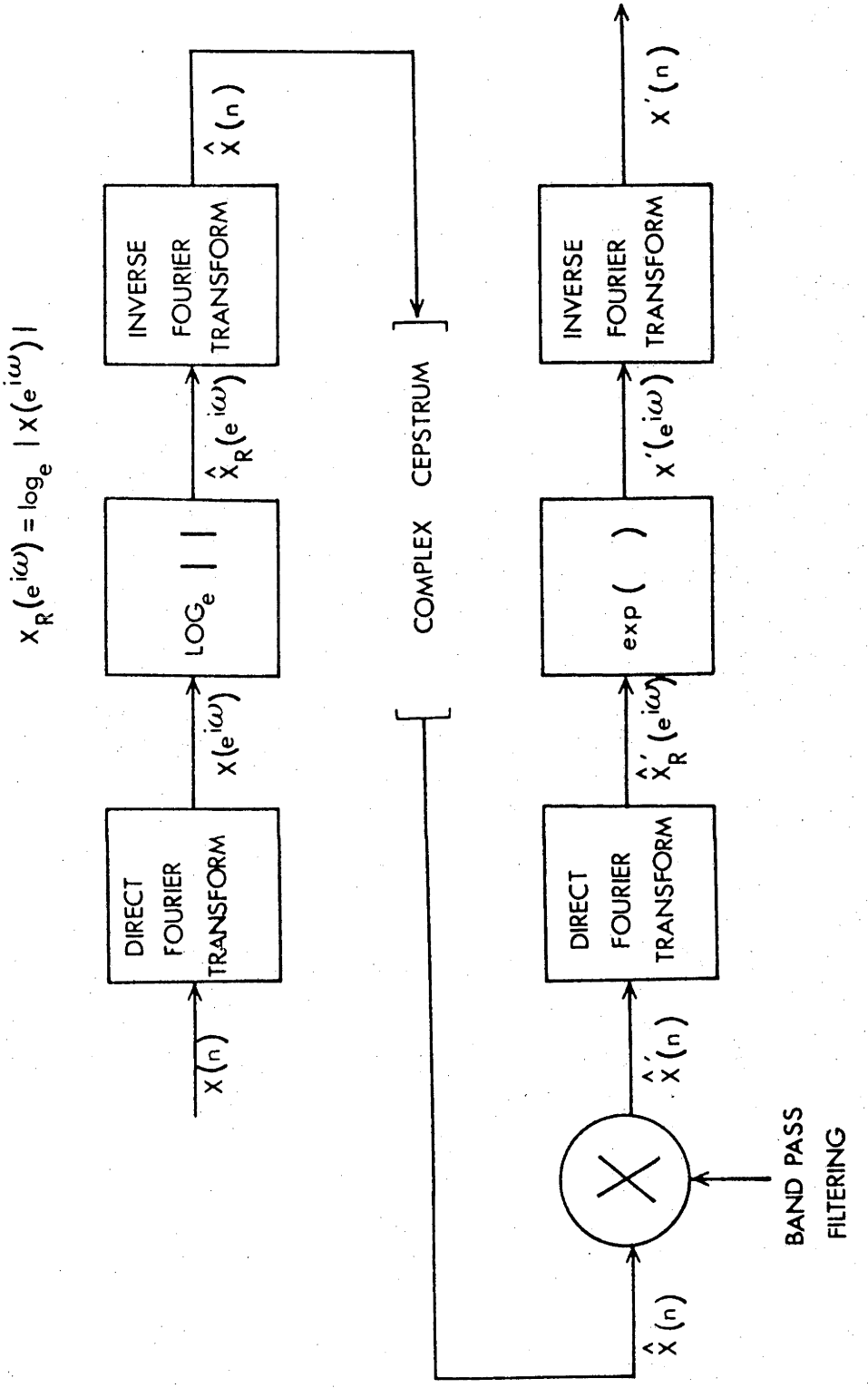

Figure 6.11 Block diagram demonstrating the Homomorphic Deconvolution process.

suggests that the most effective method for phase unwrapping is by adaptive integration of the phase derivative. This method works well for the spectra examined in this thesis, as will be demonstrated in the next section. At this stage it is worth remarking that the computer program given by Tribolet has some serious computational errors which must be corrected before its use.

6.3.2 Examples of t* Estimates Using the Homomorphic Deconvolution Technique

Considering next the problem of how this technique can be used to determine t* values for the mantle, the wavelets in Figure 5.1 will be used to test the homomorphic deconvolution technique. Using the procedure outlined above (Steps 1 through 3) the complex cepstrum is obtained (Figure 6.13 and 6.16). Note the equally spaced spike(s) on the left-hand side of the complex cepstrum in Figures 6.15 and 6.16. Observation reveals that these spikes are of the same time length as the original data. Therefore these spikes are associated with the manner in which the time series is windowed. Filtering applied to the complex cepstrum is used to remove these windowing effects in the Fourier power spectra (Figures 5.2 and 5.5). The filter has a weight of unity over the complex cepstrum to be conserved and zero over the portion to be eliminated. There are four such filters considered here; these are (a) low pass, (b) high pass, (c) band pass, and (d) comb filters. These are demonstrated in Figure 6.12. However, because of the simplicity, and the fact that they were adequate, only low pass and high pass filters have been used throughout this analysis. Since the complex cepstrum falls off very rapidly from the center values, the low pass or high pass filters will add little distortion to the original

Figure 6.12 (a) The general drop-off of the complex cepstrum is indicated as a function of positive and negative time. (b), (c), (d) and (e) are examples of Low Pass, High Pass, band Pass and comb filter which can be used to filter a complex cepstrum.

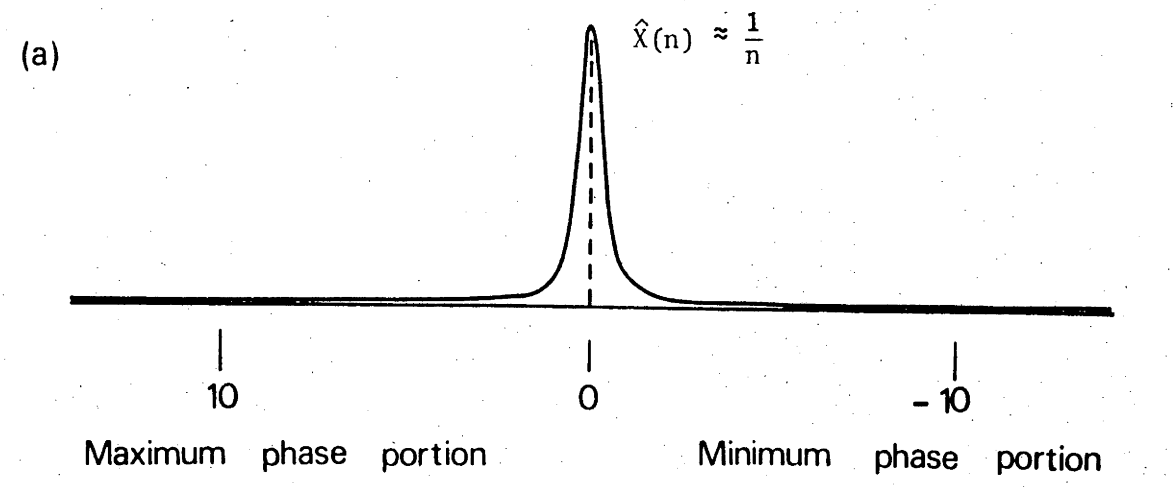
(a)
$\hat{X}(n) \approx \frac{1}{n}$
10
0
-10
Maximum phase portion
Minimum phase portion

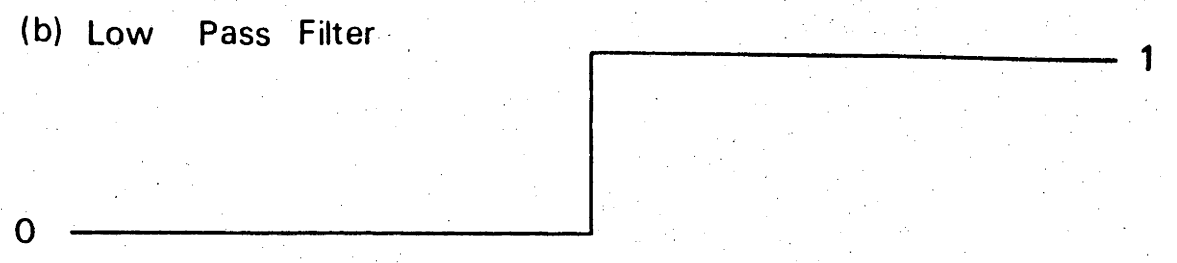
(b) Low Pass Filter
1
0

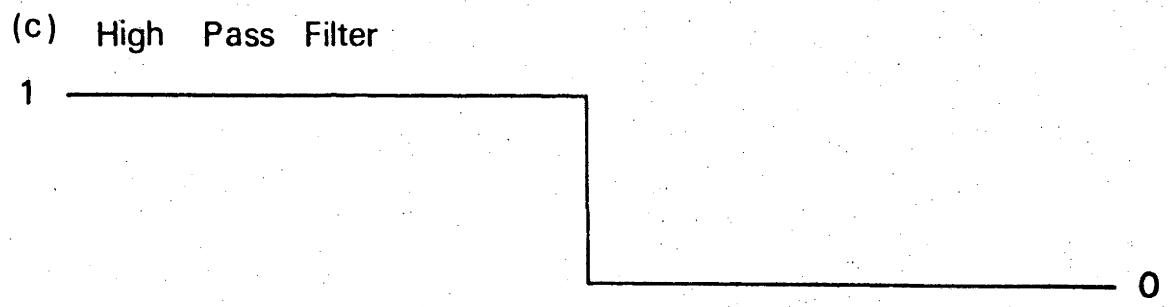
(c) High Pass Filter
1
0

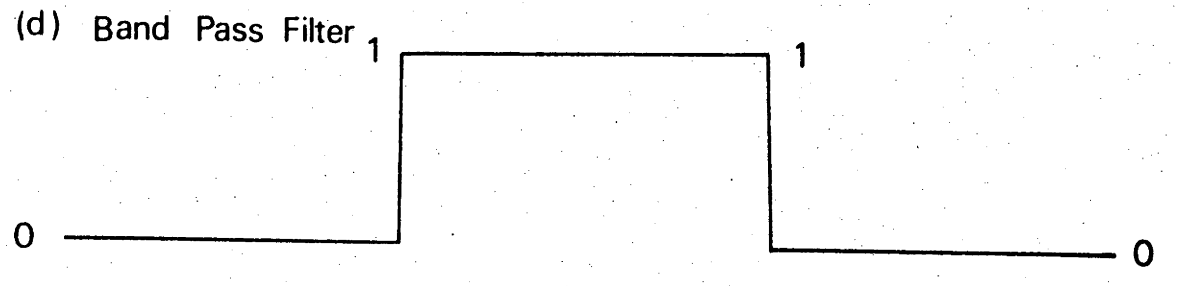
(d) Band Pass Filter
1
1
0
0

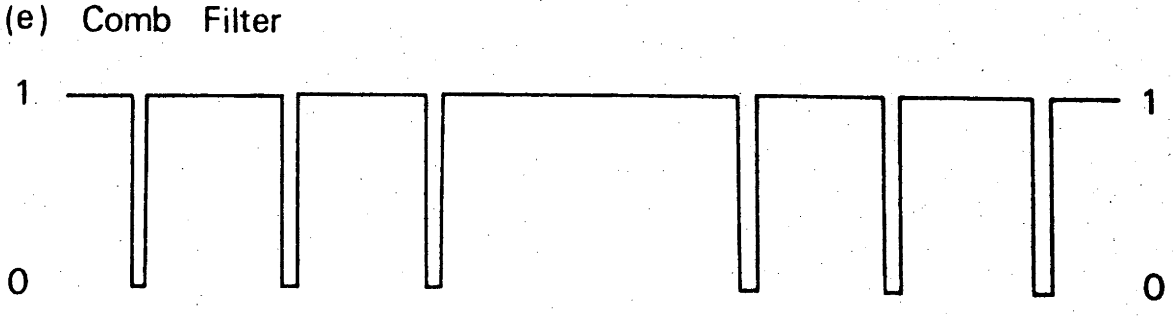
(e) Comb Filter
1
1
0
0

Figure 6.13 A demonstration of the application of the Homomorphic Deconvolution technique to the seismic wavelet given in Figure 5.1a. At the top of this figure is the filter used to filter the complex cepstrum which appears next in the figure. The lower half of this shows the resulting power displacement spectrum of the source (solid line). The dashed line is the least-squares fit for this spectrum. The dot-dash line is the portion of the data not used in the least-squares fitting interval. The estimated values for the corner frequency (C.F.) and t^*_α are 0.87 Hz and 0.518 ± 0.099 seconds respectively. Note: The only change in the original data is the smoothing out of the trailing edge of the time series (shown in the lower left hand corner of box).

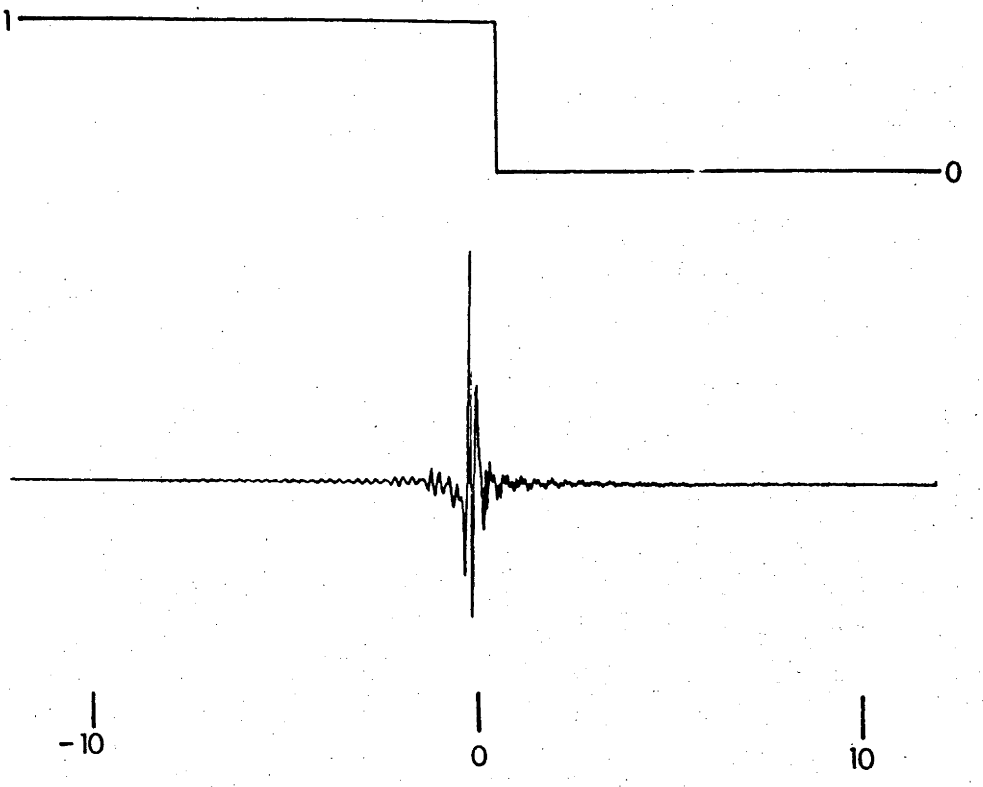
1
0
-10
0
10

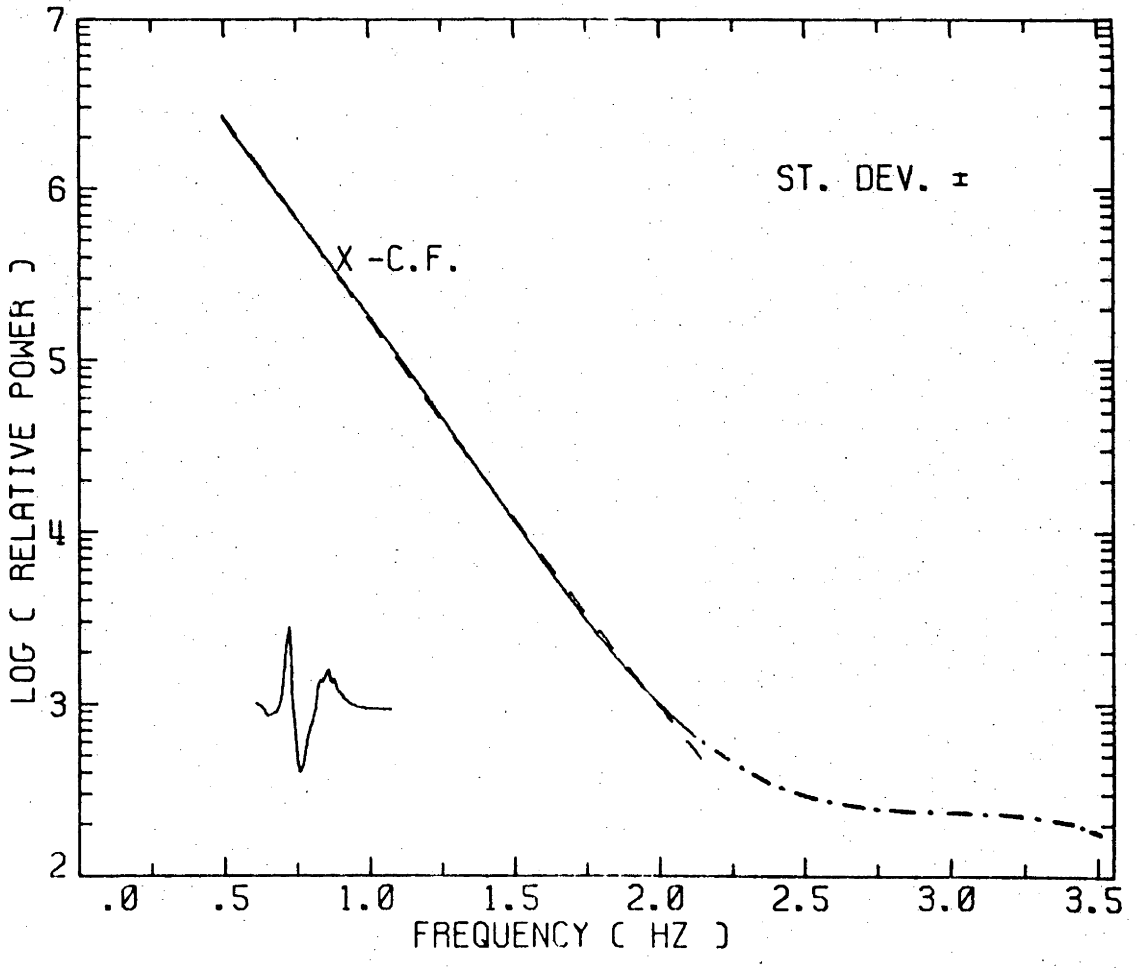
7
6
5
4
3
2
LOG (RELATIVE POWER)
ST. DEV. ±
X -C.F.
.0
.5
1.0
1.5
2.0
2.5
3.0
3.5
FREQUENCY (HZ)

Figure 6.14 The same as for Figure 6.13 except that the analysis is performed on the seismic wavelet as shown in Figure 5.1b. Estimates for the corner frequency (C.F.) and t* are 1.25 Hz and 0.374 ± 0.052 seconds respectively using the Homomorphic Deconvolution technique.

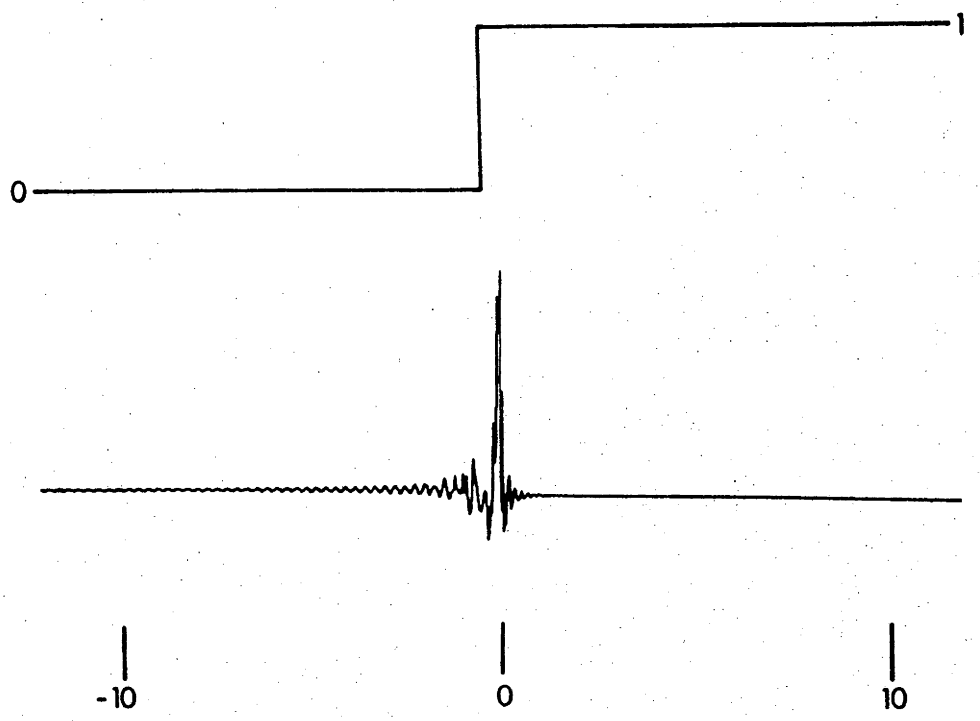
1
0
-10
0
10

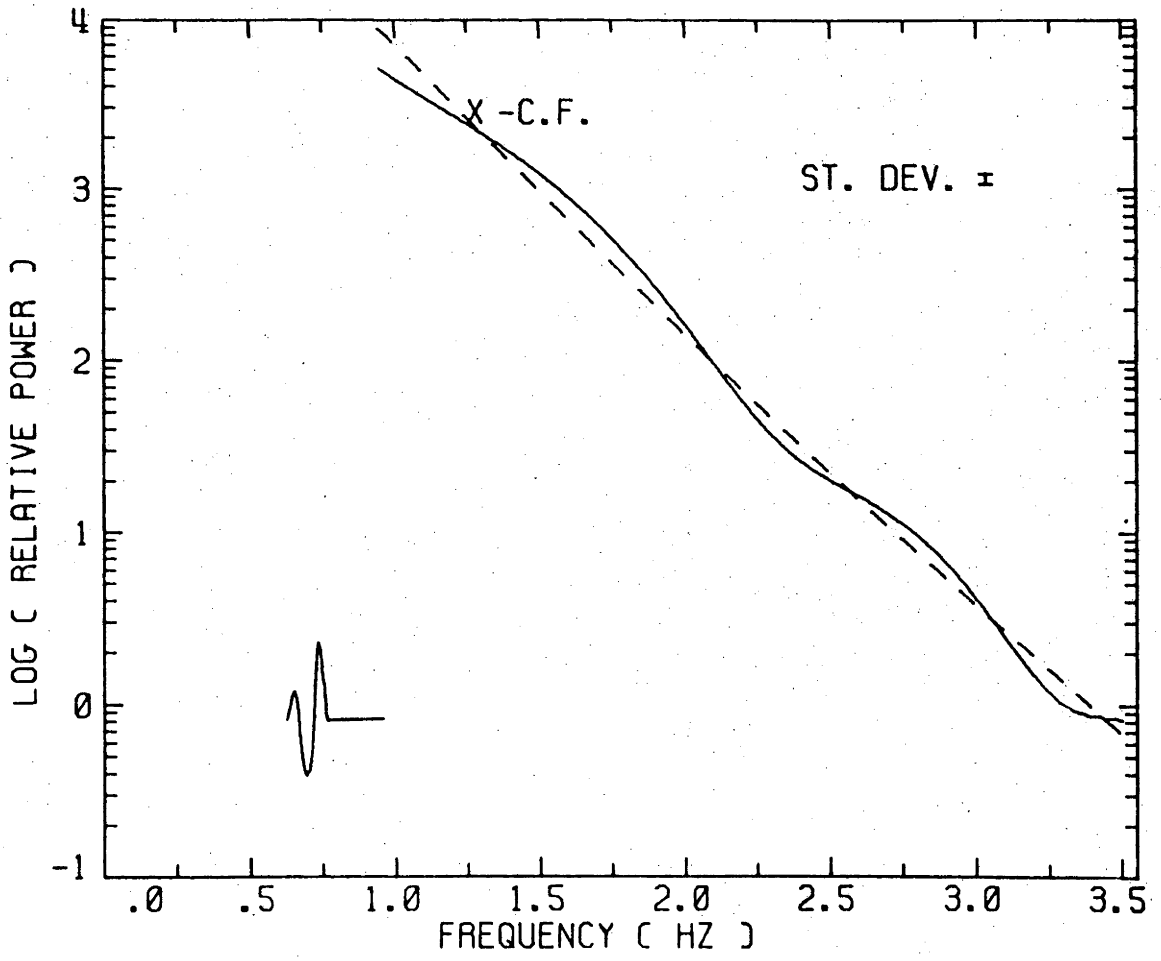
X -C.F.
ST. DEV. ±
LOG (RELATIVE POWER)
4
3
2
1
0
-1
.0
.5
1.0
1.5
2.0
2.5
3.0
3.5
FREQUENCY (HZ)

Figure 6.15 The same as for Figure 6.13 except that the analysis is performed on the seismic wavelet shown in Figure 5.1c. Estimates for the corner frequency (C.F.) and t* are 0.99 Hz and 0.388 ± 0.041 seconds respectively. The arrow indicates the spike in the complex cepstrum caused by the truncation of the seismic wavelet.

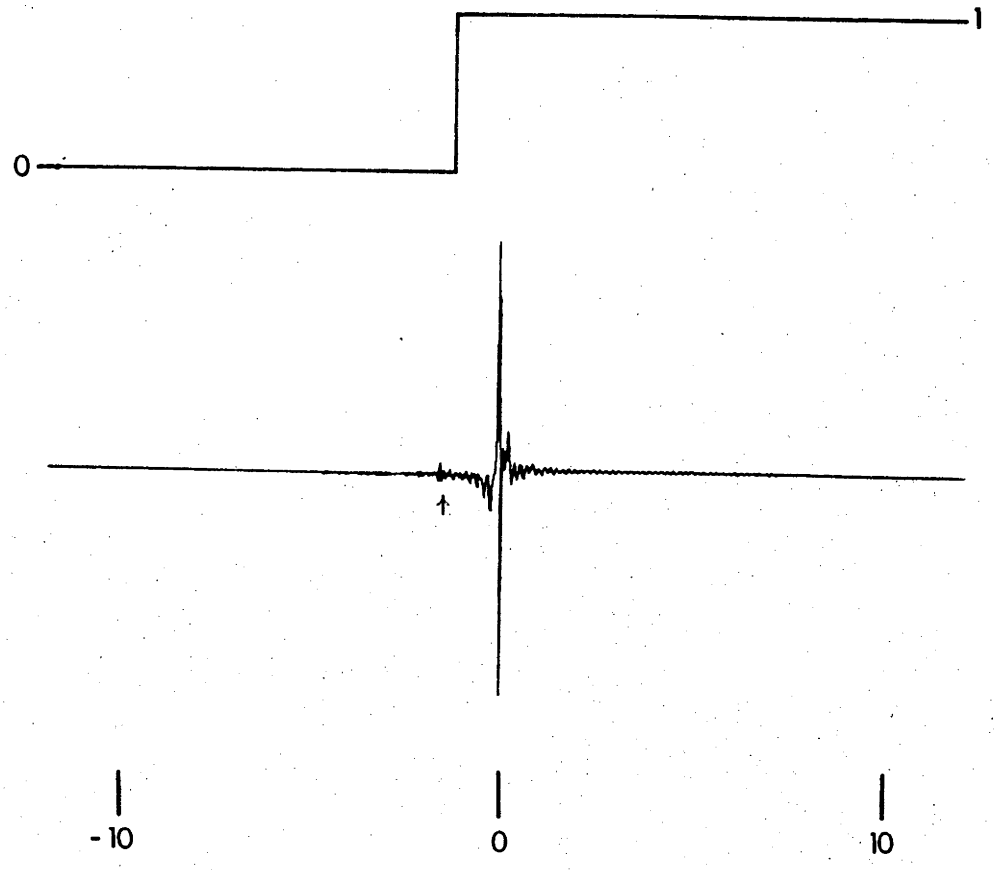
1
0
-10
0
10

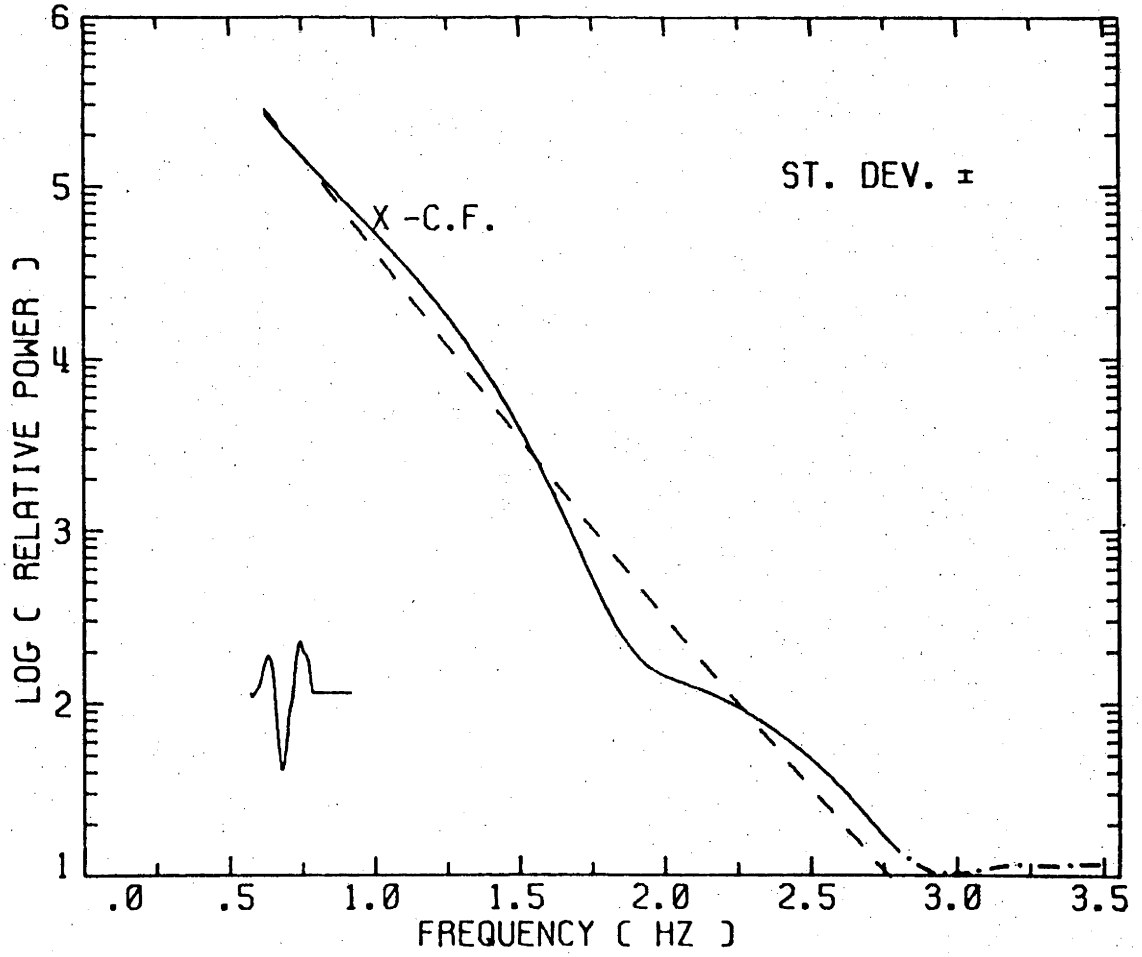
ST. DEV. ±
X -C.F.
LOG (RELATIVE POWER)
6
5
4
3
2
1
.0
.5
1.0
1.5
2.0
2.5
3.0
3.5
FREQUENCY (HZ)

Figure 6.16 The same as for Figure 6.13 except that the analysis is performed on the seismic wavelet shown in Figure 5.1d. Estimates for the corner frequency (C.F.) and t* are 1.34 Hz and 0.37 ± 0.041 seconds respectively. The arrows indicate the spikes in the complex cepstrum caused by the truncation of the seismic wavelet.

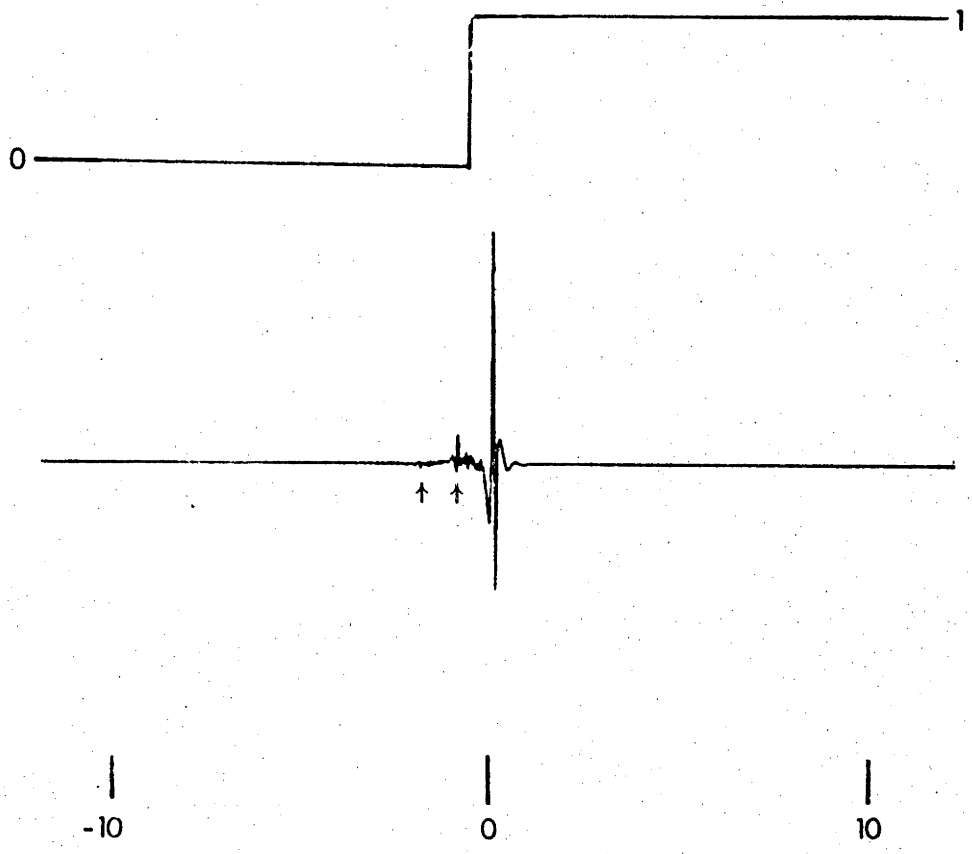
1
0
-10
0
10

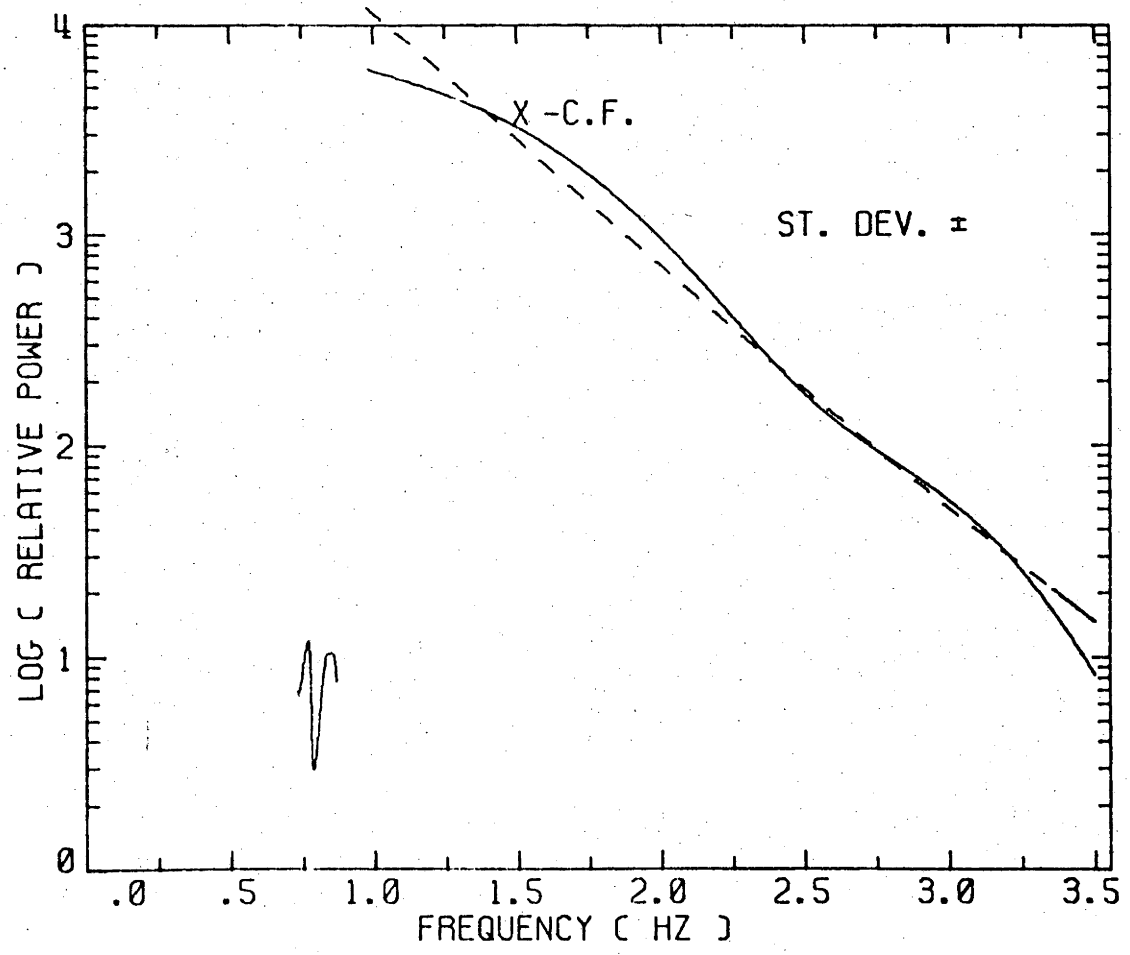
X -C.F.
ST. DEV. ±
LOG (RELATIVE POWER)
4
3
2
1
0
.0
.5
1.0
1.5
2.0
2.5
3.0
3.5
FREQUENCY (HZ)

wavelet. Note that the only change as compared with the original wavelet in the trailing edge occurs where it broadens slightly and tapers off to zero (Figure 6.13). The superiority of the power spectrum, after instrument response is removed, is clearly demonstrated in the examples given in Figures 6.13 through 6.16. The power spectrum drops off smoothly and then flattens out to a base line or white noise spectrum. Therefore a high frequency cutoff must be chosen at the point where the power spectrum becomes meaningless. This is easily achieved since the maximum peak-to-peak amplitude of the wavelet can be determined (which corresponds to the gain at the dominant frequency) and then the zero gain level can be set. Using the above criteria the resulting power spectrum (solid line) is given in Figures 6.13 through 6.16 along with its least-squares fit, (dashed line). The least-squares fitting procedure will be discussed in the following chapter.

In conclusion, some of the reasons why the homomorphic deconvolution technique is an improvement over the standard Fourier technique will be discussed. First, since it is impossible in all cases to obtain the wavelet one wishes to analyse to start and end on the mean value, windowing effects may become important in the final determination of the Fourier power spectrum. The sharp cutoff of data (eventhough it is cosine tapered) may be adding in harmonics of frequencies higher than the Nyquist frequency and folding them back into the power spectrum. As a result, homomorphic deconvolution is acting as an anti-aliasing filter at each end of the data. Secondly, by truncating the wavelet to be analysed necessitated by the presence of other interfering incoming wavelets, some of the wavelet is being cut off, thereby making the wavelet non-analytic. This in effect is the same as convolving the spectrum with a sinc function. Homomorphic

deconvolution could therefore be, in part, separating the sinc function away from the true spectrum. This is in effect a prediction of the end of the wavelet, which was lost in other incoming wavelets, causing the original wavelet to be more analytic, (Bath, 1974).

6.4 Conclusions to the Maximum Likelihood and Homomorphic Deconvolution Techniques

As demonstrated in this chapter, the Maximum Likelihood method (MLM) given by Lacoss (1971) and the Homomorphic deconvolution technique given by Oppenheim et al., (1968) are considerably superior (for this application) to those given in the previous chapter. However, these techniques are not without their drawbacks. For example, the MLM tends to indicate a power content at the higher frequency ranges higher than actually present, which results in an estimate of t* about 0.05 seconds less that the actual value. This error in power can be reduced by pre-whitening the time series prior to spectral analysis. More effort in methods for pre-whitening such time series as considered here should not go unrewarded.

The MLM has the ability to discriminate between a stochastic process (white noise) and the signal. Correlatable noise arising from source and crustal effects would, however, be considered as signal by this technique. In an attempt to remove correlated noise, Homomorphic Deconvolution was used. If the correlated noise appears as echos of the original wavelet, these echos can be removed by the Homomorphic Deconvolution technique. Such wavelet mixing is a frequent occurrence on seismograms. For completeness, however, a comparison of the Maximum Likelihood and Homomorphic Deconvolution methods are made so that the relative differences between the two techniques can be evaluated, Table 6.1 is a tabulation of the examples given in this

chapter. From this table it can be seen that the Maximum Likelihood techniques generally tends to give a smaller estimate of t* than the Homomorphic Deconvolution technique. This result is expected, as previously discussed, when no pre-whitening is applied to the time series before MLM is computed. Furthermore, inspection of Table 6.1 reveals that the t* measurements obtained by both techniques are, in general, within one standard deviation of the mean from each other. The choice of which method to use to obtain the best results is not clear-cut. Since it is known that MLM results in a smaller t* than actually present and that the Homomorphic Deconvolution technique can be used to separate seismic wavelets, the latter will be used in the determination of the t* values, and these values will be presented in the next chapter.

TABLE 6.1

A Comparison Between t* Values Obtained Maximum Likelihood and Homomorphic Deconvolution Methods

	Maximum Likelihood		Homomorphic Deconvolution	
Event No.	t*	Standard Deviation	t*	Standard Deviation
3	0.462	0.063	0.518	0.099
15	0.297	0.052	0.374	0.052
24	0.434	0.066	0.388	0.041
32	0.210	0.056	0.307	0.041

CHAPTER 7

LEAST SQUARES FITTING PROCEDURE FOR THE EVALUATION OF t* VALUES AND Q MODELS

7.1 Introduction

Thus far, the methods of determining t* values from power spectral estimates have been discussed. The least squares procedure used in this research is outlined in Subsection 7.1.1 along with a means of estimating the standard deviation of the mean. Subsection 7.1.2 demonstrates how t* estimates can be used to develop Q models for the mantle, using a comparison of the short period t* values with t* values calculated from free oscillation models. In order to construct a consistent Q model for both frequency bands, two Q models were considered, firstly a model of simple proportionality between the two frequency bands (Subsection 7.2.2), and secondly a model demonstrating the frequency dependence required to make the t* values between the two frequency bands consistent with one another (Subsection 7.2.3). The free oscillation model SL7 (Anderson and Hart, 1978) was used for this purpose. After making an estimate of the amount of frequency dependence from the two frequency bands, the consequences and implications of the results were considered. These include Q_α to Q_β ratios, bulk Q (Q_K), the Q's of ScP and ScS phases, and phase velocity relationships. Since the only free oscillation model used up to this point was SL7, the last section of this chapter examines t* values calculated from other free oscillation models. In this way some judgement can be made as to which free oscillation Q model best satisfies the short period data.

7.1.1 t* Approximation by Least Squares

As outlined in the previous chapter, the spectra after the removal of instrument and source responses were fitted by a least squares method in order to determine the attenuation factor t*. A brief summary of the least squares procedure used is given to enable the reader to make comparisons between t* determined here and estimates obtained by other investigators.

Because the attenuation function is non-linear, either a least squares method for an arbitrary function must be applied or the attenuation function made linear to determine t* values (Bevington, 1969). Least-squares techniques for arbitrary functions are determined in parameter space by minimizing the reduced Chi-square (χ^2) with respect to each parameter simultaneously. However, because the attenuation factor t* is small (high Q), the corner frequency belonging to the source spectra is not expected to shift much from those determined from the power spectra. Therefore only the intercept value and the t* value need be estimated by the least-squares method. Upon removal of the source and instrument response and assuming that the crustal response, noise, etc. have been minimised by the spectral technique, the adjusted power spectrum can be made linear by taking the natural logarithm of both sides of Equation 3.3, i.e.

$$\mathrm{Ln}(P) = \mathrm{Ln}(P_o) - \omega t^* \qquad 7.1$$

or simply

$$P' = P_o' - \omega t^* \quad .$$

From this point, linear least squares regression techniques can be employed.

In order to fit the spectral data in the primed system, (Equation 7.1) it is necessary to adjust the standard deviation of the measured power in the unprimed system, so that small errors in the smaller power values do not

over emphasize the fitting interval. To compensate for this trend, the standard deviation derived in Equation 5.5 must be modified by taking the derivative of the primed system (Bevington, 1969). Therefore using σ_i and σ_i' as the standard deviations of the unprimed and primed systems respectively, the standard deviation in the primed system becomes

$$\sigma_i' = \frac{d(\mathrm{Ln}P_i)}{dP_i}\sigma_i = \frac{\sigma_i}{P_i} \quad . \qquad 7.2$$

Substituting the standard deviation given by Equation 5.5 into the above equation, the standard deviation in the primed system becomes

$$\sigma_i' = \frac{P_i / \sqrt{M}}{P_i} = \frac{1}{\sqrt{M}} \qquad 7.3$$

where again M is simply the number of channels in the stacked array.

At this point the attenuation part of the spectrum can be treated as a linear least-squares regression problem. The slope (t*) and the intercept value P_o can then be estimated. However, the standard deviation of slope and intercept will still be in the primed system, which must be evaluated in terms of the unprimed system. These standard deviations can be calculated in a similar manner to Equation 7.2; thus

$$\sigma'_{P_o} = \frac{d(\mathrm{Ln}P_o)}{dP_o}\sigma_o = \frac{\sigma_o}{P_o}$$

and $\qquad 7.4$

$$\sigma'_{t^*} = \frac{dt^*}{dt^*}\sigma_{t^*} = \sigma_{t^*} \quad .$$

Therefore the standard deviation for the unprimed system becomes

simply

$$\sigma_{P_o} = P_o \, \sigma'_{P_o}$$

and

$$\sigma_{t^*} = \sigma'_{t^*} \quad . \tag{7.5}$$

Examples of fitting by this procedure have already been demonstrated in Figures 6.7, 6.8, 6.9, 6.10, 6.13, 6.14, 6.15 and 6.16 in the previous chapter. In those figures, the displacement source response was replaced into the power spectrum (solid line) after the least-squares fit was made, and also into the fitting estimate (dashed line). Note the small curvature of the fitting line caused by the source response. This further demonstrates that the perturbation from the source function is small compared to the response due to attenuation. Using the above least-squares fitting procedure and the spectral techniques of the previous chapter, t* was determined for the P, S, PcP, ScP phases listed in Tables 2.2 and 2.3 and these are given in Tables 7.1 through 7.3. The intercept values are not given in these tables because they are of little interest, since they relate to the relative earthquake magnitudes and assumed frequency-independent reflection coefficients. However, the slownesses are included in these tables because of their importance to Q model determinations by ray tracing. The next section will discuss the methods used to obtain a Q model, making use of the parameters listed in the above tables.

7.1.2 Methods of Determining a Q Model Using Short Period t* Data

Direct inversion of the t* values given in Tables 7.1 through 7.3 is not possible because of the large variation between the individual estimates. Even with a larger data set these variations would lead to unacceptable Q variations as a function of depth or distance. Variations of the slowness

Table 7.1

t* Estimates and other Parameters for the P phase listed in Table 2.3

Event No.	Earthquake depth (Km)	Experimental t* (t^{*E})	Standard deviation	Slowness $dt/d\Delta$	Mid-frequency (Hz)
19	21.0	0.504255	0.045122	10.1	2.0625
33	49.0	0.309568	0.047339	8.0	2.2262
28	87.0	0.415544	0.042651	7.3	2.0726
9	118.0	0.333495	0.033891	7.9	2.0203
26	128.0	0.292967	0.050899	9.7	2.2500
29	184.0	0.327598	0.058580	8.0	2.2763
22	190.0	0.517525	0.103872	8.6	1.3080
15	193.0	0.374027	0.051827	7.9	2.1774
6	199.0	0.207212	0.044313	9.3	2.1317
25	254.0	0.336285	0.046317	9.7	2.1071
20	291.0	0.268660	0.048891	8.1	2.1246
31	309.0	0.298332	0.056589	8.0	2.3750
18	380.0	0.283126	0.147486	8.1	1.8056
24	405.0	0.387717	0.040889	7.5	1.7030
32	457.0	0.231542	0.056488	9.0	2.2262
12	486.0	0.279109	0.029276	7.9	2.3750
10	489.0	0.301720	0.036668	7.9	2.1246
1	491.0	0.287148	0.037630	7.9	2.1200
23	505.0	0.231943	0.039433	7.5	2.0276
13	548.0	0.387990	0.039307	7.8	1.9881
7	551.0	0.378585	0.038066	8.0	1.9951
4	556.0	0.369502	0.042428	8.0	2.1020
34	599.0	0.307232	0.040538	7.7	2.1346
11	619.0	0.211618	0.040461	7.9	2.0530
† 21	67.0	0.543483	0.042149	2.1	1.8000
† 28	87.0	0.308932	0.035945	3.6	2.1667
† 29	184.0	0.584120	0.064747	3.3	1.4667
† 22	190.0	0.314123	0.036464	2.7	2.2500
† 24	405.0	0.528550	0.076939	3.6	1.7150

† Denote PcP t* values.

Table 7.2

t* Estimates and other Parameters for the S phase listed in Table 2.3

Event No.	Earthquake depth (Km)	Experimental t* (t^{*E})	Standard deviation	Slowness dt/dΔ	Mid-frequency (Hz)
19	21.0	1.589342	0.526330	15.25	0.8403
33	49.0	1.491434	0.322310	15.05	0.8523
28	87.0	0.886867	0.100048	13.9	1.1852
9	118.0	1.012252	0.177512	15.3	0.8852
26	128.0	1.011513	0.190172	17.4	1.0000
8	174.0	0.805721	0.095261	17.9	1.2184
15	193.0	1.173503	0.586307	15.4	1.0417
6	199.0	0.674110	0.147128	17.4	1.6250
25	254.0	0.709526	0.335466	14.15	0.8814
20	291.0	1.032204	0.097358	14.6	1.2000
31	309.0	1.322535	0.177516	14.55	0.8667
18	380.0	0.791570	0.154091	14.4	0.9798
24	405.0	0.943249	0.370780	13.5	0.7898
32	457.0	0.648858	0.237958	15.7	1.2454
12	486.0	1.129739	0.291745	14.4	0.9833
10	489.0	1.156290	0.230811	14.4	0.8814
1	491.0	0.899270	0.115726	14.4	1.2948
23	505.0	0.789395	0.200108	13.6	1.3296
4	526.0	0.789086	0.312251	14.6	0.9028
13	548.0	0.351320	0.047551	14.1	2.1667
7	551.0	1.154149	0.149355	14.4	1.3333
4	556.0	0.750327	0.128156	14.4	1.2278
16	563.0	0.472646	0.165795	14.25	1.6250
34	599.0	0.778556	0.160566	14.05	1.1278
11	619.0	0.646994	0.088684	14.2	1.4625

Table 7.3

t* Estimates and other Parameters for the ScP phase listed in Table 2.3

Event No.	Earthquake depth (Km)	Experimental t* (t^{*E})	Standard deviation	Slowness dt/dΔ	Mid-frequency (Hz)
19	21.0	0.515045	0.045331	2.4	1.9073
33	49.0	0.947318	0.145742	4.1	0.9977
27	52.0	0.651411	0.092237	3.9	1.3750
21	67.0	1.763864	0.495068	2.8	0.7500
28	87.0	0.321741	0.047729	4.2	2.2819
9	118.0	0.810995	0.111153	2.9	1.0500
26	128.0	0.703538	0.138896	2.6	1.3333
17	174.0	0.337299	0.062109	2.8	1.7917
29	184.0	0.522687	0.076328	4.0	1.6875
15	193.0	0.732610	0.100093	3.3	1.3257
6	199.0	0.289196	0.041652	2.9	2.1204
25	254.0	0.372902	0.057263	2.8	1.9329
17	273.0	1.653767	0.359954	3.5	0.7625
20	291.0	0.582009	0.092584	4.0	1.3750
31	309.0	1.243477	0.340632	4.0	0.7708
18	380.0	0.352200	0.049394	4.0	1.9137
24	405.0	0.345236	0.054399	4.2	2.0795
30	456.0	0.388630	0.046949	4.0	2.0726
32	457.0	0.558518	0.082837	2.8	1.6083
12	486.0	0.549954	0.049338	4.0	1.6022
10	489.0	0.758825	0.181495	4.0	1.0441
1	491.0	0.868583	0.065665	4.0	1.5007
23	505.0	0.812580	0.185642	4.2	1.0528
4	526.0	0.711875	0.107161	4.0	1.2632
13	548.0	0.186453	0.044266	4.1	2.1071
7	551.0	0.571331	0.050289	4.0	1.6674
4	556.0	1.033895	0.131079	4.0	1.1500
16	563.0	0.558582	0.083014	4.0	1.4583
2	583.0	0.842708	0.169251	4.0	1.0528
34	599.0	1.053978	0.288605	4.1	0.8750
11	619.0	0.373230	0.052760	4.0	2.1250

parameter and depth make an averaging of t* values impractical. In other words, it would be difficult to obtain sufficient data with similar slownesses and depths for the purpose of averaging t* values.

An alternative to a direct t* inversion is to assume a Q model constructed by other authors using free oscillation and surface wave data (Anderson and Hart, 1978a,b; Sailor and Dziewonski, 1978). A functional relationship might then be expected to exist between short period t*'s and t*'s determined from free oscillation and surface wave Q models. Such a relationship may or may not be a function of frequency. This function at the present time will be simply termed $f(\omega)$. With this function $f(\omega)$, an equation can be written for a Q model having $j = 1, \ldots, N$ layers

$$t^{*E} = f(\omega) \sum_{j=1}^{N} t_j^{*M} \qquad 7.6$$

where t^{*E} is the experimentally determined t* of this study and $\sum_{j=1}^{N} t_j^{*M}$ is the total t* value calculated from a free oscillation Q model for a given ray path. The factors controlling the t^{*M} in the above equation are the slowness, the depth of the event and the velocity model used to determine the travel times. In this case all layers through which the ray path does not pass will have zero contribution to the t^{*M} value. If Equation 7.6 is applied to each of the experimental t* determinations, an estimate for the parameters in $f(\omega)$ can be determined in a least-squares sense. Methods for least-squares fitting to an arbitrary function are available for the purpose of determining $f(\omega)$ in terms of the experimental t* values and the t* values calculated from a Q model (Bevington, 1969). The least squares method described here finds the optimum values of the parameters a_j contained in the function $f(\omega)$ by minimising the reduced χ^2 with respect to each of the parameters simultaneously

$$\frac{\partial \chi^2}{\partial a_j} = \frac{\partial}{\partial a_j} \sum \frac{1}{\sigma_i^2} [y_i - y(x_i)]^2 = 0 \quad . \qquad 7.7$$

Here $y_i = f(\omega)t^{*E}$, $y(x_i) = f(\omega)t^{*M}$ and σ_i^2 is the variance of the measured t* values. In general the analytical expression for derivative of the function with respect to the parameters a_j are not easily determined. It is therefore necessary to search for the minimum reduced χ^2 for the n parameters a_j on an n-dimensional hypersurface to find the appropriate minimum values of the reduced χ^2. However, the use of a non-analytical derivative can result in the occurrence of local minima on the hypersurface which may not be the absolute minimum of the function being determined. In the next two sections the analytical derivatives of the function $f(\omega)$ will be used to reduce the possibility of local minima on the hypersurface, thereby obtaining the best estimate of the values of the parameters a_j contained in $f(\omega)$.

Four least squares techniques for an arbitrary function are described in the book by Bevington (1969). Of these methods, the most commonly used technique is a gradient-expansion algorithm which takes advantage of the best features of the other three methods. Fewer iterations are necessary to determine the parameter a_j by the gradient-expansion method.

7.2 Q Models for the Mantle

7.2.1 Preliminary Parameters

In order to compare the experimental t* values given in Tables 7.1 through 7.3 using the least-squares procedure described in the previous section, Q and velocity models for P and S seismic phases must be

incorporated. Firstly, the velocity model chosen for this purpose is the Parametric Earth Model (PEM) given by Dziewonski, Hales and Lapwood (1975). The resulting travel time error introduced by this velocity model is considered to be much smaller than the error incurred with available Q data. Therefore it is unnecessary to seek a velocity model which may result in a reduction of the travel time error. Secondly, the Q model chosen for comparison with the experimental t* values of this work is Anderson's SL7 Q model (Anderson and Hart, 1978b). The choice of this Q model was completely arbitrary and results obtained are compared with those from other models later in the chapter. Both the Q and velocity models just discussed for longitudinal and shear waves are given in Table 7.4.

7.2.2 Functional Relationships of P and S Phases (Q Model 1)

For the first model, Q Model 1, the frequency dependence of Q is not specifically considered. That is, the t* values derived from the free oscillation Q model (SL7) are assumed to have a simple proportionality to the values of t* estimated in the short period range. Therefore, making use of Equation 7.6,

$$f(\omega) = \frac{1}{A} \qquad 7.8$$

where A is a constant of proportionality between the free oscillation and short period t* estimates.

Table 7.5 and 7.6 are the results of the least-squares fit using the fit function just described for P and S phases respectively.

Examination of these tables indicate that for P and PcP the t* values obtained here must be 2.44 ± 0.01 times greater than the t* values obtained from the SL7 model. Furthermore, the t* values obtained for SL7 model

Table 7.4

Quality Factors and Velocity Models

+ Velocity model after Dziewonsky et al., (1975)
++ Q model SL7 after Anderson and Hart, (1978)

Depth (Km)	Velocities+		Quality Factors++	
	V_α	V_β	Q_α	Q_β
0.0	5.8	3.45	1242.22	500.0
5.5	6.5	3.75	1244.11	500.0
11.0	6.5	3.75	1047.31	500.0
45.20	8.02	4.69	240.20	110.0
79.37	8.02	4.69	207.14	90.0
113.53	8.02	4.69	218.50	90.0
147.70	7.84750	4.4586	265.92	105.0
181.86	7.84750	4.4586	273.85	105.0
250.19	8.34835	4.4732	282.06	105.0
318.52	8.59017	4.6005	280.41	105.0
352.68	8.71100	4.6641	277.89	105.0
386.84	8.83184	4.7277	275.19	105.0
421.00	9.55633	5.05333	285.61	110.0
462.69	9.63691	5.12333	515.20	200.0
504.35	9.71743	5.19328	511.56	200.0
546.02	9.79798	5.26325	507.94	200.0
587.68	9.87850	5.33320	504.18	200.0
629.34	9.95902	5.40315	499.63	200.0
671.00	10.92971	6.11522	578.62	235.0
757.07	11.07309	6.18223	680.00	280.0
843.99	11.21443	6.24727	771.19	320.0
930.91	11.35237	6.30974	852.04	355.0
1017.84	11.48702	6.36975	925.11	385.0
1104.76	11.61839	6.42739	931.93	385.0
1191.68	11.74666	6.48274	941.71	385.0
1278.60	11.87183	6.53592	951.49	385.0
1365.52	11.99401	6.58701	959.93	385.0
1452.45	12.11330	6.63612	967.10	385.0
1539.37	12.22974	6.68333	973.45	385.0
1626.29	12.34343	6.72873	979.08	385.0
1713.21	12.45446	6.77244	983.57	385.0
1800.13	12.56289	6.81453	1326.86	518.0
1887.06	12.66892	6.85512	1362.99	532.0
1973.98	12.77235	6.89428	1397.09	546.0
2060.90	12.87351	6.93212	1432.49	560.0
2147.82	12.97241	6.96873	1456.86	568.0
2234.74	13.06912	7.00421	1486.98	576.0
2321.67	13.16375	7.03866	1522.30	584.0
2408.59	13.25634	7.07216	1560.92	592.0
2495.52	13.34701	7.10431	1599.26	600.0
2582.45	13.42297	7.13672	1633.42	608.0
2669.38	13.52283	7.16797	1661.64	616.0
2758.30	13.60815	7.19866	1079.53	400.0
2843.24	13.69187	7.22889	268.99	100.0
2885.0	13.732	7.22889	268.99	100.0

Table 7.5

The Least Squares Fit for the Proportionality Constant A (Q Model 1) using Free Oscillation Model SL7 (Anderson and Hart, 1978)

P Phase

$\chi^2 = 3.361741$

Earthquake depth (Km)	t^{*E} (sec)	Standard deviation	$t^{*M}/f(\omega)$ (sec)	$t^{*E} - t^{*M}/f(\omega)$ (sec)
21.0	0.504255	0.045122	0.428245	0.076010
49.0	0.309568	0.047339	0.407118	-0.097550
87.0	0.415544	0.042651	0.411669	0.003875
118.0	0.333495	0.033891	0.389431	-0.055936
128.0	0.292967	0.050899	0.325971	-0.033004
184.0	0.327598	0.058580	0.369652	-0.042054
190.0	0.517525	0.103872	0.359602	0.157923
193.0	0.374027	0.051827	0.371396	0.002631
199.0	0.207212	0.044313	0.282665	-0.075453
254.0	0.336285	0.046317	0.286860	0.049425
291.0	0.268660	0.048891	0.352725	-0.084065
309.0	0.298332	0.056589	0.353881	-0.055549
380.0	0.283126	0.147486	0.329671	-0.046545
405.0	0.387717	0.040889	0.335280	0.052437
457.0	0.231542	0.056488	0.261875	-0.030333
486.0	0.279109	0.029276	0.208567	-0.029458
489.0	0.301720	0.036668	0.308567	-0.006847
491.0	0.287148	0.037630	0.308567	-0.021419
505.0	0.231943	0.039433	0.314403	-0.082460
548.0	0.387990	0.039307	0.301007	0.086983
556.0	0.369502	0.042428	0.295701	0.073801
599.0	0.307232	0.040538	0.298649	0.008583
619.0	0.211618	0.040461	0.292913	-0.081295
67.0	0.543483	0.042149	0.339759	0.203724
87.0	0.308932	0.035945	0.359918	-0.050986
184.0	0.584120	0.064747	0.328074	0.256046
190.0	0.314123	0.036464	0.316691	-0.002568
405.0	0.528550	0.076939	0.298452	0.230098

$A = 2.443378 \pm 0.006068$

$f(\omega)$ is defined by Equation 7.8 in text.

Table 7.6

The Least Squares Fit for the Proportionality Constant A (Q Model 1) using Free Oscillation Model SL7 (Anderson and Hart, 1978)

S Phase

χ^2 = 1.464982

Earthquake depth (Km)	t^{*E} (sec)	Standard deviation	$t^{*M}/f(\omega)$ (sec)	$t^{*E} - t^{*M}/f(\omega)$ (sec)
21.0	1.589342	0.526330	1.072518	0.516824
49.0	1.491434	0.322310	1.080393	0.411041
67.0	0.914603	0.134049	0.912981	0.000622
87.0	0.885225	0.101930	1.080400	-0.195175
118.0	1.012252	0.177512	1.017786	-0.005534
128.0	1.240804	0.167715	0.850253	0.390551
174.0	0.805721	0.095261	0.850785	-0.045064
193.0	1.173503	0.586307	0.964058	0.209445
199.0	0.674119	0.147128	0.778852	-0.104742
254.0	0.709526	0.335466	0.967606	-0.258080
291.0	1.032204	0.097358	0.951420	0.080784
309.0	1.322535	0.177516	0.952497	0.370038
380.0	0.763378	0.175118	0.887707	-0.124329
405.0	0.943249	0.370780	0.913863	0.029386
458.0	0.648858	0.237958	0.771316	-0.122458
486.0	1.129739	0.291745	0.821933	0.307806
489.0	1.156290	0.230811	0.821933	0.334357
491.0	0.899270	0.115726	0.821933	0.077337
505.0	0.789395	0.200108	0.849499	-0.060104
526.0	0.789086	0.312251	0.800573	-0.011487
551.0	1.154149	0.149355	0.793556	0.360593
556.0	0.750327	0.128156	0.793556	-0.043229
563.0	0.472646	0.165795	0.801162	-0.328516
599.0	0.778556	0.160566	0.797490	-0.018934
619.0	0.646994	0.088684	0.789639	-0.142645

A = 4.140477 ± 0.145615

$f(\omega)$ is defined by Equation 7.8 in text.

S phases must be 4.14 ± 0.15 greater than in this work. Therefore, assuming that SL7 model is approximately correct for free oscillation data, the Q's at the short periods are much higher; (2.44 times for P phase Q's and 4.14 times for S phase Q's). Hence the conclusion must be reached that Q is frequency dependent, as will be explored in the next section.

7.2.3 Frequency-Dependent Functional Relationship of Q_α and Q_β (Q Model 2)

If t* estimates of this study are plotted against the mid-frequencies of the spectral estimates for t* they indicate an asymptotic trend, or equivalently a linear trend in Q (Figures 7.1 through 7.3). This trend is consistent in all these figures: a decrease of the t* estimate with frequency, implying an increase of Q with frequency. Furthermore, the effect of the frequency dependence is a first order effect, whereas the effects of distance and depth of the ray path are only second order.

A survey of the literature supports the conclusion here that Q is frequency dependent. Yoshida and Tsujiura (1975) found shear Q's for the upper 600 km of the earth of 150, 220 and 260 for the frequency ranges 0.015-0.035, 0.035-0.095 and 0.30-0.80 Hz, which demonstrates an increase in Q with increasing frequency. Archambeau et al., (1969) also suggest an increase in Q with increase in frequency from observations of the differential attenuation of P phases from the Shoal explosion in two frequency bands 0.75-1.0 Hz and 1.0-1.5 Hz. In the course of their travel time studies, they developed a Q model to explain the observed amplitudes of the P phases. However, little or no attention was given to the actual frequency dependence. Sipkin and Jordan (1979) determined the Q for ScS (Q_{ScS}) phase as being 156 ± 13 for the frequency range of 0.006-0.07 Hz. They also found that Q_{ScS} increased with frequency for these seismic phases. For the frequency

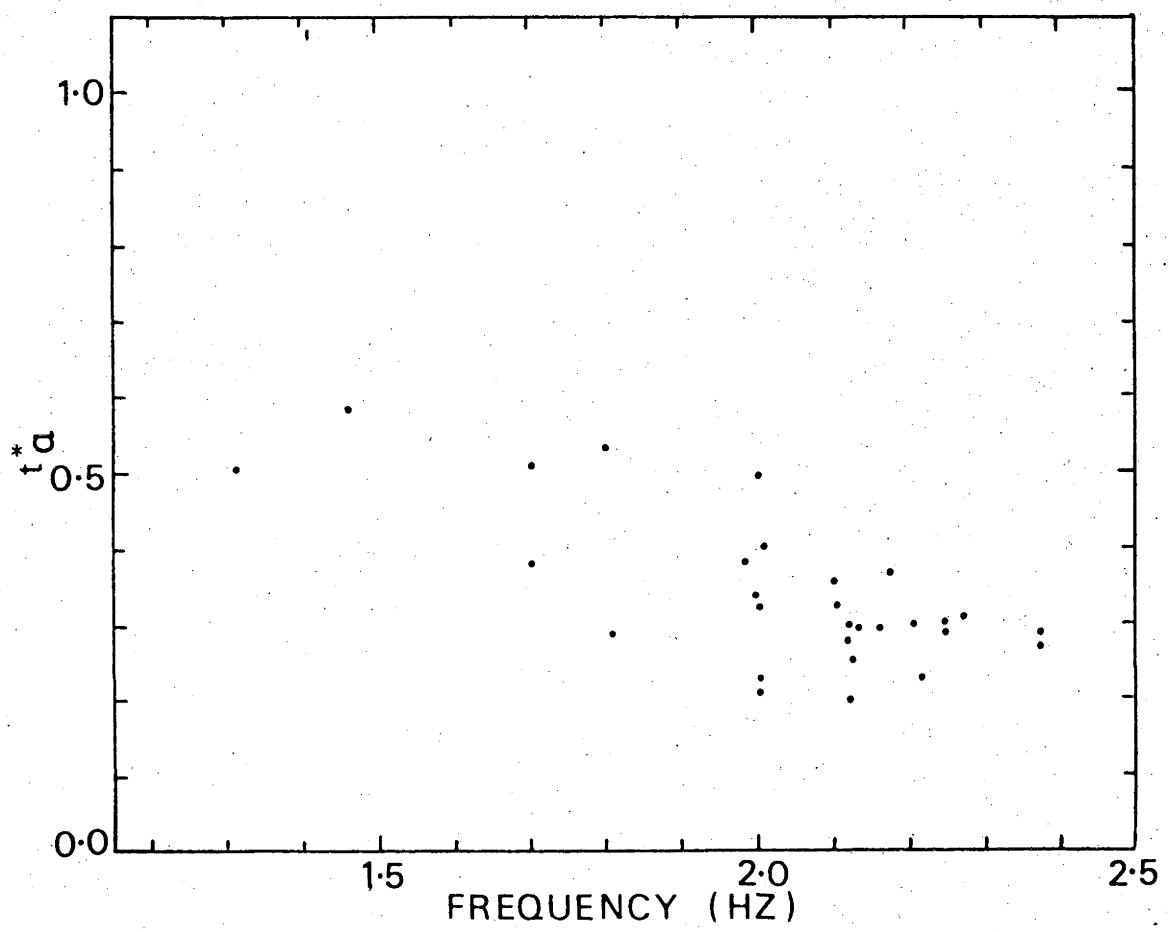

Figure 7.1 Illustration of the correlation between the t^*_α and the mid-frequency of the spectral fitting interval. Standard deviations of the mean for these t* values are given in Table 7.1.

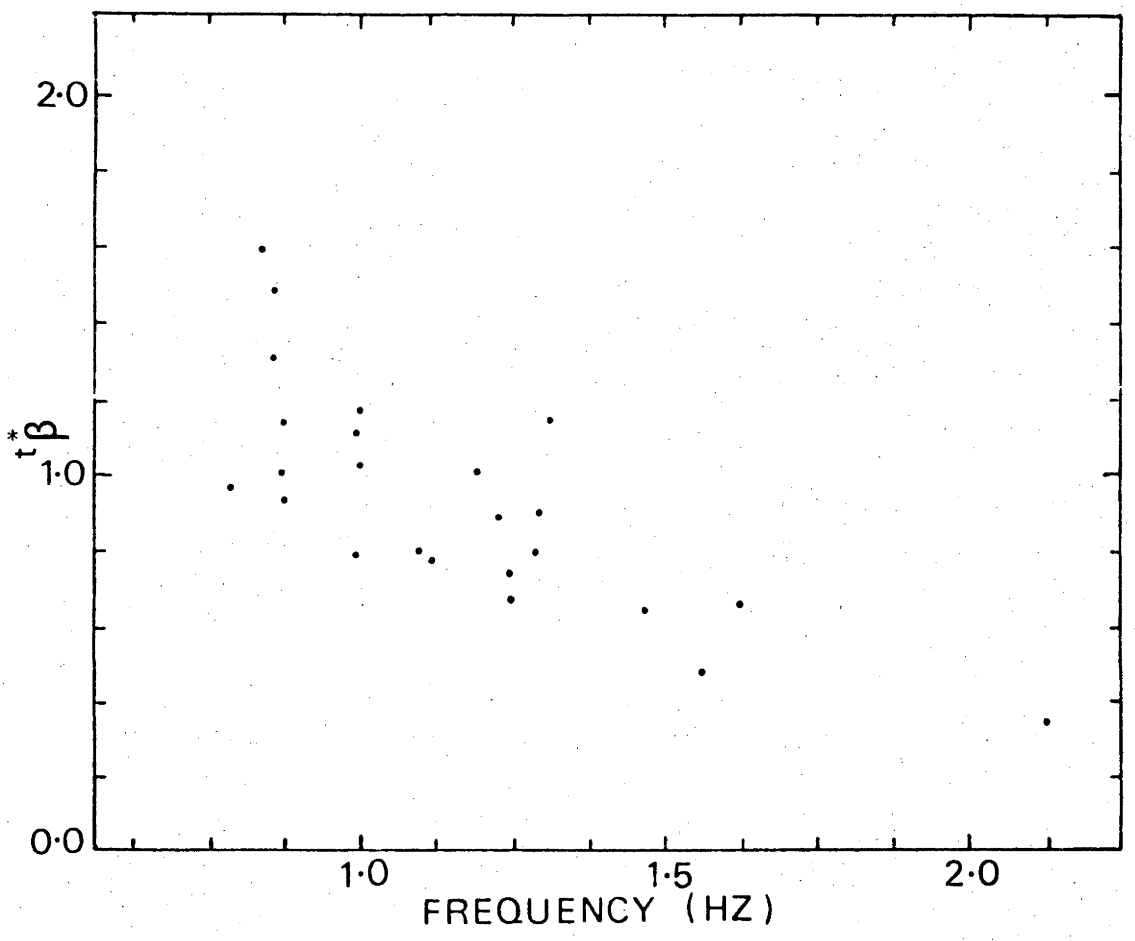

Figure 7.2 Illustration of the correlation between the t^*_β and the mid-frequency of the spectral fitting interval. Standard deviations of the mean for these t* values are given in Table 7.2.

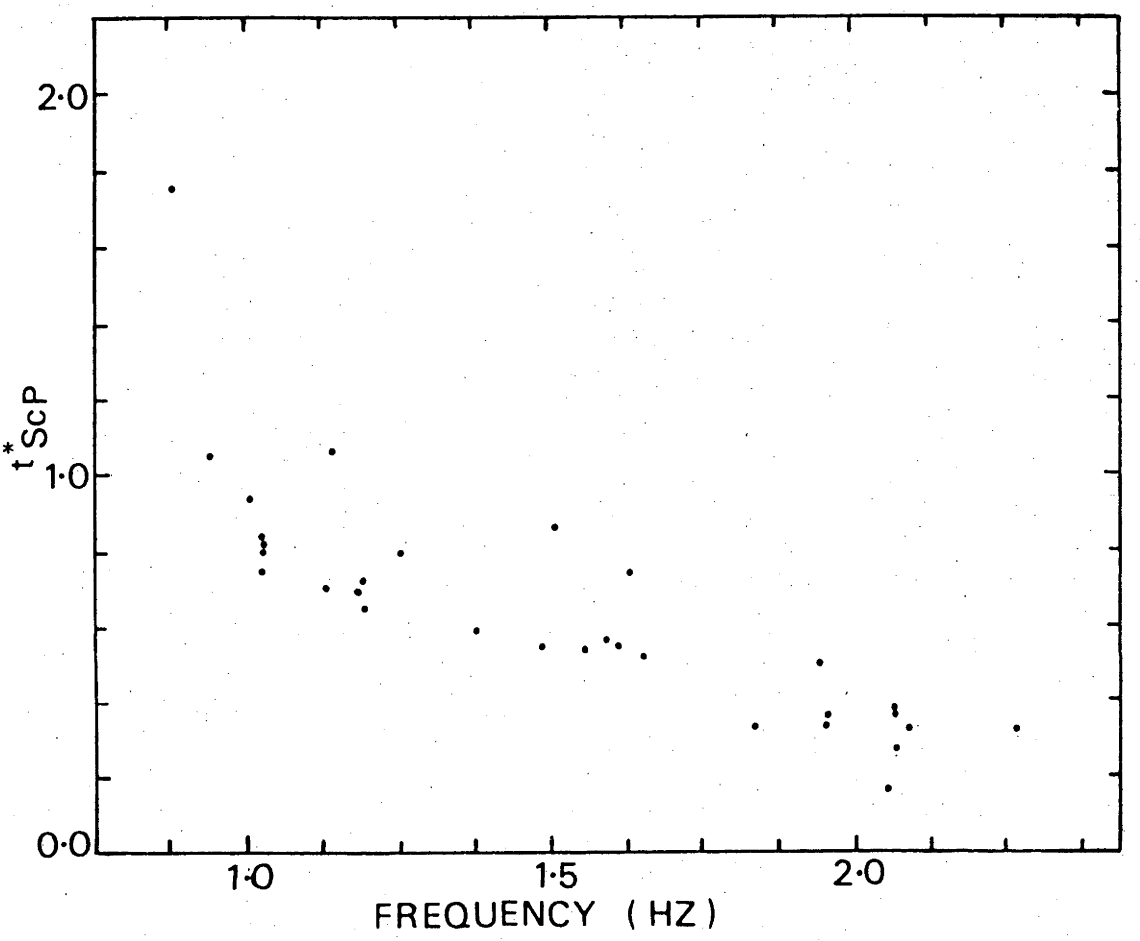

Figure 7.3 Illustration of the correlation between the t^*_{ScP} and the mid-frequency of the spectral fitting interval. Standard deviations of the mean for these t* values are given in Table 7.3.

range of 1.0-2.5 Hz they get a Q_{ScS} of between 400 and 750 depending upon the choice of corner frequency. However, it is clear that an increase of Q with frequency is present. Further evidence for high Q_α values (small t* values) measured in the short period range are given by Der and McElfresh, (1977).

The exact relationship between Q and frequency is far from clear. Many phenomenological and mechanistic models have been proposed (Strick, 1967; Futterman, 1962; Jackson, 1969; Jackson and Anderson, 1970) which may or may not correspond to conditions in the earth's interior. Experimental evidence favouring one particular mechanism or group of mechanisms is not yet available. Even empirical relationships between Q and frequency have not been satisfactorily determined. Such empirical relationships could lead to insight into possible physical Q mechanisms operating in the earth. The derivation of an empirical relationship between Q and frequency will be the purpose of this section.

Making the assumption that the apparent Q (Q_{App}) for a given ray path can be expressed as a polynomial in terms of the angular frequency ω, the polynomial becomes

$$Q_{App} = \gamma_o + \gamma_1\omega + \gamma_2\omega^2 + \ldots + \gamma_n\omega^n \qquad 7.9$$

where the γ's are related to the sum of the relaxation times of the material through which the ray passes. In the above equation, as ω approaches zero, the initial value of Q approaches γ_o, i.e. $Q_o = \gamma_o$. The above equation can thus be rewritten as

$$Q_{App} = Q_o (1 + \tau_1\omega + \tau_2\omega^2 + \ldots + \tau_n\omega^n) \qquad 7.10$$

where

$$\tau_i = \frac{\gamma_i}{Q_o} \quad \text{for} \quad i = 1, 2, \ldots, n$$

It remains to decide how many terms to use in the above polynomial.

On the basis of the evidence presented in the beginning of this section, it is assumed that Q is linearly frequency dependent for the crust and mantle. Equation 7.10 then becomes

$$Q_{App} = Q_o(1 + \tau\omega) \quad . \qquad 7.11$$

In the solution of the wave equation the absorption coefficient $k(\omega)$ becomes

$$k(\omega) = \frac{\omega}{vQ_o(1 + \tau\omega)}$$

where v is the wave velocity. This absorption coefficient can be coupled with phase velocity satisfying the requirements of causality (Kalinin et al., 1967).

Bearing in mind the justification presented above for the use of Equation 7.11 as a reasonable Q function, a function $f(\omega)$ must be developed for the comparison between the experimental t^{*E} and the t^{*M} of Anderson's SL7 model. This relationship, to be used in Equation 7.6 forms the basis of Q Model 2, and is

$$f(\omega) = \frac{(1 + \tau\omega_A)}{(1 + \tau\omega)} \qquad 7.12$$

where ω_A is taken to be $2\pi/200$ radians/sec, the mid-frequency range for the free oscillation data. Also, ω in the mid-frequency range of the observed t^{*E} is as given in Tables 7.1 through 7.3.

Again applying the least squares technique of Section 7.1.2 using $f(\omega)$ given in Equation 7.12, then τ for the P phase (τ_α) and for the S phase (τ_β) are calculated to be 0.11 ± 0.005 and 0.46 ± 0.02 respectively. The P phase least-squares fit of t^{*E} for Q Model 1 (Table 7.5) compared with that of Q Model 2 (Table 7.7) indicates that the fitting function in

Table 7.7

The Least Squares Fit for τ_α (Q Model 2) using Free Oscillation Model SL7 (Anderson and Hart, 1978)

P Phase

χ^2 = 2.400248

Earthquake depth (Km)	t^{*E} (sec)	Standard deviation	$t^{*M}/f(\omega)$ (sec)	$t^{*E} - t^{*M}/f(\omega)$ (sec)
21.0	0.504255	0.045122	0.432473	0.071782
49.0	0.309568	0.047339	0.392803	-0.083235
87.0	0.415544	0.042651	0.414542	0.001002
118.0	0.333495	0.033891	0.398066	-0.064571
128.0	0.292967	0.050899	0.312483	-0.019516
184.0	0.327598	0.058580	0.351852	-0.024254
190.0	0.517525	0.103872	0.462699	0.054826
193.0	0.374027	0.051827	0.363165	0.010862
199.0	0.207212	0.044313	0.279932	-0.072720
254.0	0.336285	0.046317	0.286052	0.050233
291.0	0.268660	0.048891	0.349033	-0.080373
309.0	0.298332	0.056589	0.328136	-0.029804
380.0	0.283126	0.147486	0.359242	-0.076116
405.0	0.387717	0.040889	0.377260	0.010457
457.0	0.231542	0.056488	0.252667	-0.021125
486.0	0.279109	0.029276	0.286118	-0.007009
489.0	0.301720	0.036668	0.306192	-0.004472
491.0	0.287148	0.037630	0.306587	-0.019439
505.0	0.231943	0.039433	0.320701	-0.088758
548.0	0.387990	0.039307	0.310568	0.077422
551.0	0.378585	0.038066	0.304472	0.074113
556.0	0.369502	0.042428	0.295295	0.074207
599.0	0.307232	0.040538	0.295521	0.011711
619.0	0.211618	0.040461	0.296609	-0.084991
+ 67.0	0.543483	0.042149	0.382338	0.161145
+ 87.0	0.308932	0.035945	0.368359	-0.059427
+ 184.0	0.584120	0.064747	0.415865	0.168255
+ 190.0	0.314123	0.036464	0.314743	-0.000620
+ 405.0	0.528550	0.076939	0.352123	0.176427

τ_α = 0.110182 ± 0.004555 (sec).

$f(\omega)$ is defined by Equation 7.12 in text.

+ Denotes PcP t* values.

the latter case is more appropriate. The difference between t^{*E} and t^{*M} is much smaller in Q Model 2 than in Q Model 1. The same comparison is made between the S phase Q Model 1 (Table 7.6) and S phase Q Model 2 (Table 7.8). In this case the frequency dependence is even more obvious. The differences between t^{*E} and t^{*M} are much smaller in Q Model 2 than in Q Model 1.

The frequency dependence of Q for the P and S phases is demonstrated pictorially in Figure 7.4. Note that the ordinate axis is in terms of $Q_{App}/Q_{o\beta}$ where $Q_{o\beta}$ is the apparent zero shear frequency Q for both P and S models. The reason is that $Q_{o\beta}$ varies with the ray path. Depth, distance, and possibly station corrections must be applied, which in turn are related to pressure, temperature, viscosity, elasticity, etc., before the Q_{App} at the desired frequency can be determined for each ray path. A further correction can also be applied to the SL7 model used for the comparison of the derived and observed t*s. Since it was assumed that the mid-angular frequency range for the SL7 model was $2\pi/200$ radian sec^{-1}, the apparent Q_o for each layer will cause a reduction of 3.0% and 1.4% for P and S phases respectively from those given in Table 7.4. Care must be exercised, however, in extending the Q model beyond the frequency range specified by the assumed free oscillation model and the short period t* estimates in this thesis.

7.2.3.1 The Relationship Between Q_α and Q_β

As mentioned in the previous section, a frequency dependence of Q has been suggested earlier by other investigators, based on the variation of the ratio of Q_α/Q_β with increasing frequency. Q Model 2 accounts for this discrepancy in Q_α/Q_β when Equation 7.11 for Q_α and Q_β is written in the form

Table 7.8

The Least Squares Fit for τ_β (Q Model 2) using Free Oscillation Model SL7 (Anderson and Hart, 1978)

S Phase

$\chi^2 = 1.314070$

Earthquake depth (Km)	t^{*E} (sec)	Standard deviation	$t^{*M}/f(\omega)$ (sec)	$t^{*E} - t^{*M}/f(\omega)$ (sec)
21.0	1.589342	0.526330	1.306630	0.282712
49.0	1.491434	0.322310	1.303024	0.188410
87.0	0.886867	0.100048	1.030734	-0.143867
118.0	1.012252	0.177512	1.194610	-0.182358
128.0	1.011513	0.190172	0.894676	0.116837
174.0	0.805721	0.095261	0.785529	0.020192
193.0	1.173503	0.586307	1.003702	0.169801
199.0	0.674110	0.147128	0.570558	0.103552
254.0	0.709526	0.335466	1.139226	-0.429700
291.0	1.032204	0.097358	0.888918	0.143286
309.0	1.322535	0.177516	1.135100	0.187435
380.0	0.791570	0.154091	0.971173	-0.179603
405.0	0.943249	0.370780	1.162946	-0.219697
457.0	0.648858	0.237958	0.700051	-0.051193
486.0	1.129739	0.291745	0.893387	0.236352
489.0	1.156290	0.230811	0.967725	0.188565
491.0	0.899270	0.115726	0.723494	0.175776
505.0	0.789395	0.200108	0.732225	0.057170
526.0	0.789086	0.312251	0.926387	-0.137301
548.0	0.351320	0.047551	0.464713	-0.113393
551.0	1.154149	0.149355	0.682475	0.471674
556.0	0.750327	0.128156	0.728305	0.022022
563.0	0.472646	0.165795	0.586902	-0.114256
599.0	0.778556	0.160566	0.781682	-0.003126
619.0	0.646994	0.088684	0.630517	0.016477

$\tau_\beta = 0.463692 \pm 0.015167$ (sec).

$f(\omega)$ is defined by Equation 7.12 in text.

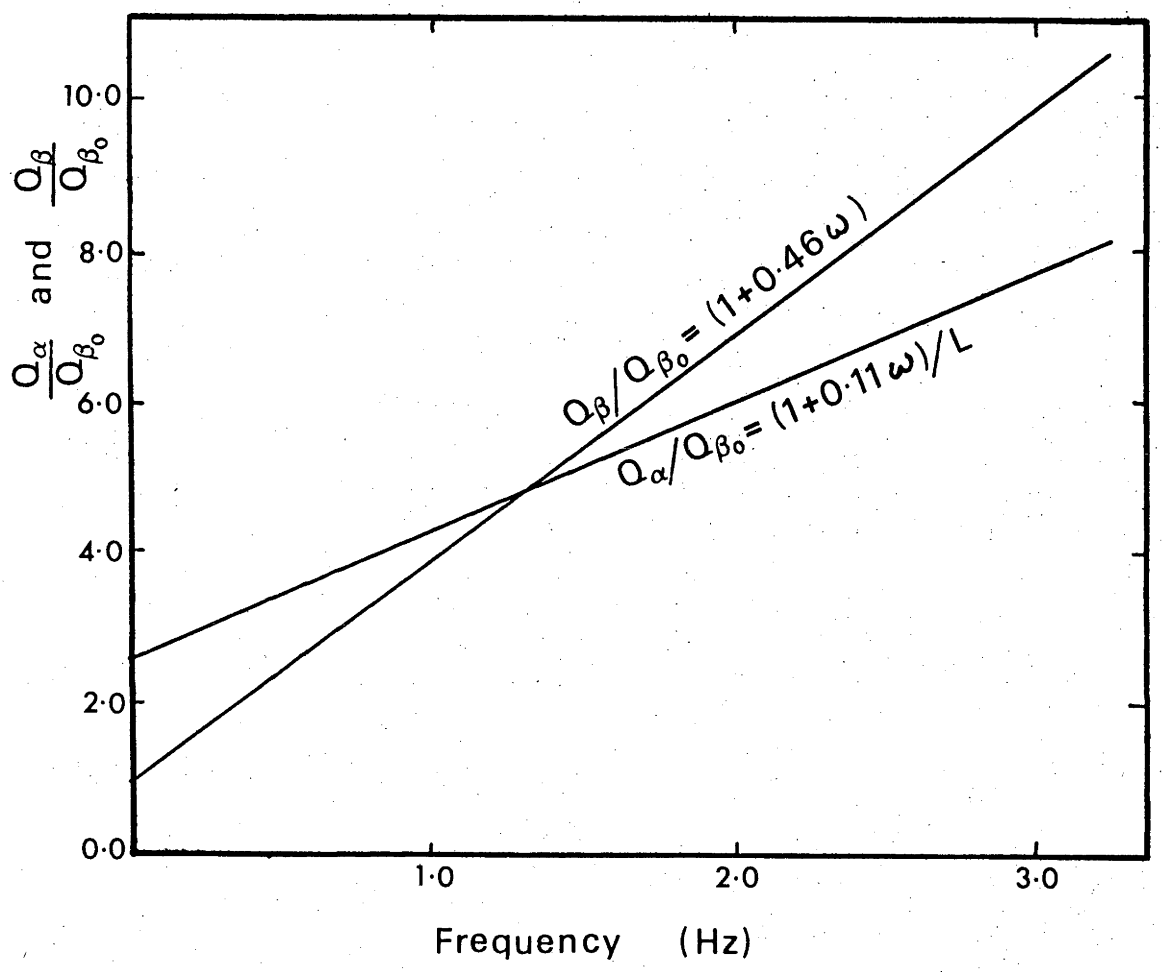

Figure 7.4 Illustration of the apparent trend of $Q_{App}/Q_{\beta o}$ for P and S seismic phases, as predicted from free oscillation and short-period body wave data.

$$\frac{Q_\alpha}{Q_\beta} = L^{-1} \frac{(1 + \tau_\alpha \omega)}{(1 + \tau_\beta \omega)} \qquad 7.13$$

where τ_α and τ_β are the respective constants for P and S phases as given in the previous section. L^{-1} is the Q_α to Q_β ratio at the apparent zero frequency where attenuation is assumed to occur in shear, therefore

$$L^{-1} = \left[\frac{Q_\alpha}{Q_\beta}\right]_{\omega=o} = \frac{3}{4} \left(\frac{\alpha}{\beta}\right)^2 \approx \frac{5}{2} \quad . \qquad 7.14$$

Equation 7.13 does indeed give a decrease in Q_α to Q_β ratio as the frequency increases. The expected values of Q_α/Q_β are presented in Figure 7.5. Another interesting feature of the above equation in that it predicts that the Q ratio is equal to 1 at a frequency corresponding to 1.29 Hz. At frequencies below this intersecting value

$$\frac{Q_\alpha}{Q_\beta} > 1 \quad \text{at } \omega < 2\pi(1.29)$$

and above the intersection, 7.15

$$\frac{Q_\alpha}{Q_\beta} < 1 \quad \text{at } \omega > 2\pi(1.29)$$

with a terminating value

$$\lim_{\omega \to \infty} \frac{Q_\alpha}{Q_\beta} = \frac{3}{4} \left(\frac{\alpha}{\beta}\right)^2 \left(\frac{1}{4}\right) \approx \frac{5}{8} \quad . \qquad 7.16$$

The decrease in Q_α/Q_β may occur when finite dissipation occurs due to bulk modulus relaxation due to intergranular thermoelastic effects (Anderson and Hart, 1978b).

So far little evidence has been obtained indicating Q_β higher than Q_α. The notable exception to this is given by Walker et al., (1978) and Sutton

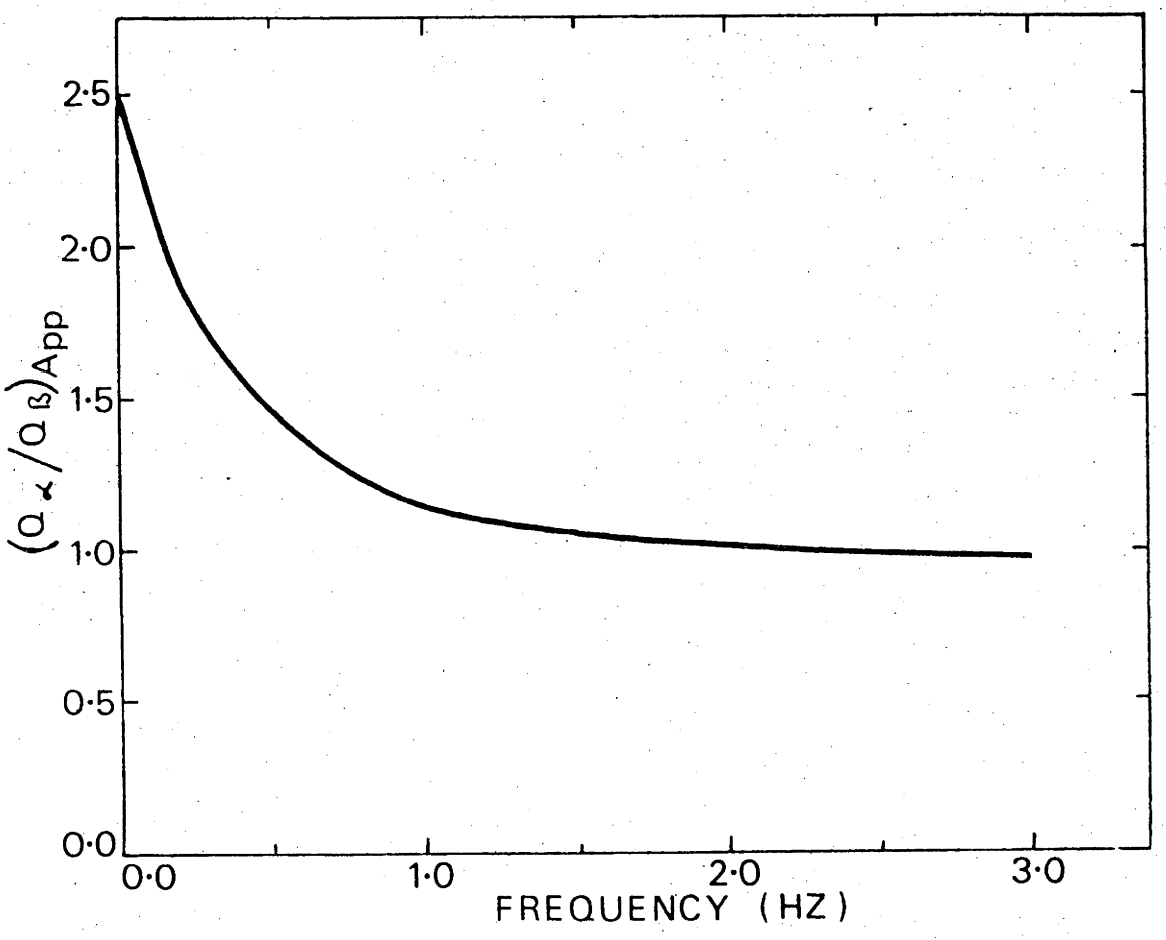

Figure 7.5 The predicted behaviour of Q_α/Q_β from Q Model 2.

et al., (1978). For P_n and S_n phases recorded on ocean bottom hydrophones, they have been reported apparent Q values as high as 8,400 ± 1,300 and 19,100 ± 3,700 respectively for the two phases. The frequency ranges for these Q measurements were also high, being 12 Hz for the P_n phases and 15 Hz for the S_n phase. If the hypothesis that these are waveguided close to the Mohorovičić discontinuity is correct (Walker, 1977a; Walker, 1977b) then, by making use of the formulation of the previous section, the apparent zero Q's for the P_n and S_n phases are 903 ± 144 and 427 ± 83 respectively. Furthermore, the initial P_n to S_n Q ratio would be 2.11 ± 0.53. These predicted values are not out of the realm of possibility, owing to the uncertainty in the Q measurements and free oscillation Q models.

The above implication can be tested in other regions of the seismic frequency band. As more Q ratios are obtained for other seismic frequency bands, further restriction may be imposed on Equation 7.11. Alteration of Equation 7.13 to a higher order polynomial may also be required. Such refinements will be the subject of future studies.

7.2.3.2 Implications for the Bulk Modulus Q (Q_K) in the Mantle

If it is accepted that the linear relationship given in Equation 7.11 is correct to a first order approximation, an equation for the frequency dependent bulk Q (Q_K) can be derived for mantle material. Making use of the equation (Anderson and Hart, 1978b)

$$Q_K = (1-L)\, Q_\beta / [Q_\beta/Q_\alpha - L] \qquad 7.17$$

where

$$Q_\beta = Q_\mu$$

the frequency dependence of Q_K can be determined. Substituting from Equation 7.11 into 7.17, the frequency dependence Q_K becomes

$$Q_K = (1 + 0.11\omega)(1 + 0.46\omega)\, Q_{\beta_o}/(0.23\omega) \quad . \qquad 7.18$$

From this equation,

$$\lim_{\omega \to 0} Q_K = \lim_{\omega \to \infty} Q_K = \infty$$

if the value of Q_K is accepted as a correct approximation to the actual bulk Q. The first derivative of the above equation with respect to frequency indicates a Q_K minimum at approximately 0.72 Hz, which means that the bulk Q is equal to the apparent Q_{β_o} at this frequency. The function tends to decrease rapidly from zero frequency to this minimum. In the free oscillation band, however, the bulk Q is still quite high. Q_K is approximately 150 times Q_{β_o} for mantle material. Q_K increases much more slowly from the minimum towards the higher frequencies than in the previous case. At a frequency of 1 Hz the increase in Q_K is only 4.5 Q_{β_o}.

The validity of the Q_K formulation given in Equation 7.18 awaits confirmation through appropriate laboratory experiments.

7.2.3.3 Frequency Dependent Functional Relation for ScP Phases (Q Model 2)

For the P and S phases, it was found that the best fits for the t* data in Tables 7.1 and 7.2 were obtained using the Q Model 2. In these two cases, however, the mantle is only sampled to a depth of approximately 1300 km. In order to sample more of the lower mantle the t* values for the ScP phase were used (Table 7.3). The application of this model is further encouraged by the apparent functional relationship of t^*_{ScP} to frequency (Figure 7.3).

The function used to compare the SL7 Q model given in Table 7.4 with the t* data of ScP phases (t^*_{ScP}) given in Table 7.3 is complicated by the need to consider the ray paths of the S and P phases separately. In this

case, the experimental t^{*E} can be compared with Q model through the following equation:

$$t^{*E}_{ScP} = f_s(\omega)\ t^{*M}_s + f_p(\omega)\ t^{*M}_p \qquad 7.19$$

where $f_s(\omega)$ and $f_p(\omega)$ are of the same form as Equation 7.12. To obtain t^{*M}_{ScP} it is necessary to solve for the relaxation time τ_β of the S wave from the source to the core-mantle boundary, and for the relaxation time τ_α of the P wave from the core-mantle boundary to the receiving station. By implication, if the values of τ_β and τ_α are the same as those given in Section 7.2.3, the models for the upper and lower mantle will be consistent.

Table 7.9 gives the results of the fit for the values of t^*_{ScP}. It is apparent that the numerical values for τ_β and τ_α are very close to those found for the S and P phases in Section 7.2.3. In the former case τ_β and τ_α are equal to 0.46 ± 0.015 and 0.11 ± 0.005 respectively, whereas in the latter they are equal to 0.41 ± 0.02 and 0.108 ± 0.009. The conclusion is therefore that the frequency dependent Q models for both the upper and lower mantle are consistent to first order.

For the fit the reduced χ^2 is much higher than those observed for P and S seismic phases. Scattering and frequency-dependent layering are the most probable causes for this deviation in the least squares fit, and the most likely place for this scatter in the data is in a region not sampled by the teleseismic P and S phases. The region of the earth in which this phenomenon occurs may be the core-mantle-boundary where scattering (Haddon and Cleary, 1974) and frequency-dependent layering (Mitchell and Helmberger, 1973) have both been postulated.

7.2.3.4 Phase Velocity Relationships from Q Model 2

In many aspects of seismology it is of interest to compute synthetic

Table 7.9

The Least Squares Fit for τ_β and τ_α (Q Model 2) using Free Oscillation Model SL7 (Anderson and Hart, 1978)

ScP Phase

χ^2 = 4.970832

Earthquake depth (Km)	t^{*E} (sec)	Standard deviation	$t^{*M}/f(\omega)$ (sec)	$t^{*E} - t^{*M}/f(\omega)$ (sec)
21.0	0.515045	0.045331	0.516799	-0.001754
49.0	0.947318	0.145742	0.853525	0.093793
52.0	0.651441	0.092237	0.684509	-0.033098
67.0	1.763864	0.495068	0.953362	0.810502
87.0	0.321741	0.047729	0.479594	-0.157853
118.0	0.810995	0.111153	0.742363	0.068632
128.0	0.703538	0.138896	0.631132	0.072406
174.0	0.337299	0.062109	0.502269	-0.164970
184.0	0.522687	0.076328	0.541060	-0.018373
193.0	0.732610	0.100093	0.612133	0.120477
199.0	0.289196	0.041652	0.434327	-0.145131
254.0	0.372902	0.057263	0.438767	-0.065865
273.0	1.653767	0.359954	0.812861	0.840906
291.0	0.582009	0.092584	0.589077	-0.007068
309.0	1.243477	0.340632	0.832667	0.410810
380.0	0.352200	0.049394	0.433726	-0.081526
405.0	0.345236	0.054399	0.407703	-0.062467
456.0	0.388630	0.046949	0.388089	0.000541
457.0	0.558518	0.082837	0.430859	0.127659
486.0	0.549954	0.049338	0.448036	0.101918
489.0	0.758825	0.181495	0.583213	0.175612
491.0	0.868583	0.065665	0.467508	0.401075
505.0	0.812580	0.185642	0.583495	0.229085
526.0	0.711875	0.107161	0.511222	0.200653
548.0	0.186453	0.044266	0.863345	-0.176892
551.0	0.571831	0.050289	0.420948	0.150383
556.0	1.033895	0.131079	0.530545	0.503350
563.0	0.558582	0.083014	0.458973	0.099609
583.0	0.842708	0.169251	0.558362	0.284346
599.0	1.053978	0.288605	0.612780	0.441198
619.0	0.373230	0.052760	0.350740	0.022490

τ_β = 0.417372 ± 0.019170 (sec).

τ_α = 0.108452 ± 0.008585 (sec).

$f(\omega)$ is defined by Equation 7.12 in text.

wavelets which represent those passing through the earth. This naturally involves a knowledge of the phase characteristics of the wavelets. Once the phase velocity is known the phase of the wavelets due to attenuation can easily be calculated. Assuming that Q Model 2 developed in this chapter is correct to first order, the phase velocity $v(\omega)$ modified from Kalinin et al. (1967) is

$$v(\omega) = \frac{v_\infty}{1 + [Q_o^{-1} \ln(\tau\omega)/\pi(\tau^2\omega^2 - 1)]} \qquad 7.20$$

where τ is the relaxation time for either P or S phases given by Q Model 2 and v_∞ is the velocity at infinite frequency.

Equation 7.20 implies an increase in phase velocity with an increase in the frequency of a seismic wavelet, or conversely a decrease in travel time with an increase in frequency. Therefore Equation 7.20 can be written in terms of the frequency dependent arrival time $t(\omega)$ for any frequency contained in a seismic wavelet, as

$$t(\omega) = t_\infty \left[1 + \frac{\ln(\tau\omega)}{Q_o\pi\ (\tau^2\omega^2 - 1)}\right] \qquad 7.21$$

where t_∞ is the predicted travel time at infinite frequency. Armed with the above equation and Equation 7.11 it may be possible to reduce much of the travel time residuals or baseline discrepancies once the apparent Q and high frequency cutoff point for a seismic wavelet under study are known.

The literature indicates the validity of the above paragraph. For example, when comparing travel times calculated from free oscillation velocity models with observed travel times of short period body wave data, the free oscillation velocity models predicts arrival times which are late. The free oscillation model C2, which is not corrected for phase velocity, has a baseline discrepancy of about 0.6 and 2-4 seconds when compared with

body wave solutions for P and S phases respectively (Anderson and Hart, 1976). On the other hand, when Hart et al., (1977) modelled the effect of attenuation in perturbating the free oscillation mode periods, a considerably smaller baseline discrepancy was produced. If Equations 7.21 and 7.11 provide the proper relationship between phase velocity and Q, an improved velocity and Q model for the mantle would result.

With the limited data on hand it is not possible to test Equation 7.21 completely. Also, it is not known by this author which free oscillation modes receive the most weight when determining the free oscillation velocity models. Therefore an average frequency cannot be chosen to demonstrate the absolute residual differences between short period and free oscillation velocity models. However, it is possible to show how the travel time varies with frequency for a given path by using one of the earthquakes as an example studied in this research. Table 7.10 demonstrates this travel time trend with frequency for both P and S phases using Event 19 in Table 2.2.

Further research is needed to ascertain whether the travel times given in Table 7.10 can properly account for earthquake residuals and baseline discrepancies. Knowing the high frequency cutoff point, one possibility is to perform a least-squares fit in a similar fashion to that done to derive Q Model 2 for the short period travel time data, and compare these values with the travel times calculated from free oscillations. Using the previously determined Q_o model and the values of τ for P and S phases, an average frequency for the free oscillation model can be determined. With these average frequency values for both P and S seismic phases, velocity and Q models for the mantle can be determined for any seismic frequency.

Table 7.10

Example Calculation for Event No. 19

Input Data:

Phase	P	S
Apparent t* (sec.)	0.504	1.59
Apparent travel time (sec.)	287.6	533.7
Apparent Q	570.35	335.8
Mid spectral Fequency (Hz)	2.0625	0.84028
High Frequency cutoff (Hz)	3.5	1.125

Output Data:

Apparent Zero Q_α (Equation 7.11)	235.15	160.61
Long period t* (sec.)	1.3	3.3

Travel time vs. Frequency and Period (Equation 7.21)

Frequency (Hz)	Period (sec.)	P Time (sec.)	S Time (sec.)
∞	0.0	287.53	533.50
3.5	0.29	287.60	533.52
3.0	0.33	287.62	533.53
2.0	0.5	287.67	533.56
1.0	1.0	287.81	533.66
0.5	2.0	288.00	533.88
0.1	10.0	288.57	534.97
0.05	20.0	288.84	535.63
0.025	40.0	289.11	536.34
0.01	100.0	289.47	537.30
0.005	200.0	289.74	538.03
0.0033	300.0	290.89	538.46
0.0025	400.0	290.01	538.76
0.002	500.0	290.09	539.00
0.001	1000.0	290.36	539.73
0.0	∞	∞	∞

Note: τ_α and τ_β are assumed to be 0.11 and 0.44 respectively for the above calculations.

7.2.3.4 Further Implications of Q Model 2

Up to this point Q Model 2 has been examined as to its implications concerning the bulk Q, Q_α/Q_β ratios, and the phase velocity for frequencies from zero to infinity. Such extrapolations are highly risky because the data are restricted to the range between the average free oscillation periods and the short period seismic bands. Different Q mechanisms can produce major changes to the predicted attenuation properties of the mantle outside this fitting interval. Predictions from a first-order model such as Q Model 2 must be tested when more data becomes available. Since Q_α/Q_β is assumed to be 2.5 for the SL7 Q model of Anderson et al., (1965), the point at which Q_β becomes greater than Q_α is predicted to be at a frequency about 1.29 Hz. However the P/S Q ratio at free oscillation periods may not be as large at 2.5. Since the long period Q_α's are not well known, a conservative estimate for this ratio at free oscillation periods, based upon a bulk Q of 4000 for the mantle Q_α/Q_β would be 2.0. This may shift the point at which $Q_\alpha/Q_\beta = 1$ to a higher frequency.

An important aspect of any model is, however, the accuracy of its predictions. Since Q values for the ScS phase have been given most attention in the literature, these data will be used to examine the ability of Q Model 2 to predict Q values for ScS phases. Figure 7.6 is a compilation of Q data for ScS phases after 1962, beyond which time one would expect the employment of computer techniques to produce a higher precision of measurement. It can be seen from the figure that the Q values at the various measured frequencies correspond quite favourably with the theoretical curve of Q Model 2. The conclusion therefore reached is that Q Model 2 is appropriate not only for the data described here but also for observations of Q for ScS phases obtained by other investigators.

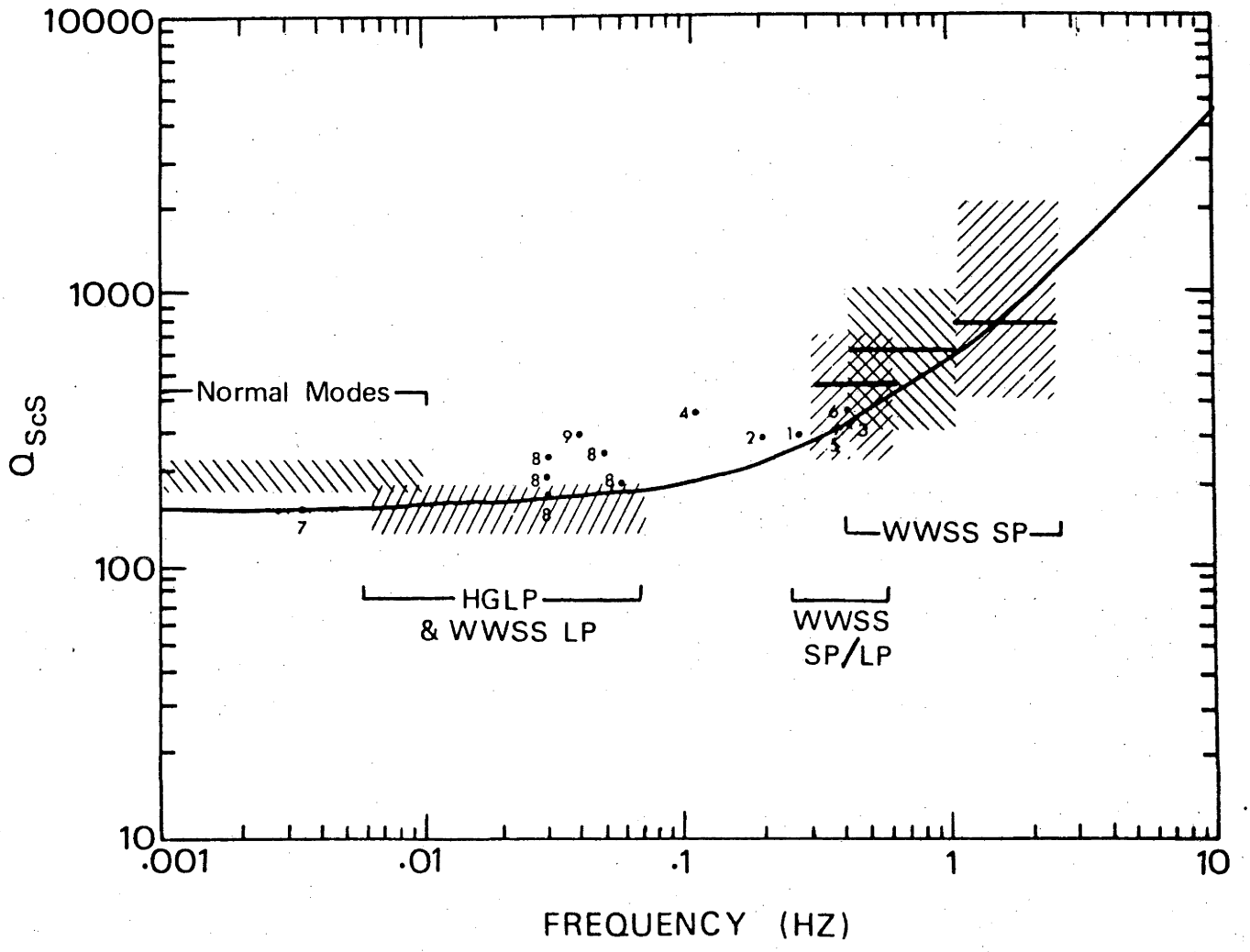

Figure 7.6 Computation of Q values for ScS phase. The figure is modified from Sipkin and Jordan (1979). The numbers dots correspond to the following determinations: 1 - Otsuka (1962); 2 - Otsuka (1963); 3 - Kanamori (1967a); 4 - Choudbury and Dorel (1973); 5 - Yoshida and Tsujiura (1975); 6 - Okal (unpublished data averaged 1976) taken from Anderson and Hart (1978a); 7 - Jordan and Sipkin (1977); 8 - Nakanishi (1979); 9 - Best et al., (1974).

7.3 Comparison of Other Free Oscillation Q Models with Short-period Teleseismic t* Estimates.

In the previous sections, it has been demonstrated how the free oscillation Q model SL7 and t* values obtained at short periods can be incorporated into a single Q model by assuming that Q is a linear function of frequency. Using the derived frequency-dependent Q model of Subsection 7.2.3, the implication for Q_α/Q_β, Q_K, phase velocity, and Q of ScS phase were considered (Subsections 7.2.3.1 through 7.2.3.5). The choice of the SL7 free oscillation Q model for this purpose was, however, to some extent arbitrary. In this section, other free oscillation Q models are examined, in order to determine how much variation in the constant τ_α and τ_β can occur. For this purpose, models SL1, SL2, (Anderson and Hart, 1978a) SL8, (Anderson and Hart, 1978b) QMU, GDQ, QML, QBS (Sailor and Dziewonski, 1978) and the Q_α model of Teng (Teng, 1967) were used. As in Subsection 7.2.3, the mid-period for these models was taken to be 200 seconds. The exception to this was the long-period Q_α model derived by Teng, because his mid-frequency range was known to be 10 seconds. In the case of the Sailor and Dziewonski, (1978) models, only the Q values for shear were given, therefore it was assumed that the initial Q_α values were 2.25 times greater than Q_β. The resulting values for τ_α and τ_β, along with their reduced χ^2 and standard deviations for the above mentioned Q models, are given in Table 7.11. Note that the statistical scatter range for both τ_α and τ_β is only approximately 0.1 sec. This statistical scatter is small considering the wide variations in the various Q models used for comparison with short period t* data. Some judgement as to which Q model is the best may perhaps be provided by comparison of the reduced χ^2 values obtained. If, however, it is assumed that the standard deviation represents a measure of goodness of fit for the various free oscillation models the weighted mean and standard deviation values for τ_α and τ_β can be calculated. These values are also given in Table 7.11.

Table 7.11

The Least Squares fit for τ_α and τ_β Obtained from Other Free Oscillation Q Models (cf. Tables 7.7 and 7.8).

P Phase

Q Model	Reduced χ^2	τ_α (sec)	Standard Deviation
SL1	3.208984	0.096598	0.001282
SL2	2.959040	0.113912	0.000470
SL7	2.400248	0.110182	0.004555
SL8	2.336596	0.120198	0.003394
QMU	2.175768	0.157933	0.005714
GDQ	2.318949	0.142684	0.000053
QML	2.257128	0.163585	0.000060
Teng	3.577476	0.198599	0.005787
Weighted mean and standard deviation		0.152611	± 0.003540

S Phase

Q Model	Reduced χ^2	τ_β (sec)	Standard Deviation
SL1	1.604550	0.428764	0.000202
SL2	1.455263	0.474114	0.021853
SL7	1.314070	0.463692	0.006467
SL8	1.287617	0.495703	0.007150
QMU	1.269727	0.527837	0.016826
GDQ	1.289501	0.485035	0.006701
QML	1.279111	0.544750	0.000772
QBS	1.237696	0.540175	0.002413
Weighted mean and standard deviation		0.441006	± 0.010334

The above Q models were also tested against the ScP phase t* data, with the exception of the QBS and Teng Q models. Again a least squares fit was obtained for these in the manner demonstrated in Subsection 7.2.3.3. Values for τ_α and τ_β, along with their reduced χ^2 and standard deviations for the values of the ScP phase, are given in Table 7.12. Note that the values for τ_α and τ_β are smaller than those obtained using Q_α and Q_β from free oscillations alone. If it is assumed that each Q layer in the mantle is linearly frequency dependent by the same amount, this would indicate that either the upper mantle Q values given by the free oscillation Q models are too low or the lower mantle Q values given by the models are too high. This question can only be answered by further research.

Better control of the least squares fit was obtained when only one constant at a time was estimated. This is obvious from comparison of the reduced χ^2s for the Q models given in Table 7.11 with those given in Table 6.12. For each free oscillation Q model given in Tables 7.11 and 7.12, the reduced χ^2 for ScP t* data tends to be approximately the sum of the reduced χ^2s of the S and P phases. For a given free oscillation model, a large reduced χ^2 in the ScP model to some degree represents a lack of control in the fitting function, possibly resulting in poorer estimate of the associated standard deviation for τ_α and τ_β. However, the standard deviations for τ_α and τ_β given in 7.12 can be used to find a weighted mean for these Q models. Since SL8 and GDQ give very small standard deviations for τ_α and τ_β, the weighted means are strongly influenced by these values. A second weighted mean is calculated excluding SL8 and GDQ to show that the weighted mean values for τ_α and τ_β do not differ much from the former values.

The analysis of the free oscillation Q models does not shed much light on the structure of the crust and mantle. However, it does demonstrate that the estimation of the frequency dependence of Q by the method used here does not depend greatly on which free oscillation model is used. A comparison

Table 7.12

The Least Squares Fit for τ_α and τ_β Obtained from Other Free Oscillation Q Models (cf. Table 7.9).

		ScP Phase			
Q Model	Reduced χ^2	τ_β (sec)	Standard Deviation	τ_α (sec)	Standard Deviation
SL1	4.874303	0.412138	0.013385	0.103951	0.003834
SL2	4.916819	0.414607	0.0120776	0.104397	0.003521
SL7	4.969423	0.420553	0.012225	0.106377	0.003372
SL8	4.785031	0.440000	39.2×10^{-8}	0.110000	10.3×10^{-8}
QMU	5.397561	0.449403	0.027783	0.125593	0.006950
GDQ	5.052410	0.440000	11.8×10^{-8}	0.110000	2.9×10^{-8}
QML	5.660912	0.453804	0.026051	0.126573	0.006893
Weighted means and standard deviations		0.440000	0.016583	0.110000	0.004380
Weighted means and standard deviations+		0.434972	0.016583	0.115260	0.004380

+ Note: These weighted means and standard deviations are for above models with the exception SL8 and GDQ.

between long period and short period Q's of the same phase from the same earthquake arriving at the same station is needed in order to determine the precise values for τ_α and τ_β for that particular path. Once this is done for many paths, some judgement can be made as to which of the free oscillation Q models is the best. With many such comparisons it may be possible to construct a better free oscillation Q model than can be obtained from a free oscillation data itself. This suggestion is left for future studies.

CHAPTER 8

DISCUSSION

8.1 Introduction

The study of attenuation in the earth impinges on almost every field of seismology. Factors such as the filtering properties of the measuring instrument and the source must be taken into account at the outset. A knowledge of how Q is related to the whole seismic frequency band is required before an assessment can be made about Q in the mantle. For the short period range under study in this thesis an examination of the best available analytical estimating procedures has been undertaken. Modelling of the available data over the entire distance range is required to determine the Q vs. depth relationship, as well as the effect of Q on such aspects of travel time studies as station anomalies and baseline discrepancies. The above considerations are all relevant in the present context and will be summarized further in the following sections.

8.2 Summary of the Thesis

8.2.1 Beamforming of a Seismic Array (Chapter 2)

Beamforming of seismic arrays are an important technique in reducing microseismic and random noise as much as possible. This in effect reduces the amount of noise arising from local perturbing sources which affect the incoming seismic phase, the advantage being less uncertainty in the resulting estimate of the frequency content of the seismic wavelet. More information is gained in this fashion because no artificial smoothing is required which otherwise leads to a biased estimate. Some beamformed seismic traces of the

WRA array clearly demonstrating this property were shown in Chapter 2. These beamformed arrays were therefore used as a starting point from which better estimates of the composition of a seismic wavelet can be obtained.

8.2.2 Attenuation Properties of the Mantle (Chapter 3)

In this chapter the discussion was centered around the range of plausible Q models for the mantle. There have been two approaches to this problem: (1) to develop analytical models which fit observed data and (2) to develop a model which is based upon physical parameters expected to play a role in determining the attenuation properties of the mantle. Generally the analytical models given by Futterman (1962), Lamb (1962), Strick (1967) and Kalinin, (1967) are easier to use because fewer parameters are needed to describe these models. Physical Q models given by Walsh (1968, 1969), Liu et al., (1976), Gordon and Nelson (1966) and more recently by Minster (1978a, 1978b) suffer from having too many parameters to be estimated with a limited amount of data throughout the seismic frequency range. Until more data (t* vs. frequency) are available throughout the seismic band these models cannot be confirmed or eliminated as possibilities.

Certain attenuation models can be eliminated by physical considerations. The one principle which must be maintained is that a seismic wave passing through the earth must be causal. This means that Q in the layered earth must to some extent be frequency dependent. If Q is frequency dependent then the phase velocity of a wave passing through a given layer must also be frequency dependent excluding the one exception when $Q = Q_0\omega$. The extent of the Q and phase velocity frequency dependence has been an open question up to this point in time. This point will be discussed in more detail in Section 8.2.6.

8.2.3 Seismic Wavelet Description (Chapter 4)

It is impossible at this stage to specify all the impulse responses needed for an unambiguous determination of Q. The only impulse function known for certain is the instrument response. The response due to the earthquake source function is less well known. However, the bulk of the presently available evidence indicates a source function similar to that described by Brune (1970, 1971). If the earthquake source response is as described by Savage (1966), for which the source energy drops off with the third power, and further assuming that the corner frequency is close to the mid-frequency range of measurement, then there will be only a change in t* of approximately 0.05 seconds. This small change in t* would result in a slightly higher value for Q estimated in the short period seismic range. As pointed out in Chapter 4, however, Savage's model has been rejected by Randall (1973) on theoretical grounds. The impulse responses of the source and receiver structure are impossible to ascertain with the present knowledge of the crustal structure at WRA and the structure at the source. If these impulse sources are considered to be in part random, beamforming of the array helps to reduce their effect. Scattering at the source will probably differ for each earthquake and therefore its phase and amplitude components of scattered responses cannot be estimated. Horizontal instruments recently installed at the array site were not available for this study, but can be used in the future to study the receiver crustal structure. Determination of the phase and amplitude changes caused by the transmission of seismic energy through the earth requires the use of full wave theory. These changes in phase and amplitude due to transmission coefficients are not expected to alter the power spectrum of the incoming energy but may alter the overall appearance of the impulse response in the time domain.

8.2.4 Unsuccessful Analytical Procedures Used to Determine t* Values (Chapter 5)

As pointed out in this chapter, the advantage of frequency domain methods over time domain methods is that the phase velocity properties do not have to be known. This eliminates one of the unknowns from the determination of the attenuation properties of the mantle. However, the problem does not therefore become simple, since the best spectral method to be used must be determined. It has been determined in this chapter that the autoregressive process as described by Yule-Walker and Burg cannot be applied to transient seismic wavelets because these wavelets are better modelled as a moving average process. Fourier analyses leads to side lobe effects caused by the windowing function (sinc function) of the time series being processed. In many examples in the literature one has only to measure the frequency range between successive dips in the measured power spectra in order to determine the length of the time series used by the author. Examples of such spectra can be found in Yoshida and Tsujiura (1975). Conventional windowing and smoothing of power spectra of real time series should therefore be treated with great caution because these techniques tend to bias the true spectrum (Yuen, 1979).

8.2.5 Successful Analytical Procedures used to Determine t* Values (Chapter 6)

The two remaining spectral techniques investigated in this thesis are the Maximum Likelihood (Lacoss, 1971, 1977) and Homomorphic Deconvolution (Oppenheim et al., 1968) methods. One advantage of the Maximum Likelihood method is that subjective guessing as to windowing and smoothing functions are not necessary when this technique is applied to a real time series. A power spectrum is returned with very little distortion. The only

disadvantage of this method is its limitation of the dynamic range from the peak power estimate. This effect may be compensated for by pre-whitening the time series before application of the spectral technique. The best pre-whitening function is still under investigation. On the other hand, the Homomorphic Deconvolution method suffers from the investigator picking a cutoff point in the complex cepstrum. In the seismic wavelet case, the point is picked just before the spike in the complex cepstrum caused by the truncated window. Since most of the time series is contracted to approximately one-third of the original length in the complex cepstrum (Ulrych, 1971), very little of the deterministic signal is lost. Owing to the randomness of phase of the noise, the complex noise cepstrum is distributed throughout. As shown in Chapter 6, filtering of the complex cepstrum demonstrates the effectiveness of noise and windowing function elimination. This is the reason why Homomorphic Deconvolution has been preferred in determining t* values in this study.

8.2.6 Evaluation of t* by Least-Squares Procedures (Chapter 7)

After the best estimate of the spectral power is made by the Homomorphic Deconvolution technique, an estimate for each weighted t* value is determined assuming that the relative variances of the power spectra are proportional to the number of seismic channels beamformed. In this way a relative standard deviation of the mean for the t* values can be estimated. Upon collection of t* values for the P, S, ScP and PcP phases, these values are plotted against the mid-frequency range at which the estimate was taken. The plots of t* vs. frequency clearly demonstrate a correlation between these two variables, whereas plotting t* or its resulting Q value against source depth or azimuth only result in a scatter diagram in which no apparent correlation can be seen. Comparison of these short period t* values with the

t* values calculated from Anderson's SL7 Q Model require that Q be frequency dependent if the t* values given in the two frequency ranges (Free Oscillation and short period phases) are to be self consistent. The first order frequency dependent Q model (Q Model 2) presented here will undoubtedly require refinement when t* values at intermediate and high frequency ranges as they are determined.

Chapter 7 discusses some of the implications of Q Model 2 for Q_α/Q_β, Q_K and phase velocity dispersion. Furthermore the model predicts what the apparent Q's would be for ScS body wave phases throughout the seismic frequency spectrum. As new data become available, the above implications or prediction can be tested. Adjustment of τ_α and τ_β would not be unexpected. Improved free oscillation and surface wave models will also have an impact upon the values of τ_α and τ_β. Finally, other free oscillation Q models were examined to determine which results in the best fit to the short period t* values.

8.3 Suggestions for Further Investigation

8.3.1 Improvements of Spectral Estimators

The results of this research indicate that spectral estimators have been properly chosen. Since Q in the mantle has been determined to be frequency dependent, its associated phase velocity must be dispersive. Therefore, when a power estimate is made for a dispersive truncated real seismic wavelet, the spectral phase angle will be different for each spectral frequency estimate. This dispersion effect is enough to result in the side lobe effects which are observed in Fourier power spectra. To compensate for this side lobe effect the seismic time series must be windowed in such a way

as to remove spectral phase transitions. Compensating for such spectral phase transitions at the truncation point by linear windowing of Fourier power spectra will become difficult if not impossible. The methods of Maximum likelihood (Lacoss, 1971) and Homomorphic Deconvolution (Oppenhiem et al., 1968) appear to eliminate satisfactorily the spectral phase effect due to seismic dispersion. In addition to this windowing, the complex cepstrum in the case of Homomorphic Deconvolution can help to eliminate effects of other seismic phases which arrive within the seismic wavelet under study. This is especially so in the case of S phases where seismic wave mixing is common.

The above two spectral techniques can be made to operate more efficiently by increasing the sampling rate when digitizing the seismic phase. Lacoss (1971, 1977) has shown that the spectral bandwidth frequency estimate decreases with the number of digitized samples per unit time of a time series. In the case of Homomorphic Deconvolution, the increase in digital sampling of a time series better defines the properties of the complex cepstrum (Ulrych, 1971). With a better defined complex cepstrum a finer cutoff point can be determined, resulting in less perturbed power estimates.

8.3.2 Possible Areas of Further Investigations

Assuming that Q Model 2 is close to the correct Q model for the mantle, it necessitates the construction of apparent Q_o and infinite frequency velocity models for both shear and compressional waves. Using free oscillation Q data, a Q_o model can be developed. The values of τ_α and τ_β form the Q Model 2 and its phase velocity counterpart can be used as starting values to perturb such free oscillation models. Further velocity

models for the mantle can be constructed by pre-filtering travel time record sections for a given high frequency cutoff so that travel time residuals caused by the attenuation causality will not affect such velocity models. After such a velocity model for the mantle at a given frequency cutoff is made, an infinite frequency velocity model for the mantle can be constructed by extrapolation. Both long period and short period velocity modelling should make such extrapolation possible. In the past the relationship between Q and velocity has not been considered very important. Investigators interested in Q have not recorded travel times, and conversely velocity studies have not paid much attention to the Q aspect of the problem. The consideration of both travel times and Q will lead to greater constraints on possible mantle materials.

Source studies now can be better treated assuming that Q Model 2 and its associated phase velocities are correct. When the phase response due to Q, and other known phase responses, are removed from the source spectrum, better source models can possibly be developed. This research awaits future studies. Studies related to creep, viscosity, temperature and pressure conditions in the mantle, to name only a few, may be investigated more completely with the relationship between Q and frequency in mind. Many doors may therefore be opened for future investigations.

REFERENCES

Akaike, H. (1969a) Fitting autoregressive models for prediction. *Ann. Inst. Stutisit. Math., 21,* 243-247.

Akaike, H. (1969b) Power spectrum estimation through autoregressive model fitting. *Ann. Inst. Stutist. Math., 21,* 407-419.

Aki, K. (1967) Scaling law of seismic spectrum. *J. Geophys. Res., 72,* 1217-1231.

Anderson, D.L. (1967) The anelasticity of the mantle. *Geophys. J. 14,* 135.

Anderson, D.L. and Archambeau, C.B. (1964) The anelasticity of the earth. *J. Geophys. Res., 69,* 2071-2084.

Anderson, D.L., Ben-Menahem, A. and Archambeau, C.B. (1965) Attenuation of seismic energy in the upper mantle. *J. Geophys. Res., 70,* 1441-1448.

Anderson, D.L. and Hart, R.S. (1976) An earth model based on free oscillations and body waves. *J. Geophys. Res., 81,* 1461-1475.

Anderson, D.L. and Hart, R.S. (1978a) Attenuation models of the earth. *Physics of the Earth and Planetary Interiors, 16,* 289-306.

Anderson, D.L. and Hart, R.S. (1978b) Q of the earth. *J. Geophys. Res., 83,* 5859-5882.

Archambeau, C.B., Flinn, E.A. and Lambert, D.G. (1969) Fine structure of the upper mantle. *J. Geophys. Res., 74,* 5825-5865.

Attwell, P.B. and Ramana, Y.V. (1966) Wave attenuation and internal friction as functions of frequency in rocks. *Geophysics, 31,* 1049-1056.

Azimi, SH.A., Kalinin, A.V., Kalinin, V.V. and Pivovarov, B.L. (1968) Impulse and transient characteristics of media with linear and quadratic absorption laws. *Izv. Earth Physics, No.2,* 88-93, (Russian to English translation).

Barazangi, M. and Isacks, B. (1971) Lateral variations of seismic-wave attenuation in the upper mantle above the inclined earth. *J. Geophys. Res., 76,* 8493-8516.

Barley, B.J. (1977) Short period teleseismic S waves. *Ph.D. Thesis,* Dept. of Earth Science, Leeds University, England.

Bäth, M. (1974) Spectral analysis in geophysics. *Elsevier Scientific Publishing Company, N.Y.*

Bäth, M. and Arroyo, A. Lopez (1962) Attenuation and dispersion of G waves. *J. Geophys. Res., 67,* 1933-1942.

Bendat, J.S. and Piersol, A.F. (1971) Random data: Analysis and Measurement Procedures. *Wiley-Interscience, New York.*

Best, W.J., Johnson, L.R. and McEvilly, T.V. (1974) ScS and the mantle beneath Hawaii. *EOS (Trans. Am. Geophys. Union), 56,* 403 (abs.).

Bevington, P.R. (1969) Data reduction and error analysis for the physical sciences. *McGraw-Hill Book Company, New York.*

Brace, W.F., Luth, W.C. and Unger, J. (1967) Melting of granite under an effective confining pressure. (Abs.) *Paper presented at the Annual Meeting of the Geological Society of America.*

Brune, J.N. (1970) Tectonic stress and spectra of seismic shear waves from earthquakes. *J. Geophys. Res., 75,* 4997-5009.

Brune, J.N. (1971) Correction (to Brune 1970). *J. Geophys. Res., 76,* 5002.

Buchbinder, G.G.R. and Poupinet, G. (1973) Problem related to PcP and the core-mantle boundary illustrated by two nuclear events. *B.S.S.A., 63,* 2047-2070.

Burg, J.P. (1967) Maximum entropy spectral analysis. *Paper presented at 37th Annual International SEG Meeting, Oklanhoma City, Oklahoma, October 31, 1967.*

Capon, J., Greenfield, R.J. and Kolker, R.J. (1967) Multidimensional maximum-likelihood processing of a large aperture seismic array. *Proceedings of the I.E.E.E., 55,* 192-211.

Capon, J. (1973) Signal processing and frequency-wavenumber spectrum analysis for a large aperture seismic array. *Method in Computational Physics, 13,* Editor B.A. Bolt, Academic Press, N.Y., 1-59.

Chatfield, C. (1975) The analysis of time series: Theory and practice. *Chapman and Hall, London.*

Choudbury, M.A. and Dorel, J. (1973) Spectral ratio of short period ScP and ScS phases in relation to the attenuation in the mantle beneath the Tasman Sea and Antarctic region. *Geophys. Res., 81,* 3066.

Dash, B.P. and Obaidullah, K.A. (1970) Determination of signal and noise statistics using correlation theory. *Geophysics, 35,* 24-32.

Der, Z.A. and McElfresh, T.W. (1977) The relationship between anelastic attenuation and regional amplitude anomalies of short-period P waves in North America. *B.S.S.A., 67,* 1303-1317.

Douglas, B.M. and Ryall, A. (1972) Spectral characteristics and stress-drop for micro-earthquakes near Fairview Peak, Nevada. *J. Geophys. Res., 77,* 351-359.

Dziewonski, A.M. and Gilbert, F. (1972) Observation and normal modes from 84 recordings of the Alaskan earthquake of 1964, March 28. *Geophys. J. Astron. Soc., 27,* 393-411.

Dziewonski, A.M., Hales, A.L. and Lapwood, E.R. (1975) Parametrically simple earth models consistent with geophysical data. *Physics of the Earth and Planetary Interiors, 10,* 12-48.

Ewing, M. and Press, F. (1954) Mantle Rayleigh waves from the Kamchatka earthquake of November 4, 1952, *B.S.S.A., 50,* 471-479.

Frasier, C.W. and North, R.G. (1978) Evidence for ω-cube scaling from amplitudes and periods of the Rat Island Sequence (1965). *B.S.S.A., 68,* 265-282.

Furuya, I. (1969) Predominant period and magnitude. *Journal of Physics of the Earth, 17,* 119-126,

Futterman, W.I. (1962) Dispersive body waves. *J. Geophys. Res. 67,* 5279-5291.

Gilbert, F. and Dziewonski, A.M. (1975) An application of normal mode theory and retrieval of structural parameters and source mechanisms from seismic spectra. *Phil. Trans. Roy. Soc. London, Ser. A, 278,* 187.

Gladwin, M.T. and Stacey, F.D. (1974) Anelastic degradation of acoustic pulses in rock. *Physics of the Earth and Planetary Interiors, 8,* 332-336.

Gordon, B.G. and Nelson, C.N. (1966) Anelastic properties of the earth. *Rev. of Geophys., 4,* 457-474.

Gross, B. (1947) On creep and relaxation. *Journal of Applied Physics, 18,* 212.

Haddon, R.A.W. and Cleary, J.R. (1974) Evidence for scattering of seismic PKP waves near the mantle-core boundary. *Physics of the Earth and Planetary Interiors, 8,* 211-234.

Hales, A.L. (1976) ScS travel time residuals and the difference between continents and oceans. *Earth Planet. Sci. Lett., 33,* 249-254.

Hanks, T.C. and Wyss, M. (1972) The use of body-wave spectra in the determination of seismic-source parameters. *B.S.S.A., 62,* 561-589.

Hart, R.S., Anderson, D.L. and Kanamori, H. (1977) The effect of attenuation of gross earth models. *J. Geophys. Res., 82,* 1647-1654.

Haskell, N.A. (1964) Total energy and energy density of elastic wave radiation from propagating faults. *B.S.S.A., 54,* 1811-1841.

Haskell, K. (1966) Total energy and energy spectral density of elastic wave radiation from propagating faults, Part II. *B.S.S.A., 56,* 125-140.

Ibrahim, A.K. (1971a) Effects of a rigid core on the reflection and transmission coefficients from multi-layered core-mantle boundary. *Pure and Appl. Geophys. 8,* 114-133.

Ibrahim, A.K. (1971b) The amplitude ratio PcP/P and the core-mantle boundary. *Pure and Appl. Geophys., 8,* 114-133.

Jackson, D.D. and Anderson, D.L. (1970) Physical mechanisms of seismic-wave attenuation. *Rev. Geophys. and Space Phys., 8,* 1-63.

Jackson, D.D. (1969) Elastic relaxation model for seismic wave attenuation in the earth. *Phys. Earth Planet. Interiors, 2,* 30-34.

Jeffreys, H.A. (1965) The damping of S waves, *Nature, 208,* 675.

Jenkins, G.M. and Watts, D.G. (1968) Spectral analysis and its applications. *Holden-Day, San Francisco.*

Jordan, T.H. and Anderson, D.L. (1974) Earth structure from free oscillation and travel-times. *Geophys. J. Roy. Astron. Soc., 36,* 411-459.

Jordan, T.H. (1975) Lateral heterogeneity and mantle dynamics. *Nature, 257,* 745-750.

Jordan, T.H. and Sipkin, S.A. (1977) Estimation of the attenuation operator for multiple ScS waves. *Geophysical Research Letters, 4,* 167-170.

Kalinin, A.V., Azimi, SH.A. and Kalinin, V.V. (1967) Estimate of the phase-velocity dispersion in absorbing media. *Izv. Earth Physics, No.4,* 249-251 (Russian to English translation).

Kanamori, K. (1967a) Spectrum of P and PcP in relation to the mantle-core boundary and attenuation in the mantle. *J. Geophys. REs., 72,* 2181-2186.

Kanamori, K. (1967b) Spectrum of short-period core phases in relation to the attenuation in the mantle. *J. Geophys. Res., 72,* 2181-2186.

Kanasewich, E.R. (1973) Time sequence analysis in geophysics. *The University of Alberta Press, Canada.*

Kasahara, K. (1957) The nature of seismic origins as inferred from seismological and geodetic observation (1). *Bull. Earthquake Res. Inst., 36,* 473-532.

Kasahara, K. (1960) An attempt to detect azimuth effect on spectral structures of seismic waves. (The Alaskan earthquake of April 7, 1958). *Bull. Earthquake Res. Inst., 38,* 207-218.

Keen, C.G., Montgomery, J., Mowat, W.M., Mullard, J.E. and Platt, D.C. (1965) British seismometer array recording systems. *The Radio and Electronic Engineer, 30,* 297-306.

Key, F.A. (1967) Signal generated noise at the Eskdalemuir seismometer array station. *B.S.S.A., 57,* 27-37.

King, D.W. (1974) Automation of the reduction of seismic data. *Ph.D. Thesis, Department of Engineering Physics, Research School of Physical Sciences, The Australian National University, Canberra, A.C.T., Australia.*

Knopoff, L. (1964) Q. *Reviews of Geophysics, 2,* 625-660.

Kogan, S.Y. (1966a) A brief review of seismic wave absorption theories I. *Izv., Earth Physics, No.11,* 689-695. (Russian to English translation).

Kogan, S.Y. (1966b) A brief review of seismic wave absorption theories II. *Izv., Earth Physics, No.11,* 696-701. (Russian to English translation).

Koopmans, L.H. (1974) The spectral analysis of time series. *Academic Press, New York.*

Kovach, R.L. and Anderson, D.L. (1964) Attenuation of shear waves in the upper and lower mantle. *B.S.S.A., 54,* 1855-1864.

Kulhánek, O. (1968) Seismic noise discrete filtering. *Pure and Applied Geophysics, 69,* 5-11.

Lacoss, R.T. (1971) Data adaptive spectral analysis methods. *Geophysics, 36,* 661-675.

Lacoss, R.T. (1977) Autoregressive and maximum likelihood spectrum analysis methods. *Aspects of Signal Processing, Part 2,* by D. Reidel Publishing Company, Dordrecht-Holland, 591-615.

Lamb, G.L. Jr. (1962) The attenuation of waves in a dispersive medium. *Journal of Geophysical Research, .87,* 5273-5277.

Levinson, H. (1947) The Wiener RMS (root mean square) error criterion in filter design and prediction. *J. Math. Phys., 25,* 261-278.

Lines, L.R. and Ulrych, T.J. (1977) The old and new in seismic deconvolution and wavelet estimation. *Geophysical Prospecting, 25,* 512-540.

Liu, H.P., Anderson, D.L. and Kanamori, H. (1976) Velocity dispersion due to anelasticity: Implications for seismology and mantle composition. *Geophys. J. Roy. Astron. Soc., 47,* 41.

Lomnitz, C. (1956) Creep measurements in igneous rocks. *J. Geol., 64,* 473-479.

Lomnitz, C. (1957a) Linear dissipation in solids. *Journal of Applied Physics, 28,* 201-205.

Lomnitz, C. (1957b) Application of the logarithmic creep law to stress wave attenuation of the solid earth. *J. Geophys. Res., 67,* 365-368.

Mack, H. (1969) Nature of short-period signal variations at LASA. *Journal of Geophysical Research, 74,* 3161-3170.

Madariaga, R. (1977) High-frequency radiation from crack (stress-drop) models of earthquake faulting. *Geophys. J.R. astr. Soc., 51,* 625-651.

Minster, J.B. (1978a) Transient and impulse responses of a one-dimensional linearly attenuation medium-I. Analytical results. *Geophys. J.R. astr. Soc., 52,* 479-501.

Minster, J.B. (1978b) Transient and impulse responses of a one-dimensional linearly attenuating medium-II. A parametric study. *Geophys. J.R. astr. Soc., 52,* 503-524.

Mitchell, B.J. and Helmberger, D.V. (1973) Shear velocities at the base of the mantle from observation of S and ScS. *J. Geophys. Res., 78,* 6009.

Mitronovas, W., Isacks, B. and Seeber, L. (1969) Earthquake locations and seismic wave propagation in the upper 250 km of the Tonga Island Arc. *B.S.S.A., 59,* 1115-1135.

Molnar, P. and Atwater, T. (1978) Interarc spreading and cordilleran tectonics as alternates related to the age of subducted oceanic lithosphere. *Earth and Planetary Science Letters, 41,* 330-340.

Muirhead, K.J. (1968) The reduction and analysis of seismic data using digital computers. *Ph.D. Thesis, Department of Engineering Physics, Research School of Physical Sciences, The Australian National University, Canberra, A.C.T., Australia.*

Nukanishi, I. (1979) Attenuation of multiple ScS waves beneath the Japanese arc. *Physics of the Earth and Planetary Interiors, 19,* 337-347.

Oliver, J. and Isacks, B. (1967) Deep earthquake zones, anomalous structures in the upper mantle, and the lithosphere. *J. Geophys. Res., 72,* 4259.

Oppenheim, A.V. and Schafer, R.W. (1975) Digital signal processing. *Prentice-Hall, Inc., Englewood Cliffs, New Jersey.*

Oppenheim, A.V., Schafer, R.W. and Stockham, Jr., T.G. (1968) Nonlinear filtering of multiplied and convolved signals. *Proceedings of the ... I.E.E.E., 56,* 1264-1291.

Otsuka, M. (1962) On the forms of the S and ScS waves of some deep earthquakes. *Zisin, 2(15),* 169 (In Japanese), (taken from Table 1, Anderson and Hart, 1978).

Otsuka, M. (1963) Some considerations on the waveforms of ScS phases. *Spec. Contrib. Geophys. Inst., Kyoto Univ. 2,* 415, (taken from Table 1, Anderson and Hart, 1978).

Papoulis, A. (1962) The Fourier Integral and its applications. *McGraw-Hill Book Company Inc., New York.*

Press, F. (1956) Rigidity of the earth's core. *Science, 124,* 1204.

Ram Datt (1977) A P-wave velocity structure for the upper mantle and transition zone, using the Warramunga array. *Ph.D. Thesis, Research School of Earth Sciences, The Australian National University, Canberra, A.C.T., Australia.*

Randall, M.J. (1973) The spectral theory of seismic sources. *B.S.S.A., 63,* 1133-1144.

Randall, M.J. (1976) Attenuative dispersion and frequency shifts of the earth free oscillations. *Phys. Earth Planet. Interiors, 12,* P1-P4.

Richter, C.F. (1958) Elementary seismology. *W.H. Freeman and Company, San Francisco and London.*

Robinson, J.C. (1970) Statistically optimal stacking of seismic data. *Geophysics, 35,* 436-446.

Sailor, R.V. and Dziewonski, A.M. (1978) Measurement and interpretation of normal mode attenuation. *Geophys. J.R. astr. Soc., 53,* 559-581.

Satô, R. and Espinosa, A.F. (1967) Dissipation in the earth's mantle and rigidity and viscosity in the earth's core determined from waves multiply-reflected from the mantle core boundary. *B.S.S.A., 57,* 829.

Satô, Y. (1957) Attenuation, disperison and the wave guide of the G wave. *B.S.S.A., 48,* 231-251.

Savage, J.C. (1966) Radiation from a realistic model of faulting. *B.S.S.A., 56,* 577-592.

Savarensky, E.F., Popov, I.I., and Lazareva, A.P. (1961) Observations of long periods waves of the Chilean earthquake of 1960. *AKad. Nauk. SSSR Ser. Geofiz.* 744-748.

Simpson, D.W. (1973) P. wave velocity structure of the upper mantle in the Australian region. *Ph.D. Thesis, Department of Geophysics and Geochemistry, The Australian National University, Canberra, A.C.T., Australia.*

Sipkin, S.A. and Jordan, T.H. (1979) Frequency dependence of Q_{ScS}. *B.S.S.A., 69,* 1055-1979.

Solomon, S.C. and Toksöz, M.N. (1970) Lateral variation of attenuation of P and S waves beneath the United States. *B.S.S.A., 60,* 812-838.

Stacey, F.D., Gladwin, M.T., McKavanagh, B., Linde, A.T. and Hastie, L.M. (1975) Anelastic damping of acoustic and seismic pulses. *Geophysical Surveys, 2,* 133-151.

Strick, E. (1967) The determination of Q, dynamic viscosity, and transient creep curves from wave propagation measurements. *Geophys. J. Roy. Astron. Soc., 13,* 197.

Sutton, G.H., McCreery, C.S., Duennebier, F.K. and Walker, D.A. (1978) Spectral analyses of high-frequency P_n, S_n phases record on ocean bottom seismographs. *Geophysical Research Letters, 5,* 745-747.

Takano, K. (1971) A note on the attenuation of short period P and S waves in the mantle. *J. Phys. Earth, 19,* 155-163.

Teng, T. (1967) Attenuation of body waves and the Q structure of the mantle. *J. Geophys. Res., 73,* 2195-2208.

Terashima, T. (1968) Magnitude of microearthquake waves. *Bull. Int. Inst. Seismol. Earthquake Eng. 5,* 31-108.

Tribolet, J.M. (1977) A new phase unwrapping algorithm. *I.E.E.E. Transactions on Acoustics, Speech and Signal Processing, ASSP-25,* 170-177.

Tucker, B.E. and Brune, J.N. (1973) Seismograms, S-wave spectra and source parameters for after shocks of the San Fernando earthquake of February 9, 1971. *N.O.A.A. (Special Report).*

Ulrych, T.J. (1971) Application of homomorphic deconvolution to seismology. *Geophysics, 36,* 650-660.

Ulrych, T.J. and Bishop, T.N. (1975) Maximum entropy analysis and auto-regressive decompostion. *Reviews of Geophysics and Space Physics, 13,* 183-200.

Ulrych, T.J., Jensen, R.M., Ellis, R.M. and Somerville, P.G. (1972) Homomorphic deconvolution of some teleseismic events. *B.S.S.A., 62,* 1269-1281.

Underwood, R. (1967) The seismic network and its applications. *Ph.D. Thesis, Department of Geophysics and Geochemistry, The Australian National University, Canberra, A.C.T., Australia.*

Walker, D.A. (1977a) High-frequency P_n phases observed in the Pacific at great distances. *Science, 197,* 257-259.

Walker, D.A. (1977b) High-frequency P_n and S_n phases recorded in the western Pacific. *J. Geophys. Res., 82,* 3350-3360.

Walker, D.A., McCreery, C.S., Sutton, G.H. and Duennebier, F.K. (1978) Sprectral analyses of high-frequency P_n and S_n phases observed at great distances in the western Pacific. *Science, 199,* 1333-1335.

Walker, G. (1931) On periodicity in series of related terms. *Proc. Roy. Soc. London Ser. A, 131,* 518-532.

Walsh, J.B. (1968) Attenuation in partially melted material. *Journal of Geophysical Research, 73,* 2209-2216.

Walsh, J.B. (1969) New Analysis of attenuation in partially melted rock. *Journal of Geophysical Research, 74,* 4333-4337.

Welch, P.D. (1967) The use of fast Fourier transform for the estimation of power spectra: A method based on time averaging over, modified periodograms. *I.E.E.E. Transactions on Audio and Electroacoustics, AU-15,* 70-73.

Wiener, N. (1949) Extrapolation, interpolation and smoothing of stationary time-series. *Cambridge, Mass. M.I.T. Press.*

Wright, C. (1970) P wave investigations of the earth's structure using the Warramunga seismic array. *Ph.D. Thesis, Department of Geophysics and Geochemistry, The Australian National University, Canberra, A.C.T., Australia.*

Wyss, M. and Hanks, T.C. (1972) The source parameters of the San Fernando Earthquake inferred from teleseismic body waves. *B.S.S.A., 62,* 591-602.

Yoshida, M. and Tsujiura, M. (1975) Spectrum and attenuation of multiply reflected core phases. *J. Phys. Earth, 23,* 31-42.

Yuen, C.K. (1979) Comments on modern methods for spectrum estimation. *I.E.E.E. Transactions on Acoustics, Speech and Signal Processing, ASSP-27,* 298-299.

Yule, G.U. (1927) On a method investigating periodicities in disturbed series with special reference to Wolfer's sunspot numbers. *Phil. Trans. Roy. Soc., London Ser. A, 226,* 267-298.

Zener, C. (1948) Elasticity and anelasticity of metals. *The University of Chicago, Illinois.*